POLITECNICO DI MILANO

MASTER DEGREE IN BIOMEDICAL ENGINEERING -
BIOMECHANICS AND BIOMATERIALS

SCHOOL OF INDUSTRIAL AND INFORMATION ENGINEERING
DEPARTMENT OF ELECTRONICS INFORMATION AND BIOENGINEERING

Development of a numerical model for the analysis of the thrombogenic potential associated with residual contractility and inflow cannula positioning in the VAD-assisted left ventricle

Advisor:
Prof. Alberto Redaelli
Co-advisor:
Prof. Filippo Consolo

Graduation Thesis of:
Antonio Crescenzo, 862618
Ilaria Urciuoli, 862547

ACADEMIC YEAR 2017–2018

Contents

Summary

Introduction

Heart failure (HF) is a severe pathological chronic condition where the heart is unable to pump enough blood to support the needs of other organs in the body. Approximately half of the patients with HF is affected by dilated cardiomyopathy (DCM), a syndrome characterized by enlargement, wall hypokinesis, and reduction of the overall contractility (typically < 40%) of left or both ventricles [1-4], which acquire a pathological-dilated nearly spherical shape [5].

Patients with advanced and/or end-stage HF have limited treatment options. Indeed, only a small number of patients may qualify for cardiac transplantation, which is restricted by stringent selection criteria and lack of availability of donor hearts. Consequently, mechanical circulatory support system, in particular, left ventricular assist devices (LVADs) implantation has been introduced as bridge to transplantation or as destination therapy.

The current generation of LVADs has five main components: the inflow cannula, the pump body (centrifugal or axial), the outflow cannula, the percutaneous drive-line, and the external controller (Figure 1).
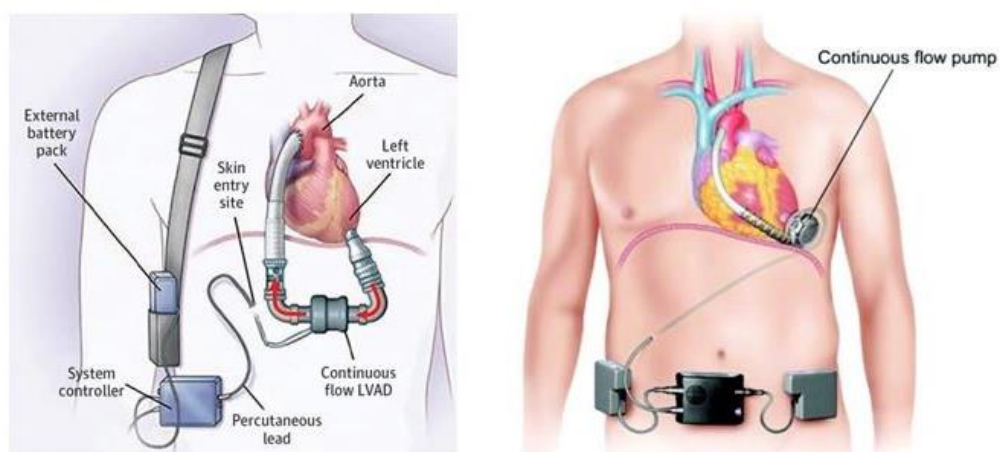
Figure 1: LVAD components. Left: pump placed within the peritoneal cavity. Right: pump placed "on board" of the heart.

Despite the widespread clinical use of LVADs, there are a number of complications associated with the therapy, the most relevant being those associated with the device-related thrombogenicity.

Thrombus formation was demonstrated [6-9] to often develop at the interface between the ventricular endocardial surface and the LVAD inflow cannula, with subsequent thrombotic apposition on the cannula and, eventually, migration and ingestion of intraventricular thrombi into the pump. Ingested thrombi may either enhance pump thrombosis or, when propelled downstream, provoke thromboembolic events.

Several mechanisms have been suggested to trigger and promote intraventricular thrombus formation:

- activation of the coagulation cascade due to blood contact with the artificial surface of the LVAD, at the LV apex-LVAD inflow cannula interface;
- prothrombotic platelet function: activated/sensitized platelets – due to recirculation within the "hypershear" environment of the pump – are prone to thrombus formation within the implanted LV when facing the LVAD inflow cannula;
- the altered ventricular hemodynamics (stagnation regions and recirculation zones) due to:

  i. enlargement of the LV chamber and reduced contractility;

  ii. LVAD implantation, in particular the LVAD inflow cannula/outflow graft surgical implantation configuration.

In particular, aberrant flow patterns are observed in patients with DCM: while the normal LV flow pattern has been reported to recycle the blood volume inside the LV every 2–3 beats, blood transport is significantly altered in patients with reduced contractility by large swirling flow patterns, where blood is trapped and undergoes altered flow patterns throughout most of the cardiac cycle [10]. In details, stagnant flow is present in the lower apical region, where it triggers the thrombotic process.

In this study, we hypothesize that the residual contractility of a dilated ventricle can act as an additional thrombogenic factor, since the degree of cardiac impairment associated with HF seems to have a role in altering LV hemodynamics. Altered intraventricular hemodynamics might promote prothrombotic conditions, especially in the LV apical region, where the LVAD inflow cannula is inserted.

Therefore, given that both the LV residual contractility and the LVAD implantation configuration have a role in altering the LV hemodynamic, we herein analysed the mutual interactions between these two factors.

Hence, the present work is focused on the development of a computational fluid dynamic (CFD) model aimed to analyse the hemodynamics of a LVAD-supported patient-specific LV. In detail, we compared LV hemodynamics in the LVAD-implanted LV by varying selectively: *i)* the LV residual contractility (as a means of modelling different degrees of HF) and *ii)* the LVAD inflow cannula positioning. Blood flow characteristics, such as shear stress, stagnation zones and recirculation patterns were assessed, *pre-* as well as *post-* implantation of the LVAD

State of the Art

Several studies in literature [11-16] investigated the disturbed hemodynamics and the thrombogenic potential of the LV in presence of LVAD through CFD approach, which provides detailed characterization of the ventricular flow, such as velocity profiles, shear stress distributions, and re-circulation patterns. The most crucial element that can alter the physiological hemodynamics of the LV is the inflow cannula, whose geometry, insertion depth, insertion angle and position may modify the intraventricular flow fields.

However, two weak points, affecting most of the examined literature, were identified. First of all, when modelling ventricular wall motion, only myofibers contraction was included, without considering the torsional contribution, thus preventing to achieve realistic simulations of cardiac dynamics [17-19]. Secondly, when characterizing LV-LVAD hemodynamics, the LV was generally considered as a rigid and static body, neglecting any

residual contractility [11, 14-15]. After LVAD implantation, LV size decreases due to cardiac remodelling, and native ventricular contractility can be partially recovered. The addition of a wall moving boundary in CFD simulations would change regions of possible stagnation and rate of LV washout.

So, in order to overcome some of the limitations of current literature studies, in this study the dynamics of the heart was modelled including both LV contraction and torsion, through the prescribed moving boundaries approach, that is by assembling a set of mathematical equations to formulate and model LV wall motion, both for the *pre* and the *post* implants scenarios.

Materials and Methods

In this study, three sets of simulations were conceived:

- Set 1 (*Pre-implant*): This set consists of three simulations, the fluid dynamic domain being a pathologically dilated patient-specific LV.
  Transient CFD simulations of the whole cardiac cycle were carried out, considering a set of three residual ejection fraction (15% - 10% - 5% EF), parameter which resembles the LV residual contractility. These values of EF% correspond to increasing levels of cardiac impairment, that is from moderate to severe HF.
  By means of this numerical approach, the role of LV residual contractility as a possible thrombogenic factor was explored.

- Set 2 (*Post-implant A*): The CFD model is based on the same pathologically dilated patient-specific LV of Set 1, post the LVAD implantation. Patient-specific inflow cannula positioning was derived from imaging techniques and reconstruction process. This set consists of a matrix of 8 test conditions, obtained combining 4 values of residual EF% (0 - 5 - 10 - 15%) with suitable levels of support (LVAD flow rates), having as a target a total cardiac output of 5 L/min. Accordingly, the interplay between LV residual contractility and LVAD flow rate was evaluated.

- Set 3 (*Post-implant B*): This set consists of 2 test conditions, selected from Set 2 simulation matrix. These 2 configurations were chosen considering the total cardiac output (CO) provided to the patient, that is the sum of native residual CO and LVAD flow rate. Total CO was assigned equal to 5 L/min, a condition mimicking the average cardiac output at rest, so as to refer to real clinical data.

  In this set of simulations, cannula position was varied with respect to Set 2: it was modelled so that the inflow cannula longitudinal axis intersects the LV apex and the centre of the mitral valve orifice.

  The aim was to quantify the impact of cannula position on LV thrombogenicity, so to identify the most hemodynamically favourable LVAD implantation configuration.

3D trans-thoracic echocardiography (3DTTE) was performed on a candidate to LVAD implantation. 3DTTE data were used to extract the pathological patient-specific LV in the end-diastolic configuration, through an in-house reconstruction tool, developed within the Biomechanics group of Politecnico di Milano. The study was performed in collaboration with the team of the Advanced Heart Failure and Mechanical Circulatory Program of the San Raffaele Scientific Institute and the Università Vita Salute San Raffaele in Milano.

The 3D CAD Software SpaceClaim (ANSYS 18.1) was exploited to obtain the 3D LV fluid domain in the *pre-implant* configuration. To guarantee a fully developed flow during the simulations, a synthetic/paradigmatic portion of the atrium chamber and of the proximal aorta were created.

To obtain the fluid domain of *post-implant* models A and B, a LVAD inflow cannula was added to the LV, in the patient-specific reconstructed position (Set 2) and in the apical configuration (Set 3).

The LV wall motion was defined through a set of mathematical equations, according to a geometry-prescribed approach, so that the movement of the LV wall was imposed as a boundary condition of the fluid domain.

In a cardiac cycle, the ventricular motion is characterised by contraction and twist during systole, and dilation and untwist during diastole. To reproduce this peculiar movement, the

mesh motion functionality of ANSYS Fluent 18.1 was exploited, by compiling and loading a specifically set of User-Defined Functions (UDFs), which assigned a displacement to the mesh nodes. The result of the mesh motion is depicted in Figure 2.
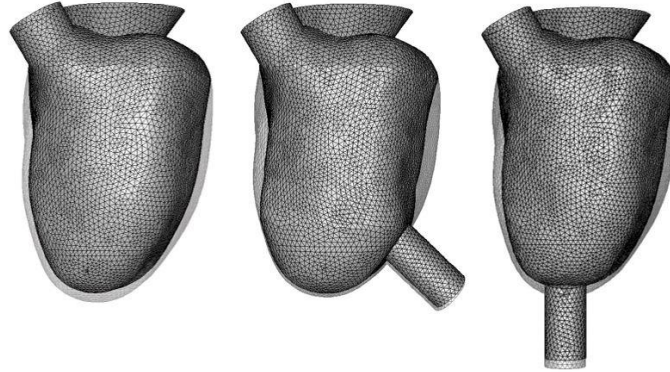
Figure 2: Superimposition of the end-systolic and end-diastolic configurations for the patient-specific models *pre*-implant (left), *post*-implant A (middle) and B (right). Image provided for an EF of 15%.

Results and Discussion

A fundamental role in determining LV hemodynamics is played by vortexes, given that these structures are responsible for blood mixing, proper cardiac filling and emptying in the diastolic and systolic phases, respectively. In this study, vortex dynamics was analysed applying the Q-criterion, in all the considered simulations sets.

In Figure 3, examples of the obtained 3D vortex fields are reported, for the healthy LV and for the pathological patient-specific LV, *pre* and *post* LVAD implantation. Results refer, for instance, to the systolic acceleration phase. Considering the *pre-implant* model, the detected vortexes were confined in the upper portion of the LV, resulting more compact and smaller the those analysed in *post-implant* configurations. A comparative analysis between the healthy condition and the *post-implant* configurations revealed a substantial difference in vortex dynamics. Indeed, during early systole, only two broad vortices were detected in the examined *post* LVAD implantation LV, while multiple vortical structures characterized the physiological scenario (Figure 3a and c).

SYSTOLE

HEALTHY   15% EF   15% EF + LVAD 2.20 L/min

t_1 = acceleration

(a)   (b)   (c)
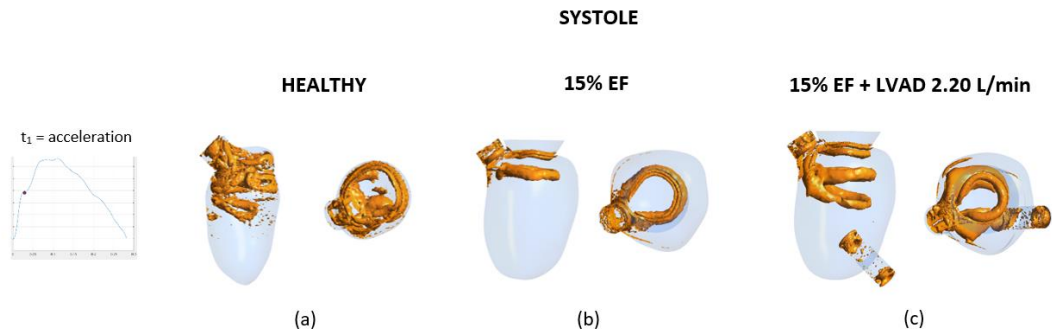
Figure 3: 3D vortex fields at the systolic acceleration, obtained applying the Q-criterion; Results are provided for: (a) the healthy LV model; (b) pathological LV *pre*-implant with a residual EF of 15%; (c) pathological LV *post*-implant for test condition 15% EF + LVAD 2.20 L/min.

The characterization of LV hemodynamics in the apical region was central in the present work, because this critical area is particularly prone to intraventricular thrombus formation. The evaluation of wall shear stress (WSS) on the apical portion of the ventricular wall was carried as a mean to assess blood stasis in the different simulated conditions. The WSS were extracted considering a complete cardiac cycle in three pre-defined regions close to the ventricular apex. The obtained results were compared to the WSS trends of a healthy ventricle, evaluated, with the same approach, in a previous study [20].

As it can be noticed, WSS peak values in the examined pathological cases (Figure 4) were approximately two order of magnitude lower than the physiological ones, and, when the residual EF% decreased from 15% to 5%, WSS were lowered of one order of magnitude.
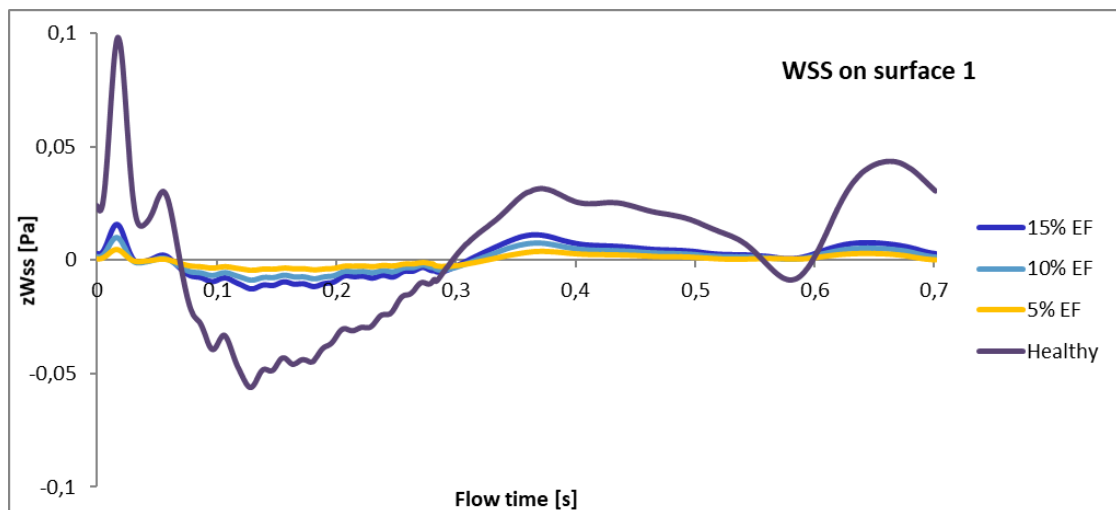
Figure 4: WSS trends on surface 1 for the healthy LV, and for 15%, 10%, and 5% residual EF.

According to our results, the decrease of residual LV contractility determined a significant reduction in blood velocity through the cardiac cycle, altering the LV hemodynamics in the apical region and generating stagnation areas.

Blood stasis is a recognized risk factor for intraventricular thrombosis as it promotes thrombus formation through the accumulation of both activated and sensitized platelets, which may get trapped in the area of blood stasis and exposed to low dynamic shear stress for elongated durations [15, 21-22].

When *post-implant* WSS trends, obtained in simulation Set 2, were compared with those from the *pre-implant* configuration (Set 1), result suggested that the implantation of a LVAD inflow cannula determined a further reduction of WSS peak values.

On the other hand, our results showed that WSS were strongly influenced by LV residual contractility and, to a lesser extent, by LVAD flow.

To identify the most hemodynamically favourable LVAD implantation configuration, WSS trends from the *post-implant* B simulation set were compared with corresponding data from the *post-implant* A simulation set. WSS peak values resulted to be one order of magnitude higher when the inflow cannula was modelled with an apical positioning. The obtained results suggested there might be a higher risk for thromboembolic events when the cannula was not in the apical configuration because of greater blood stagnation and because blood flow was slower in areas not directly along the path between the inlet (the mitral valve) and outlets (LVAD and aortic valve). Misalignment between the LV apical axis and the LVAD inflow cannula resulted in more convoluted blood trajectories, increasing the potential for platelets to be trapped in the LV, in particular in the space between the LV wall and the inflow cannula. Our results are in agreement with previous studies, which also showed that platelets linger significantly longer in the LV, and, in the process, accumulate high shear stress given their increased residence time in the MV-to-cannula pathway [23].

Conclusions

LVAD support is an established for patients suffering HF, both as bridge-to-transplantation and destination therapy. Despite the widespread clinical use of LVADs, there are a number of complications associated with LVAD therapy, the most relevant being those associated with the device-related thrombogenicity. In this study, the role of LV residual contractility as an additional thrombogenic factor was investigated, since the thrombus-favourable LV flow dynamics, in the pathological LV, was hypothesized to synergize to the mechanism of platelets activation and thrombus formation. Moreover, given that both the LV residual contractility and the LVAD-induced hemodynamics might have a role in altering LV hemodynamics promoting thrombogenesis, here we analysed the mutual interaction between these two factors.

According to our results, decreasing the LV residual contractility determine an increase in blood stasis in the apical region of the LV. Moreover, it resulted that blood stasis was strongly influenced by LV residual contractility and, to a lesser extent, by the LVAD flow rate. In addition, the obtained results proved a lower risk for thromboembolic events when the cannula was positioned in the apical configuration, because of lower blood stagnation and a more linear blood flow from the MV to the LVAD inflow cannula.

With this study we provide further mechanistic insights into the mechanisms related to intraventricular thrombus formation and thromboembolic complications in LVAD patients. In detail, the results of our study suggest that the LV residual contractility and LVAD inflow cannula insertion configuration are hemodynamic-associated variables that must be considered when facing with the LVAD-induced thrombogenicity.

References

(1) Molisso C, Molisso V. La cardiomiopatia dilatativa in ambito valutativo medico-legale. *G Ital Cardiol* 2007;8 (5):299-305.

(2) Roberts WC, Siegel RJ, McManus BM. Idiopathic dilated cardiomyopathy: analysis of 152 necropsy patients. *Am J Cardiol* 1987;60:1340-55.

(3) Feild BJ, Baxley WA, Russell RO Jr, *et al*. Left ventricular function and hypertrophy in cardiomyopathy with depressed ejection fraction. *Circulation* 1973;47:1022-31.

(4) Wallis DE, O'Connell JB, Henkin RE, Costanzo-Nordin MR, Scanlon PJ. Segmental wall motion abnormalities in dilated cardiomyopathy: a common finding and good prognostic sign. *J Am Coll Cardiol* 1984;4:674-9.

(5) Douglas PS, Morrow R, Ioli A, Reichek N. Left ventricular shape, afterload and survival in idiopathic dilated cardiomyopathy. *J Am Coll Cardiol* 1989;13:311-5.

(6) Starling RC, Moazami N, Silvestry SC, Ewald G, Rogers JG, Milano CA, Rame JE, Acker MA, Blackstone EH, Ehrlinger J, Thuita L, Mountis MM, Soltesz EG, Lytle BW, Smedira NG. Unexpected abrupt increase in left ventricular assist device thrombosis. *N Engl J Med*. 2014;370(1):33-40.

(7) Rogers JG, Pagani FD, Tatooles AJ, Bhat G, Slaughter MS, Birks EJ, Boyce SW, Najjar SS, Jeevanandam V, Anderson AS, Gregoric ID, Mallidi H, Leadley K, Aaronson KD, Frazier OH, Milano CA. Intrapericardial Left Ventricular Assist Device for Advanced Heart Failure. *N Engl J Med* 2017;376(5):451-460.

(8) Mehra MR, Naka Y, Uriel N, Goldstein DJ, Cleveland JC Jr, Colombo PC, Walsh MN, Milano CA1, Patel CB1, Jorde UP, Pagani FD, Aaronson KD, Dean DA, McCants K, Itoh A, Ewald GA, Horstmanshof D, Long JW, Salerno C; MOMENTUM 3 Investigators. A Fully Magnetically Levitated Circulatory Pump for Advanced Heart Failure. *N Engl J Med* 2017;376(5):440-450.

(9) Najjar SS, Slaughter MS, Pagani FD, Starling RC, McGee EC, Eckman P, Tatooles AJ, Moazami N, Kormos RL, Hathaway DR, Najarian KB, Bhat G, Aaronson KD3, Boyce SW; HVAD Bridge to Transplant ADVANCE Trial Investigators. An analysis of pump thrombus events in patients in the

HeartWare ADVANCE bridge to transplant and continued access protocol trial. *J Heart Lung Transplant* 2014; 33(1):23-34.

(10)   Rossini L, Martinez-Legazpi P, Vu V, *et al*. A clinical method for mapping and quantifying blood stasis in the left ventricle. *J Biomech*. 2016 July 26;49(11): 2152–2161.

(11)   Liu GM, Chen HB, Luo FL, Zhang Y, Sun HS, Zhou JY, Hu SS. Numerical Simulation of LVAD Inflow Cannulas with Different Tip. *International Journal of Chemical Engineering*, vol. 2012, Article ID 596960, 2012.

(12)   Ong CW, Dokos S, Chan BT, Lim E, Abed AA, Osman NABA, Kadiman S, Lovell NH. Numerical investigation of the effect of cannula placement on thrombosis. *Theor Biol Med Model* 2013; 10:35.

(13)   Ong CW, Chan T, Lim E, Abu Osman NA, Abed AA, Dokos S, Lovell NH. Fluid Structure Interaction Simulation of Left Ventricular Flow Dynamics under Left Ventricular Assist Device Support. *Conf Proc IEEE Eng Med Biol Soc*. 2012; 2012: 6293-6.

(14)   Liao S, Simpson B, Neidlin M, Kaufmann TAS, Li Z, Woodruff MA, Gregory SD. Numerical prediction of thrombus risk in an anatomically dilated left ventricle: the effect of inflow cannula designs. *Biomed Eng Online*. 2016 Dec   28; 15(Suppl 2): 136.

(15)   Prisco AR, Aliseda A, Beckman JA, Mokadam NA, Mahr C, Garcia GJM. Impact of LVAD Implantation Site on Ventricular Blood Stagnation. *ASAJO J*. 2017 Jul/Aug; 63(4): 392-400.

(16)   Liao S, Neidlin M, Li Z, Simpson B, Gregory SD. Ventricular flow dynamics with varying LVAD inflow cannula lengths: In-silico evaluation in a multiscale model. *J Biomech* 2018 Apr 27; 72: 106-115.

(17)   Loerakker S, Cox LGE, van Heijst GJF, de Mol BAJM, van de Vosse FN. Influence of dilated cardiomyopathy and a left ventricular assist device on vortex dynamics in the left ventricle. Computer Methods in Biomechanics and Biomedical Engineering 2008; 11(6): 649-660.

(18)   Chan BT, Ong CW, Lim E, Abu Osman NA, Al Abed A, Lovell NH, Dokos S. Simulation of Left Ventricle Flow Dynamics with Dilated Cardiomyopathy during the Filling Phase. Annual International Conference of the IEEE Engineering in

Medicine and Biology Society. IEEE Engineering in Medicine and Biology Society. Conference. 2012; 6289-92.

(19) Bavo AM, Pouch AM, Degroote J, Vierendeels J, Gorman JH, Gorman RC, Segers P. Patient-specific CFD simulation of intraventricular haemo-dynamics based on 3D ultrasound imaging. Biomed Eng OnLine. 2016; 15(107): 144-150.

(20) Apostoli A, Bianchi V. Development of an in vitro platform to characterize Endothelial Cell-Platelet pro-thrombotic interaction mechanisms associated with Left Ventricular Assist Device therapy. http://hdl.hsndle.net/10589/135360.

(21) Sheriff J, Bluestein D, Girdhar G, Jesty J. High-Shear Stress Sensitizes Platelets to Subsequent Low-Shear Conditions. *Ann Biomed Eng.* 2010 April;38(4):1442-1450.

(22) Yin W, Shanmugavelayudam SK, Rubenstein DA. The effect of physiologically relevant dynamic shear stress on platelet and endothelial cell activation. *Thrombosis Res* (2011)127:235-241.

(23) Chivukula VK, Beckman JA, Prisco AR, Dardas T, Lin S, Smith JW, Mokadam NA, Aliseda A, Mahr C. Left Ventricular Assist Device Inflow Cannula Angle and Thrombosis Risk. *Circ Heart Fail*. 2018 Apr;11(4):e004325.

Sommario

Introduzione

L'insufficienza cardiaca (IC) è una grave condizione patologica cronica, caratterizzata dall'incapacità del cuore di pompare sangue sufficiente a sopperire ai bisogni degli organi del corpo. Circa la metà dei pazienti con IC è affetta da cardiomiopatia dilatativa (CMD), una sindrome caratterizzata da ingrossamento, ipocinesi miocardica e riduzione della contrattilità complessiva (tipicamente < 40%) del ventricolo sinistro o di entrambi [1-4], che acquisiscono una forma patologica quasi sferica [5].

I pazienti affetti da CMD in stato avanzato hanno un numero limitato di opzioni terapeutiche. Pochi pazienti risultano idonei al trapianto cardiaco, considerato il trattamento di riferimento per l'IC in fase terminale. Il trapianto cardiaco è soggetto a diverse limitazioni, quali gli stringenti criteri di selezione e la mancanza di donatori compatibili. Di conseguenza, è stato introdotto l'uso di dispositivi per l'assistenza ventricolare sinistra (LVAD), il cui obiettivo è fornire un supporto o sostituire completamente la funzione pompante del ventricolo sinistro (VS).

L'attuale generazione di LVAD è costituita da cinque componenti fondamentali: la cannula di afflusso, la pompa (centrifuga o assiale), la cannula di efflusso, la linea di trasmissione percutanea e il controllore esterno (Figura 1).
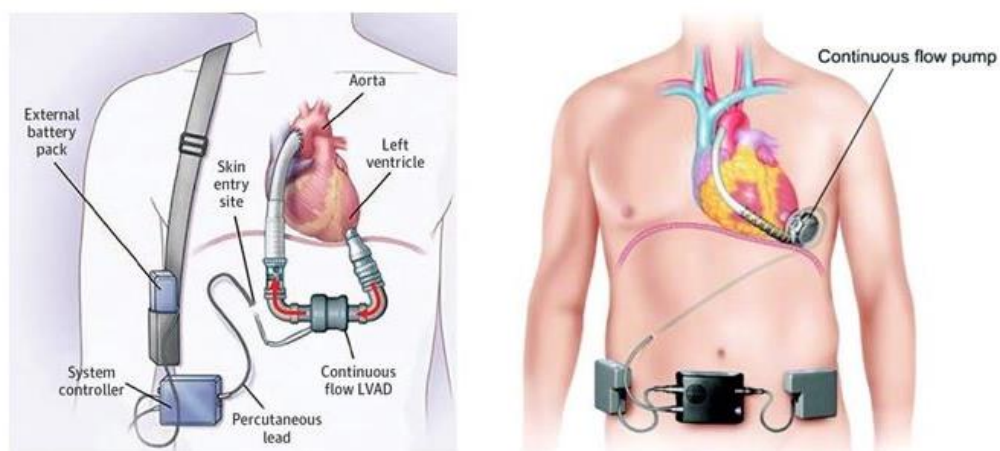

Figura 1: Componenti LVAD. Sinistra: la pompa è posizionata nella cavità peritoneale. Destra: la pompa è a contatto col miocardio ventricolare.

Nonostante l'utilizzo diffuso, i VAD provocano alcune complicazioni *post* impianto, prima tra tutte la trombosi. È stato dimostrato [6-9] che la formazione di trombi intraventricolari si sviluppa principalmente all'interfaccia tra il miocardio e la superficie della cannula; il trombo, ingrandendosi progressivamente, può distaccarsi ed essere ingerito dalla pompa, aumentando il rischio di formazione di trombi all'interno del dispositivo, e di eventi tromboembolici a valle di esso.

Diversi meccanismi sono stati proposti come promotori della formazione di trombi intraventricolari:

- l'interazione tra il sangue e il materiale artificiale del dispositivo;
- la funzione protrombotica delle piastrine: piastrine attivate e/o sensibilizzate da sforzi di taglio particolarmente elevati all'interno della pompa, una volta rientrate nel VS, tendono ad aggregarsi e a generare trombi, a causa delle condizioni protrombotiche lì presenti;
- l'alterazione dell'emodinamica ventricolare (aree di ristagno e zone di ricircolo) dovuta a:

    i.   l'aumento di volume del VS e la ridotta contrattilità miocardica;
    ii. il posizionamento della cannula del LVAD.

La CMD determina la variazione dell'emodinamica ventricolare: mentre in condizioni fisiologiche, il sangue all'interno del VS è interamente sostituito ogni 2-3 battiti, in presenza di una ridotta contrattilità del miocardio, il moto del fluido è significativamente alterato dalla presenza di vortici, nei quali il sangue rimane intrappolato e sottoposto a rotazione durante il ciclo cardiaco [10]. In particolare, si creano delle zone di ristagno nella regione apicale, dove si innesca l'attivazione del processo trombotico.

Nel presente lavoro, si ipotizza che la contrattilità residua di un ventricolo dilatato possa agire da fattore trombogenico aggiuntivo, in quanto la severità dell'IC ha un ruolo nella modifica dell'emodinamica ventricolare. Questa alterazione, infatti, potrebbe provocare

l'instaurarsi di condizioni protrombotiche, specialmente nella regione apicale del VS, dove è inserita la cannula del LVAD.

Pertanto, considerato che sia la contrattilità residua del VS che la configurazione d'impianto del LVAD hanno un ruolo nel determinare l'emodinamica del VS, nel presente studio, si sono analizzate le interazioni mutue tra questi due fattori.

Quindi, il presente lavoro è focalizzato sullo sviluppo di un modello fluido dinamico computazionale (CFD), volto ad analizzare l'emodinamica di un ventricolo sinistro, paziente specifico, supportato da LVAD. In dettaglio, si è analizzata l'emodinamica ventricolare per un VS *post* impianto, variando selettivamente: *i)* la contrattilità residua ventricolare (tramite la quale si sono modellati differenti gradi di IC) e *ii)* il posizionamento della cannula del LVAD. Le variabili emodinamiche (wall shear stress, aree di ristagno e zone di ricircolo) sono state analizzate prima e dopo l'impianto del LVAD.

Stato dell'Arte

In letteratura, diversi studi computazionali [11-16] si sono concentrati sulla caratterizzazione dei disturbi emodinamici e del potenziale trombogenico del VS in presenza di LVAD, fornendo una descrizione dettagliata del campo di moto del fluido nel VS, attraverso profili di velocità del sangue, distribuzioni di sforzi di taglio in parete (Wall shear stress, WSS), e pattern di formazione e sviluppo di vortici. La geometria della cannula, la sua posizione nel miocardio, la profondità e l'angolo di inserzione sono stati riconosciuti come fattori in grado di alterare profondamente la fluidodinamica del VS.

Ad ogni modo, due carenze fondamentali contraddistinguono la letteratura esaminata. *In primis*, il movimento delle pareti del VS è replicato solo in termini di contrazione e la mancanza del contributo torsionale impedisce di ottenere simulazione realistiche della dinamica cardiaca [17-19]. In secondo luogo, la caratterizzazione dell'emodinamica VS-LVAD prevede, di solito, che il VS sia modellizzato come un corpo rigido e statico, trascurando ogni contrattilità residua [11, 14-15].

Conseguentemente all'impianto del LVAD, il volume del VS si riduce a causa del rimodellamento cardiaco e la contrattilità ventricolare nativa può essere parzialmente recuperata. Quindi, si ritiene che l'aggiunta del movimento ventricolare in una simulazione

CFD possa modificare le regioni di possibile ristagno e la velocità di ricambio del sangue nel VS.

Di conseguenza, per superare le limitazioni di cui sopra, in questo lavoro la dinamica cardiaca è stata replicata includendo sia la contrazione che la torsione, applicando un approccio "prescribed moving boundaries", ovvero assemblando un insieme di equazioni matematiche per formulare e modellizzare il movimento ventricolare, per gli scenari *pre* e *post* impianto.

Materiali e Metodi

Nel presente lavoro, sono stati definiti tre set di simulazione:

- Set 1 (*Pre impianto*): il set comprende tre simulazioni; il dominio fluidodinamico è costituito da un VS paziente specifico, patologicamente dilatato. Sono state eseguite delle simulazioni fluidodinamiche transitorie dell'intero ciclo cardiaco, considerando tre diversi frazioni di eiezione (FE) (15% - 10% - 5%), tramite le quali è stata quantificata la contrattilità residua del VS. Questi valori di FE corrispondono a livelli crescenti di insufficienza cardiaca, da moderata a grave.
  Questo approccio numerico ha permesso di determinare il ruolo della contrattilità residua come possibile fattore trombogenico.

- Set 2 (*Post impianto A*): il modello CFD si basa sullo stesso VS paziente specifico del Set 1, dopo l'impianto della cannula. Il posizionamento di quest'ultima è stato derivato dai dati clinici e dal processo di ricostruzione. Il set comprende una matrice di 8 condizioni di test, ottenuta combinando 4 diversi valori di FE (0 - 5 - 10 - 15%) con opportuni livelli di supporto alla circolazione (portate volumetriche del LVAD), in modo tale da ottenere una gittata cardiaca complessiva di 5 L/min. In questo modo, è stato possibile valutare l'interazione tra la contrattilità residua del miocardio e la portata del LVAD.

- Set 3 (*Post impianto B*): Il set consta di 2 condizioni di test, selezionate a partire dalla matrice di simulazione del Set 2. Esse sono state scelte considerando la gittata cardiaca totale (GC) fornita al paziente, definita come la somma della gittata residua nativa e della portata fornita dal LVAD. La GC di riferimento è stata impostata pari a 5 L/min, una condizione che mima la GC media a riposo, in modo tale da riferirsi a condizioni cliniche reali. In questo set, è stata variata la posizione della cannula rispetto a quella del Set 2, cosicché l'asse longitudinale della cannula intersechi l'apice del VS e il centro dell'orifizio mitralico.

  L'obiettivo consiste nel quantificare l'impatto del posizionamento della cannula sulla trombosi intraventricolare, in modo da identificare la configurazione di impianto più favorevole dal punto di vista emodinamico.

Un'analisi elettrocardiografica trans-toracica 3D (3DTTE) è stata eseguita su un candidato all'impianto del LVAD. I dati 3DTTE sono stati utilizzati per estrarre il profilo del VS patologico, paziente specifico, nella configurazione di fine diastole, tramite una procedura di ricostruzione sviluppata dal Gruppo di Biomeccanica del Politecnico di Milano. Questo lavoro è stato realizzato in collaborazione con il team del Advanced Heart Failure and Mechanical Circulatory Program dell'Istituto Scientifico San Raffaele e dell'Università Vita Salute San Raffaele di Milano.

Il dominio fluido del VS, nella configurazione *pre* impianto, è stato poi ottenuto utilizzando il software CAD 3D SpaceClaim (ANSYS 18.1). Per garantire un flusso completamente sviluppato in fase di simulazione, è stata creata una porzione fittizia/paradigmatica della camera atriale sinistra e dell'aorta prossimale.

Per ottenere, invece, il dominio fluido dei modelli *post* impianto A e B, è stata aggiunta una cannula, rispettivamente ricostruendo la sua posizione paziente specifica e sfruttando un posizionamento apicale, coerentemente con il set-up di simulazione precedentemente descritto.

Il movimento della parete ventricolare è stato definito tramite un set di equazioni matematiche, secondo un approccio "geometry-prescribed", in modo tale che il movimento della parete del VS sia imposto sotto forma di condizione al contorno per il dominio fluido.

In un ciclo cardiaco, il movimento del miocardio è caratterizzato da contrazione e torsione durante la sistole, e da dilatazione e torsione inversa durante la diastole. Per riprodurre questo movimento particolare, è stata sfruttata una funzionalità di ANSYS Fluent 18.1, che ha permesso di compilare e caricare una User Defined Function (UDF), creata appositamente. La UDF assegna uno spostamento ai nodi della mesh mobile. Il risultato del movimento applicato è mostrato in Figura 2.
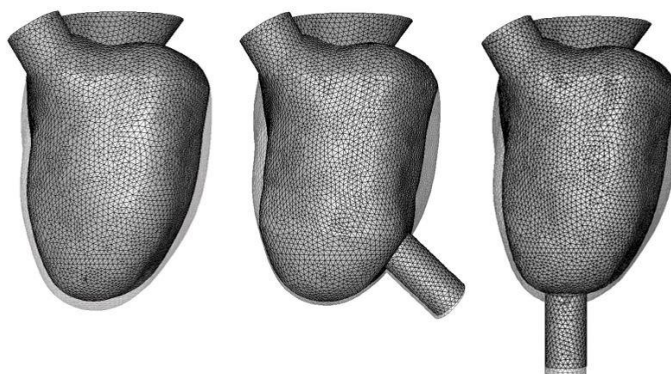

Figura 2: Sovrapposizione delle configurazioni di fine sistole e fine diastole per i modelli paziente specifico *pre* impianto (sinistra), *post* impianto A (centro) e B (destra). Le immagini sono state ottenute per un valore di FE% pari al 15%.

Risultati e Discussione

La formazione e l'evoluzione di vortici ha un ruolo fondamentale per l'emodinamica ventricolare, dato che queste strutture sono responsabili del rimescolamento sanguigno, del corretto riempimento diastolico e dell'eiezione sistolica. Nel presente lavoro, la dinamica dei vortici è stata analizzata applicando il Q-criterion, per tutti i set di simulazione considerati. In Figura 3, sono riportati alcuni esempi di vortici, estratti dal modello fisiologico del VS, e da due configurazioni patologiche *pre* e *post* impianto. I risultati mostrati si riferiscono alla fase di accelerazione sistolica. Per il modello *pre* impianto, è possibile notare che i vortici individuati sono concentrati nella porzione superiore del VS, risultando, inoltre, più compatti e di minori dimensioni rispetto a quelli analizzati nelle configurazioni *post* impianto. Un'analisi comparativa tra la condizione fisiologica e le configurazioni *post* impianto ha evidenziato una sostanziale differenza nella dinamica dei

vortici. Infatti, durante le fasi iniziali della sistole, le configurazioni *post* impianto esaminate sono caratterizzate dalla presenza di soli due vortici di grandi dimensioni, mentre strutture vorticose multiple vengono a formarsi nello scenario fisiologico (Figura 3a e c).
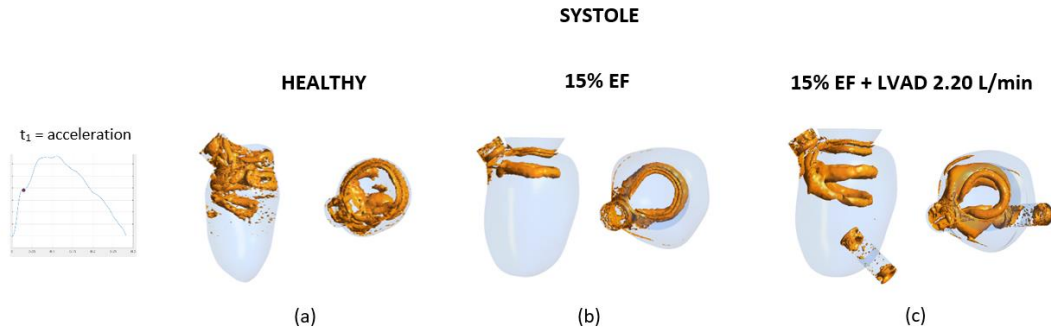
Figura 3: Vortici 3D al picco di accelerazione sistolica, ottenuti applicando il Q-criterion; I risultati si riferiscono a: (a) modello fisiologico del VS; (b) VS patologico *pre* impianto con FE residua di 15%; (c) VS patologico *post* impianto per la condizione di test 15% FE + LVAD 2.20 L/min.

La caratterizzazione dell'emodinamica ventricolare nella regione apicale è un punto centrale del presente lavoro di tesi, poiché questa regione critica del VS è particolarmente propensa alla formazione di trombi intraventricolari. Si è proceduto all'analisi dei WSS nella regione apicale del miocardio ventricolare per quantificare la stasi sanguigna. L'andamento dei WSS è stato estratto considerando un ciclo cardiaco completo, in tre regioni predefinite, in prossimità dell'apice ventricolare.

Figura 4: Andamenti di WSS, per la superficie 1, per il VS sano, e per i ventricoli patologici con FE residua pari a 15%, 10% e 5%.

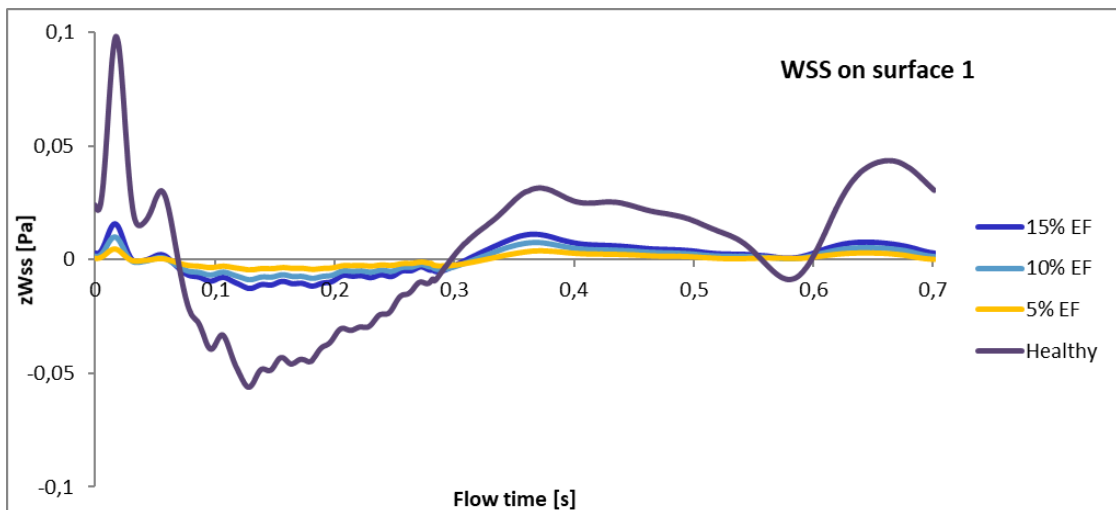I risultati ottenuti sono stati confrontati con gli andamenti di WSS relativi ad un ventricolo fisiologico, valutati, con la stessa metodologia, in uno studio precedente [20].

Come evidenziato in Figura 4, i valori di picco dei WSS nei casi patologici presi in esame sono circa due ordini di grandezza inferiori rispetto a quelli ottenuti nel caso di VS sano; inoltre, al diminuire della FE residua (dal 15% al 5%), si assiste ad un abbassamento dei picchi di WSS di un ordine di grandezza.

Valori decrescenti di FE residua determinano una riduzione significativa della velocità di movimento del sangue durante il ciclo cardiaco, modificando il campo di moto nell'apice così drasticamente da creare delle regioni di ristagno.

La stasi sanguigna è stata riconosciuta come uno dei fattori di rischio principali per la trombosi intraventricolare, poiché è in grado di promuovere la formazione di trombi tramite l'accumulo di piastrine sia nello stato attivato che sensibilizzate. In particolare, per effetto del ricambio limitato, le piastrine sensibilizzate potrebbero restare intrappolate all'interno del VS ed essere sottoposte a stress di parete dinamici e di bassa intensità, per periodi relativamente lunghi [15, 21-22].

I risultati ottenuti mostrano che i WSS sono fortemente influenzati dalla contrattilità residua del VS e, in misura minore, dalla portata del LVAD.

Infine, per identificare la configurazione di impianto più favorevole dal punto di vista emodinamico, le curve di WSS relative alle simulazioni del Set 3 (modello *post* impianto B) sono state comparate con i dati corrispondenti estratti dal Set 2 (modello *post* impianto A). Il confronto ha evidenziato che i valori di picco di WSS relativi al posizionamento apicale della cannula sono di un ordine di grandezza più elevati. I risultati ottenuti suggeriscono, quindi, che il rischio di potenziali eventi tromboembolici sia più elevato quando la cannula del VAD non si trova in posizione apicale, a causa della maggiore stasi riscontrata e di un movimento del flusso sanguigno particolarmente lento in corrispondenza di zone interne al VS, non posizionate direttamente tra la valvola mitrale e le sezioni di uscita (LVAD e valvola aortica). Il disallineamento tra l'asse ventricolare e la cannula del LVAD comporta che il flusso sanguigno segua traiettorie contorte, aumentando la possibilità che le piastrine attivate restino intrappolate nel VS, in particolare nella regione apicale, nello spazio che viene a crearsi tra la parete del miocardio e la

cannula. I risultati ottenuti sono in accordo con studi precedenti che hanno mostrato come una prolungata permanenza delle piastrine nel VS determini la loro attivazione [23].

Conclusioni

L'impianto di LVAD è un trattamento consolidato per i pazienti che soffrono di IC, sia come supporto alla circolazione in attesa del trapianto di cuore, sia come terapia definitiva. Nonostante l'ampio uso in clinica, numerose sono le complicanze associate all'impianto di LVAD, la più rilevante delle quali è la trombogenicità del dispositivo. Nel presente lavoro, si è cercato di definire il ruolo della contrattilità residua del VS come possibile fattore trombogenico, in quanto l'emodinamica protrombotica del VS, indotta dalla CMD, è in grado di innescare l'attività piastrinica, mentre la cannula del LVAD agisce da substrato per la formazione, l'apposizione e la progressiva crescita del trombo. Inoltre, considerato che sia la contrattilità residua del VS che l'impianto di un LVAD influenzano la fluidodinamica intraventricolare, il presente lavoro si è concentrato sulle interazioni mutue tra questi due fattori.

I risultati dello studio dimostrano che al diminuire della contrattilità residua del VS corrisponde una stasi di entità via via maggiore in corrispondenza dell'apice ventricolare. Inoltre, è stato possibile evidenziare come la stasi sanguigna sia fortemente influenzata dalla contrattilità residua ventricolare e, in misura minore, dalla portata imposta dal LVAD. In aggiunta, i risultati ottenuti dimostrano un rischio tromboembolico minore in caso di posizionamento apicale della cannula, grazie al minor ristagno in zona apicale e ad una traiettoria di movimento del flusso sanguigno che collega direttamente la valvola mitrale con la cannula.

Con questo studio si è fornita una migliore conoscenza dei meccanismi di formazione di trombi intraventricolari e delle complicazioni tromboemboliche nei pazienti assistiti da LVAD. In particolare, i risultati di questo studio suggeriscono che la contrattilità residua del VS e il posizionamento della cannula del LVAD sono delle variabili che influenzano l'emodinamica del VS e che devono essere prese in considerazione quando si valuta la trombogenicità indotta dal LVAD.

Bibliografia

(1)   Molisso C, Molisso V. La cardiomiopatia dilatativa in ambito valutativo medico-legale. *G Ital Cardiol* 2007;8 (5):299-305.

(2)   Roberts WC, Siegel RJ, McManus BM. Idiopathic dilated cardiomyopathy: analysis of 152 necropsy patients. *Am J Cardiol* 1987;60:1340-55.

(3)   Feild BJ, Baxley WA, Russell RO Jr, *et al*. Left ventricular function and hypertrophy in cardiomyopathy with depressed ejection fraction. *Circulation* 1973;47:1022-31.

(4)   Wallis DE, O'Connell JB, Henkin RE, Costanzo-Nordin MR, Scanlon PJ. Segmental wall motion abnormalities in dilated cardiomyopathy: a common finding and good prognostic sign. *J Am Coll Cardiol* 1984;4:674-9.

(5)   Douglas PS, Morrow R, Ioli A, Reichek N. Left ventricular shape, afterload and survival in idiopathic dilated cardiomyopathy. *J Am Coll Cardiol* 1989;13:311-5.

(6)   Starling RC, Moazami N, Silvestry SC, Ewald G, Rogers JG, Milano CA, Rame JE, Acker MA, Blackstone EH, Ehrlinger J, Thuita L, Mountis MM, Soltesz EG, Lytle BW, Smedira NG. Unexpected abrupt increase in left ventricular assist device thrombosis. *N Engl J Med*. 2014;370(1):33-40.

(7)   Rogers JG, Pagani FD, Tatooles AJ, Bhat G, Slaughter MS, Birks EJ, Boyce SW, Najjar SS, Jeevanandam V, Anderson AS, Gregoric ID, Mallidi H, Leadley K, Aaronson KD, Frazier OH, Milano CA. Intrapericardial Left Ventricular Assist Device for Advanced Heart Failure. *N Engl J Med* 2017;376(5):451-460.

(8)   Mehra MR, Naka Y, Uriel N, Goldstein DJ, Cleveland JC Jr, Colombo PC, Walsh MN, Milano CA1, Patel CB1, Jorde UP, Pagani FD, Aaronson KD, Dean DA, McCants K, Itoh A, Ewald GA, Horstmanshof D, Long JW, Salerno C; MOMENTUM 3 Investigators. A Fully Magnetically Levitated Circulatory Pump for Advanced Heart Failure. *N Engl J Med* 2017;376(5):440-450.

(9)   Najjar SS, Slaughter MS, Pagani FD, Starling RC, McGee EC, Eckman P, Tatooles AJ, Moazami N, Kormos RL, Hathaway DR, Najarian KB, Bhat G, Aaronson KD3, Boyce SW; HVAD Bridge to Transplant ADVANCE Trial Investigators. An analysis of pump thrombus events in patients in the

HeartWare ADVANCE bridge to transplant and continued access protocol trial. *J Heart Lung Transplant* 2014;33(1):23-34.

(10) Rossini L, Martinez-Legazpi P, Vu V, *et al*. A clinical method for mapping and quantifying blood stasis in the left ventricle. *J Biomech*. 2016 July 26;49(11): 2152–2161.

(11) Liu GM, Chen HB, Luo FL, Zhang Y, Sun HS, Zhou JY, Hu SS. Numerical Simulation of LVAD Inflow Cannulas with Different Tip. *International Journal of Chemical Engineering*, vol. 2012, Article ID 596960, 2012.

(12) Ong CW, Dokos S, Chan BT, Lim E, Abed AA, Osman NABA, Kadiman S, Lovell NH. Numerical investigation of the effect of cannula placement on thrombosis. *Theor Biol Med Model* 2013; 10:35.

(13) Ong CW, Chan T, Lim E, Abu Osman NA, Abed AA, Dokos S, Lovell NH. Fluid Structure Interaction Simulation of Left Ventricular Flow Dynamics under Left Ventricular Assist Device Support. *Conf Proc IEEE Eng Med Biol Soc*. 2012; 2012: 6293-6.

(14) Liao S, Simpson B, Neidlin M, Kaufmann TAS, Li Z, Woodruff MA, Gregory SD. Numerical prediction of thrombus risk in an anatomically dilated left ventricle: the effect of inflow cannula designs. *Biomed Eng Online*. 2016 Dec 28; 15(Suppl 2): 136.

(15) Prisco AR, Aliseda A, Beckman JA, Mokadam NA, Mahr C, Garcia GJM. Impact of LVAD Implantation Site on Ventricular Blood Stagnation. *ASAJO J*. 2017 Jul/Aug; 63(4): 392-400.

(16) Liao S, Neidlin M, Li Z, Simpson B, Gregory SD. Ventricular flow dynamics with varying LVAD inflow cannula lengths: In-silico evaluation in a multiscale model. *J Biomech* 2018 Apr 27; 72: 106-115.

(17) Loerakker S, Cox LGE, van Heijst GJF, de Mol BAJM, van de Vosse FN. Influence of dilated cardiomyopathy and a left ventricular assist device on vortex dynamics in the left ventricle. Computer Methods in Biomechanics and Biomedical Engineering 2008; 11(6): 649-660.

(18) Chan BT, Ong CW, Lim E, Abu Osman NA, Al Abed A, Lovell NH, Dokos S. Simulation of Left Ventricle Flow Dynamics with Dilated Cardiomyopathy during the Filling Phase. Annual International Conference of the IEEE Engineering in

Medicine and Biology Society. IEEE Engineering in Medicine and Biology Society. Conference. 2012; 6289-92.

(19)   Bavo AM, Pouch AM, Degroote J, Vierendeels J, Gorman JH, Gorman RC, Segers P. Patient-specific CFD simulation of intraventricular haemo-dynamics based on 3D ultrasound imaging. Biomed Eng OnLine. 2016; 15(107): 144-150.

(20)   Apostoli A, Bianchi V. Development of an in vitro platform to characterize Endothelial Cell-Platelet pro-thrombotic interaction mechanisms associated with Left Ventricular Assist Device therapy. http://hdl.hsndle.net/10589/135360.

(21)   Sheriff J, Bluestein D, Girdhar G, Jesty J. High-Shear Stress Sensitizes Platelets to Subsequent Low-Shear Conditions. *Ann Biomed Eng.* 2010 April;38(4):1442-1450.

(22)   Yin W, Shanmugavelayudam SK, Rubenstein DA. The effect of   physiologically relevant dynamic shear stress on platelet and endothelial cell activation. *Thrombosis Res* (2011)127:235-241.

(23)   Chivukula VK, Beckman JA, Prisco AR, Dardas T, Lin S, Smith JW, Mokadam N A, Aliseda A, Mahr C. Left Ventricular Assist Device Inflow Cannula Angle and Thrombosis Risk. *Circ Heart Fail*. 2018 Apr;11(4):e004325.

1.   Introduction

In this chapter, the clinical relevance of heart failure (HF) and, in particular of dilated cardiomyopathy leading to HF, is presented: the syndrome morphologic features are discussed in detail, as well as the alterations induced by the pathology on intraventricular hemodynamics.

A viable, long-term treatment option for patients suffering HF, alternative to cardiac transplantation, is the surgical implantation of a Ventricular Assist Device (VAD), a mechanical pump meant to partially, or totally support the cardiac functionality, thus enhancing hemodynamic restoration.

Despite the widespread clinical use of VADs, there are a number of complications associated with VAD therapy, the most relevant being the device-related thrombogenicity.

Cardiac hemodynamics, in a failing heart, is severely compromised due to the reduced myocardial contractility; moreover, stagnation zones and recirculation patterns in the ventricular apical region create an environment favourable to thrombus formation and growth. In addition, VAD implantation was proven to further enhance thrombogenicity.

Hence, it is of paramount importance to comprehensively identify possible factors promoting thrombus formation, in order to limit/reduce the device thrombogenicity, that is limiting the VAD-related detrimental impact on haemostasis and coagulation.

1.1. Heart Failure and Dilated Cardiomyopathy

Heart failure (HF) is a severe pathological chronic condition where the heart cannot pump enough blood to support the needs of other organs in the body. Affecting around 1–2% of adults in developed countries, HF prevalence increases markedly with age [1-2].

The burden of heart failure in Europe is substantial and likely to grow over time. HF is the leading cause of hospitalisation in people over the age of 65 and carries a high cost to healthcare systems (Figure 1.1). It also exerts a significant economic burden to patients, their families and society in general [3].
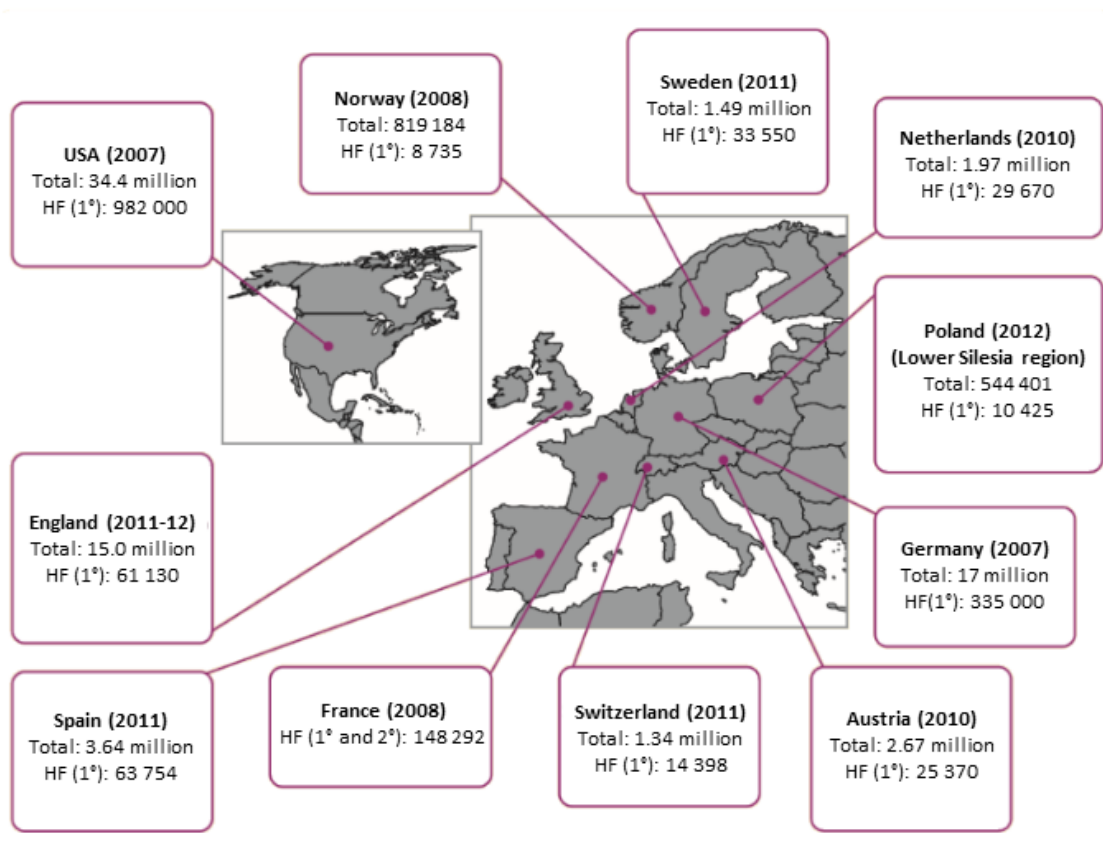

Figure 1.1: Hospitalizations for heart failure in Europe and the USA. HF (1°/2°), number of hospitalizations for heart failure as primary/secondary diagnosis.

Approximately half of the patients with HF is affected by dilated cardiomyopathy (DCM), a syndrome characterized by enlargement, wall hypokinesis, and reduction of the overall contractility of left or both ventricles [4-7], which acquire a pathological-dilated nearly spherical shape [8] (Figure 1.2).
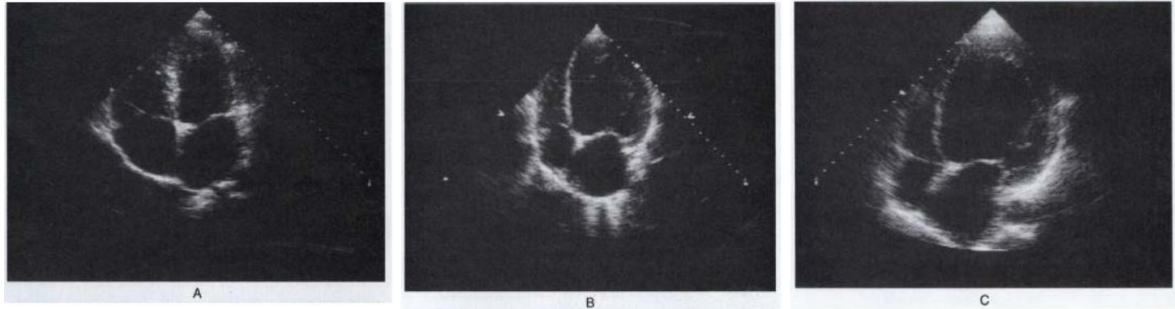

Figure 1.2: Apical four-chamber echocardiographic views of a subject with a structurally normal heart (A). Patient with moderate depression of left ventricular systolic function (B). Patient with advanced dilated cardiomyopathy (C) . In panel B, there is evidence of mild dilatation of the left ventricular cavity (end-diastolic diameter, 60 mm); the wall thickness is normal. In panel C, the residual left ventricular ejection fraction is 18%, and there is evidence of marked dilatation of the cavity (end-diastolic diameter, 86 mm) and marked enlargement of the left atrium.

When overloaded, the myocardium attempts to dampen wall shear stress through structural adaptation phenomena, the most relevant one being hypertrophy. At first, it provides hemodynamic compensation; thereafter, biochemical and structural modifications in the myocardium lead to ventricular remodelling, characterized by gradual dilation, reduction in the wall thickness, and increase in wall shear stress [9-11].

In Table 1.1, typical left ventricle end-diastolic parameters indicating a dilated cardiomyopathy are reported.

LV end-diastolic diameter	LV end-diastolic volume	
> 6 cm	> 110 ml/m^2	Symptomatic of a noticeable left ventricular enlargement, of a ventricular dysfunction, and of a negative prognosis for morbidity as well as for mortality.
> 7 cm	> 200 ml/m^2	Symptomatic of a severe left ventricular dilatation, and of serious and irreversible heart failure.

Table 1.1: Left Ventricle end-diastolic parameters [12-15].

DCM is characterised by both systolic and diastolic dysfunctions, in which the ability of the left ventricle (LV) to contract and pump blood during systole, and achieve a complete relaxation in diastole, is reduced or completely compromised.

In a normal heart (Figure 1.3a), about 50% of the blood in the LV is ejected into the aorta as the chamber contracts; this is known as the Ejection Fraction (EF).

In systolic dysfunction (Figure 1.3b), changes to the LV (enlargement of the chamber and impaired contractility) mean that a much smaller volume of blood (typically < 40%) is ejected. Systolic dysfunction, leading to systolic HF, is, therefore, also known as heart failure with reduced ejection fraction (HF-REF).

Impaired filling of the LV (diastolic dysfunction) is the main factor underlying the development of diastolic heart failure (Figure 1.3c). Characteristic changes of the heart include thickening of the left ventricular wall and enlargement of the left atrium.
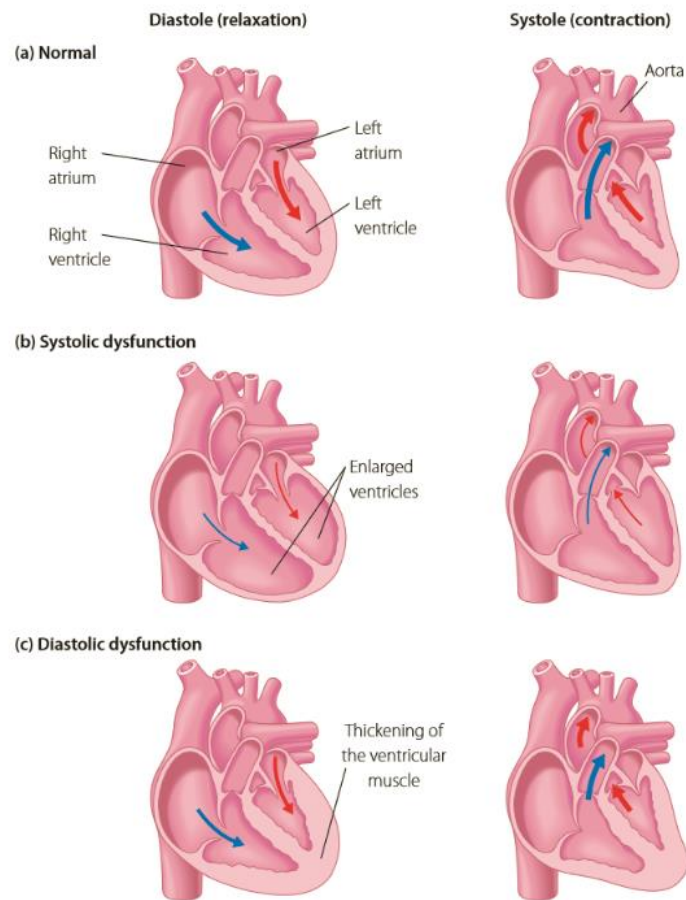
Figure 1.3: Systolic and diastolic dysfunctions.

Diastolic heart failure is also known as heart failure with preserved ejection fraction (HF-PEF). Compared with HF-REF, patients with HF-PEF are generally older, more frequently female and most have a history of hypertension [16-17]. HF-PEF is becoming more common; however, there are currently few effective treatments for HF-PEF [18].

In patients with DCM, there is risk of systemic or pulmonary embolization, because blood stasis and reduced shear rate in the hypocontractile ventricle lead to the activation of coagulation processes, so that long-term anticoagulation therapies are needed [19].

Patients with advanced DCM leading to HF have limited treatment options. Only a small number of them may qualify for cardiac transplantation, which is the treatment of choice for end-stage HF. Heart transplantation is restricted by stringent selection criteria and lack of availability of donor hearts. Consequently, ventricular assist devices (VADs) implantation has been introduced as an alternative, long-term, viable treatment to heart transplantation. A VAD is a surgically implanted mechanical pump that is implanted into the heart in order to provide full or partial mechanical circulatory support to one (Left-VAD – Right-VAD) or both ventricles (Bi-VAD). VADs are used clinically as destination therapy, as bridge to transplant or, as bridge to recovery to allow myocardial remodelling.

1.2. Left Ventricular Assist Devices

1.2.1. Components and Functions

The profound limitations in survival, functional status, and quality of life due to advanced HF can be to date treated thanks to Left Ventricular Assist Device (LVAD) implantation, a therapeutic option that provides circulatory support while waiting for heart transplantation, or is employed as a definitive therapy alternative to transplant (i.e. destination therapy). The components of a LVAD are (Figure 1.4):

- an inflow cannula, inserted into the apex of the left ventricle;
- a pump (pulsatile or continuous) placed within the abdominal wall or peritoneal cavity, or "on board" of the heart itself;
- an outflow cannula, anastomosed to the ascending aorta;
- a percutaneous drive line which carries the electrical cable and air vent to the external battery packs;
- an electronic controller, that monitors LVAD performances and provides input for the pump operation.
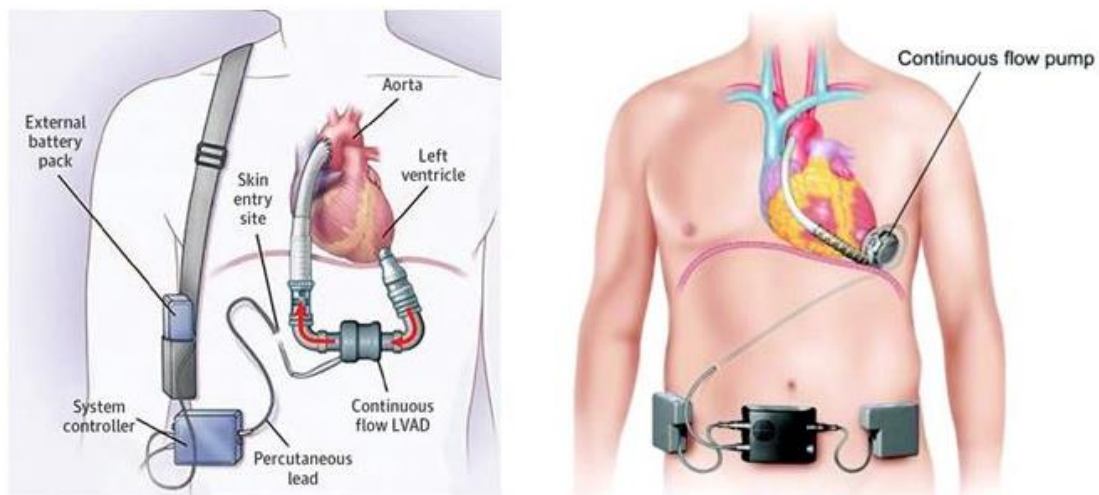

Figure 1.4: LVAD components. Left: pump placed within the peritoneal cavity. Right: pump placed "on board" of the heart.

Oxygenated blood is drained from the LV, through the inflow cannula, into the pump body, then actively pumped through an outflow cannula to the downstream ascending aorta.

There are two main categories of mechanical blood pumps: volume-displacement and rotary pumps.

Volume-displacement pumps (Figure 1.5a) consist of a chamber or a sac that fills passively or by suction and is compressed by an external pusher plate. Their performance is excellent in unloading the left ventricle and sustaining the circulation with a capacity to pump up to 10 L/min. Whilst displacement pumps maintain the physiological pulsatility of the flow, they typically experience problems related to long-term mechanical failure of diaphragms and valves.
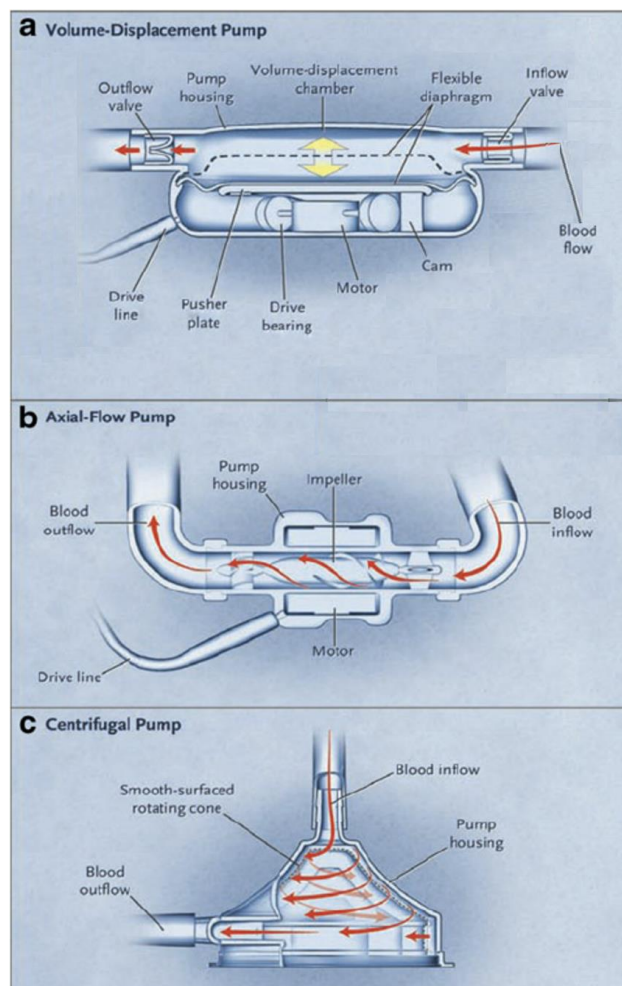

Figure 1.5: Pump types. (a) The volume-displacement pump consists of a chamber or sac that fills and empties cyclically. (b) The axial-flow pump contains an impeller, a rotor with helical blades that curve around a central shaft. (c) The centrifugal pump consists of a conical rotor contained within a housing. Blood flows into the apex of the cone and exits at the base.

Over the years, these systems have been replaced by rotary miniaturized continuous-flow pumps.

The impact of removing the pulsatility of the blood flow on the circulation and organ function is debatable, but the advantages of continuous flow pumps are the simpler design, the smaller size, the lower power consumption, and the higher durability and efficacy in the long-term.

Rotary blood pumps are suitable for high flows up to 20 L/min, they consist of an inlet and outlet with a single rotating element (impeller) that transfers energy to the blood in order to increase arterial blood flow and pressure. These devices can be axial and radial (centrifugal) according to the geometry of the impeller.

Axial flow pumps (Figure 1.5b) are driven by a spinning rotor around a central shaft. The outlet is collinear with the rotating section and the blood is moved both rotationally and axially. Centrifugal flow pumps (Figure 1.5c) are driven by a hydrodynamic or electromagnetic suspended spinning rotor; they convert the rotational flow to linear flow by positioning the outlet tangentially with the pump housing [20-21].

Improvements in technology and patients outcomes, including development of smaller LVADs suitable for use in a larger number of patients, have led to progressive growth in the number of LVAD implants.

As shown by the seventh annual report of the Interagency Registry for Mechanically Assisted Circulatory Support (INTERMACS), the number of VAD implants is approaching 2500 per year, with the INTERMACS database including more than 15000 patients. As reported in Figure 1.6, the survival curve for devices implanted since 2008 shows an overall 80% of 1- year survival and 70% of 2-year survival [22].
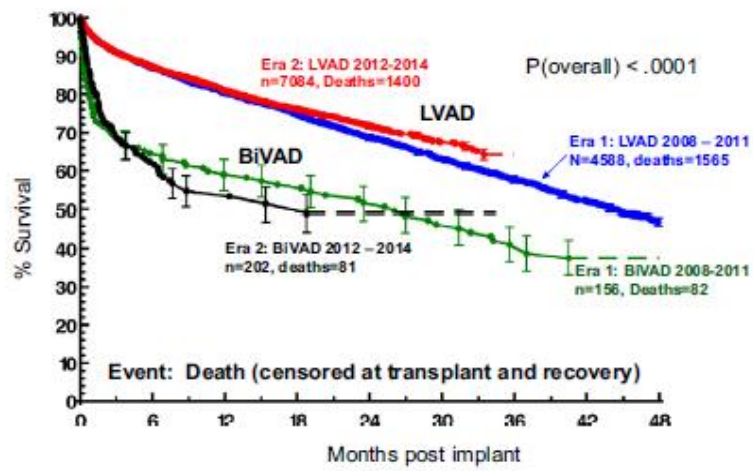
Figure 1.6: Actuarial survival curve for continuous-flow LVADs and BiVADs, stratified by era. The error bars indicate ±1 SE.

1.2.2. Device-related Complications

LVAD technology has progressed significantly over the past two decades. As earlier mentioned, designs have evolved from pulsatile devices to small implantable devices that deliver continuous flow. Despite these advancements, there are a number of clinical complications associated with LVAD therapy.

The most common postoperative complication following LVAD implantation is bleeding, that is associated to high mortality when the central nervous system is involved and can lead to ischemic stroke. Moreover, the onset of these complications requires re-hospitalization, rising healthcare costs.

LVAD recipients are also exposed to an elevated risk of developing Von Willebrand's disease, in which large multimers of Von Willebrand factor (a blood glycoprotein) are destroyed by mechanical stress, increasing bleeding risk [23]. Further, in order to limit propensity to blood clotting, patients are managed with antithrombotic therapy, including a combination of antiplatelet and anticoagulant drugs, which, in turn, pose a significant bleeding risk.

A major concern about LVADs is also device-related thrombogenicity, which is attributable to several mechanisms such as non-physiologic blood flow patterns leading to red blood cell damage or haemolysis, endothelial dysfunction and chronic platelet activation.

Starling *et al*. [24] observed an increase in the rate of device thrombosis associated with substantial morbidity and mortality among patients who received the *HeartMate II* LVAD (Thoratec Corp., Pleasanton, CA, USA). It was reported that confirmed pump thrombosis occurred early and peaked 1 month after implantation, with a reduction in risk by 6 months (Figure 1.7). The exact cause of the increased rate of pump thrombosis remained unknown, although the authors suggested that the *HeartMate II* might have a more narrow tolerance with respect to thrombus formation than originally understood, and might be vulnerable to the timing and intensity of anticoagulation.
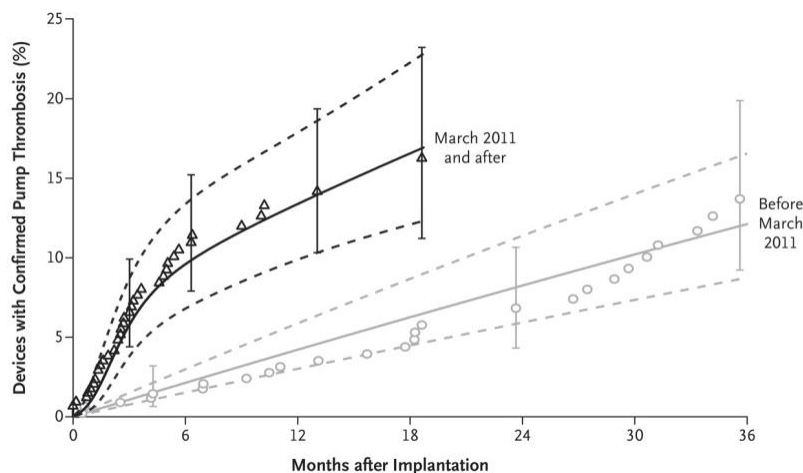
Figure 1.7: Occurrence and incidence confirmed pump thrombosis stratified according to implantation date.

The ENDURANCE [25] and MOMENTUM 3 [26] clinical trials compared the performances of the *HeartWare* VAD (HVAD HeartWare Inc., Miami, FL, USA), which is a small intrapericardial centrifugal-flow device, the *HeartMate II* (Thoratec Corp., Pleasanton, CA, USA), an axial-flow mechanical-bearing pump, and the *HeartMate3^{TM}* (Abbott, Chicago, Illinois, USA), a bearingless magnetically levitated centrifugal continuous-flow pump.

The *HVAD* was found to be noninferior to the axial flow device with respect to survival free from disabling stroke or need for device replacement. The rate of device replacement, explantation, or need for urgent transplantation due to device malfunction was higher for the *HeartMate II* if compared to the *HVAD* (16.2% vs. 8.8% respectively), as it was for the risk for LVAD thrombosis.

The *HeartMate3^{TM}* was reported to significantly reduce the incidence of pump thrombosis. It was associated with a higher rate of survival and a more evident improvement in clinical outcomes, with respect to the *HeartMate II*, but it was not free from thromboembolic complications and strokes.

In the ADVANCE [27] clinical trial, the authors evaluated the incidence of pump thrombus formation in patients who received the HVAD, identifying, at the same time, the major predictors for thrombogenesis. Signs of pump thrombus included unexpected power increases, flow estimation beyond that predicted from power consumption, elevated levels

of lactate dehydrogenase (LDH), a biochemical marker of haemolysis, and plasma free haemoglobin (pfHgb).

Thrombus formation was demonstrated [24, 27] to often develop at the interface between the ventricular endocardial surface and the LVAD inflow cannula, with subsequent thrombotic apposition on the cannula and, eventually, migration and ingestion of intraventricular thrombi into the pump. Ingested thrombi may either enhance pump thrombosis or, when propelled downstream, provoke thromboembolic events.

Several mechanisms have been suggested to trigger and promote intraventricular thrombus formation:

- blood contact with an artificial surface at the LV apex - LVAD inflow cannula interface;
- platelets that, activated/sensitized by the supra-physiologic hypershear environment within the pump, once returned to the LV, tend to aggregate, generating thrombi, because of the prothrombotic hemodynamic conditions within the LV;
- the altered ventricular hemodynamics (stagnation regions and recirculation patterns) due to:

    i. enlargement of the LV chamber and reduced myocardial contractility;

    ii. LVAD implantation, in particular the LVAD inflow cannula/ouflow graft surgical implantation configuration.

Surface Contact Activation

Even though titanium is the most biocompatible metal to be used in blood recirculating devices, still it is not completely inert, thus possessing the potential for triggering coagulation and thrombus formation. Contributors to titanium's bioreactivity are proteins mediating platelet adhesion, like fibrinogen, and prothrombotic contact proteins. These

proteins set off a chain reaction that leads to abundant fibrin formation and contributes to increase clot growth rate. Sintering is used to mitigate titanium thrombogenicity. As Najjar *et al.* [27] confirmed in their study, comparing sintered *vs.* non-sintered surfaces, the technique appeared to have succeeded in limiting the growth of tissue along the shaft of the cannula. This way, the connective tissue does not extend beyond the sintered area and is more firmly adherent to it (Figure 1.8d). Sintering is a process by which small titanium beads are mechanically affixed to the titanium surface of the cannula, creating a matrix into which tissue can be incorporated.
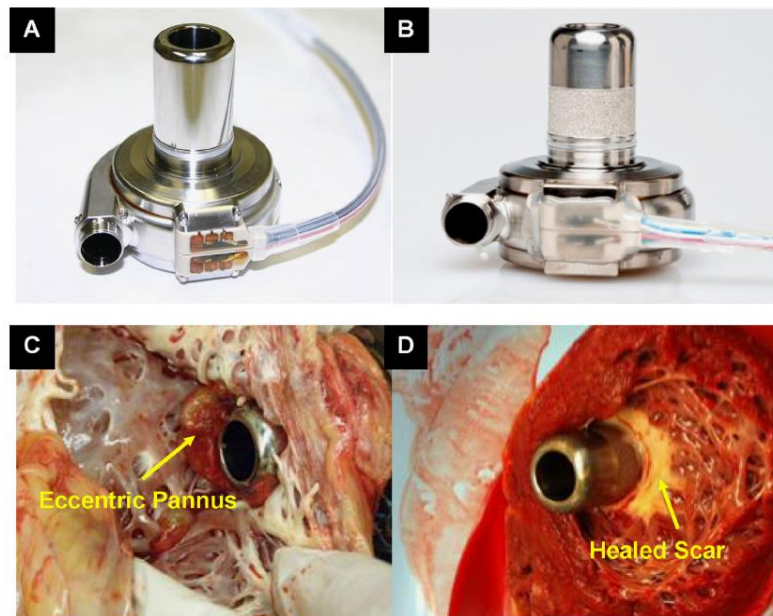

Figure 1.8: (A) Non-sintered *vs.* (B) sintered HVAD (HeartWare Inc., Miami, FL, USA) pumps. (C) Tissue growth on the inflow cannula of a non-sintered pump extends across the length of the cannula, (D) whereas tissue growth on the inflow cannula of a sintered pump does not extend beyond the sintered area.

Hypershear Environment

A dominant mechanism contributing to thrombosis in mechanical circulatory support (MCS) systems is the supra-physiologic hypershear environment, that is, highly dynamic elevated shear stress, imparted to blood through the impeller of current LVADs. Present

pumping systems, because of extremely narrow gap clearances between the impeller and the pump housing, induce elevated shear stress on platelets and red blood cells as they move throughout the LVAD, resulting in cumulative platelet damage and consequent activation, haemolysis, initiation, and subsequent propagation of thrombus formation [28].

Furthermore, high values of dynamic shear stress sensitize platelets to subsequent low shear conditions, experienced by platelets in areas of stagnation, for instance in the apical region of a failing LV, or in normal cardiovascular circulation conditions. Actually, while platelets are activated by short periods of high shear, they do not recover their normal quiescent activity state under consecutive normal conditions of low shear. Rather, if the initial exposure is sufficiently severe (≥ 2000 dynes·s/cm^2 or 200 Pa·s), they are rendered substantially more sensitive to activation in response to low shear stress [29], increasing the thrombotic risk associated with blood-recirculating devices. Moreover, with recirculation, the risk for chronic platelet activation increases substantially over time. As a result, activated platelets due to recirculation through the pump might experience altered hemodynamic conditions within the pathologic-implanted LV, triggering the formation of intraventricular thrombi.

Altered LV Hemodynamics

Blood stasis and recirculation patterns in the LV chamber are recognized risk factors for intraventricular thrombosis and potential thromboembolic events.

In physiologic blood flow, thrombus formation is prevented by appropriate levels of wall shear stress that create a homeostatic balance between fibrin monomer polymerization and cleavage. However, in areas of stagnation, this homeostatic balance is disrupted, increasing the susceptibility to pathologic thrombus formation [30].

Moreover, regions of stagnation and recirculation promote thrombosis through the accumulation of both active and sensitized platelets. Sensitized platelets may get trapped because of the limited washout and may be exposed to low dynamic shear stress for

elongated durations and eventually become activated, enhancing the potential for thrombosis [29, 31].

Aberrant flow patterns are observed in patients with DCM: the normal LV flow pattern has been reported to recycle the blood volume inside the LV every 2–3 beats, but, blood transport is significantly altered in patients with reduced contractility by large swirling flow patterns, where blood is trapped and undergoes rotation throughout most of the cardiac cycle [32] (Figure 1.9). In particular, stagnant flow is present in the lower apical region, where it triggers the activation of the coagulation system.

LV dilation and reduced myocardial contraction cause the flow to be disorderly, reducing the blood flow for systolic ejection and, consequently, increasing the residual blood flow in the LV cavity [33-34].
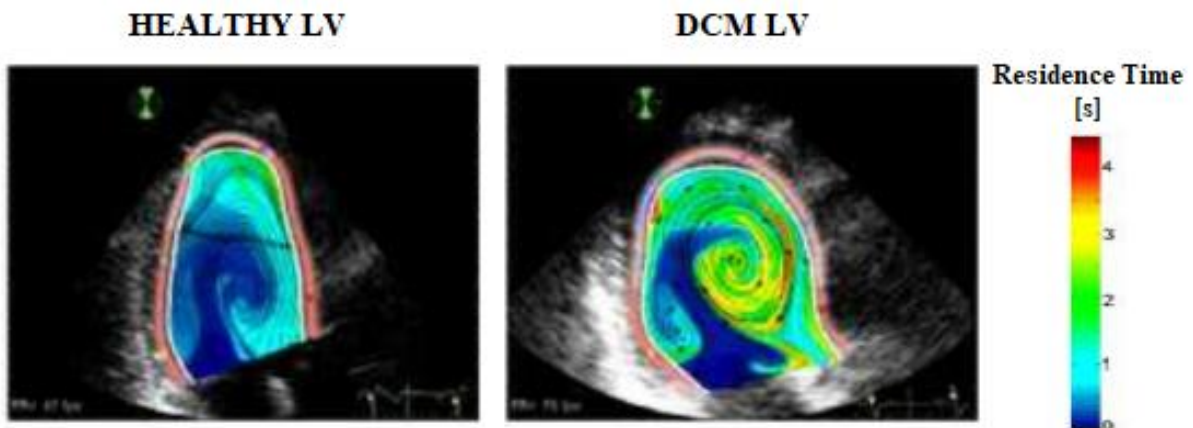

Figure 1.9: Intraventricular Residence time at the diastolic E-peak, in a healthy LV (left) and in a LV with dilated cardiomyopathy (right). The residence time is the time spent by a blood particle inside the LV.

Even though LVAD implantation is meant to restore, in a dilated ventricle, the flow field of a normal heart, nonetheless, the device was proven to alter intraventricular blood flow and rheologic conditions, creating areas of stagnation and recirculation zones in the LV apex.
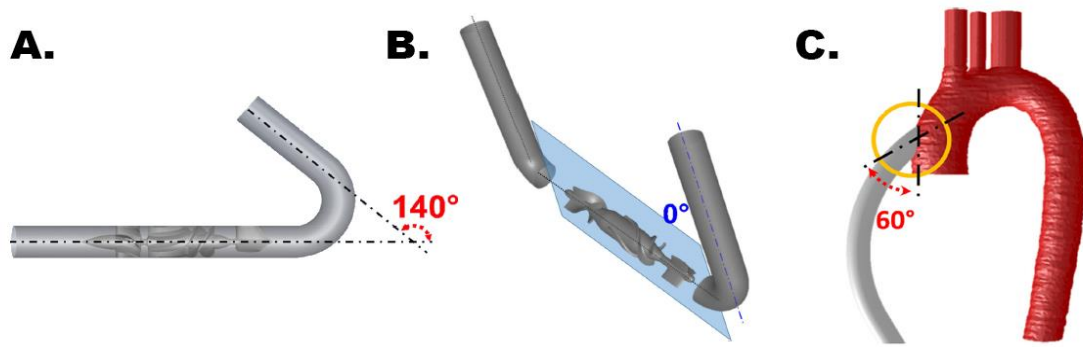
Figure 1.10: Implantation configurations studied: (A) Inflow cannula elbow angle (140°); (B) Inflow cannula circumferential orientation (0°), the angles being calculated between the inflow cannula and the sagittal plane (light blue); (C) 60° anastomotic angle of outflow graft end-to-side anastomosis with respect to the ascending aorta.

For reducing the overall thrombogenic potential (TP) of LVADs, it is of paramount importance to optimize both the device design and the implantation configuration. On the subject, Chiu *et al*. [35] evaluated how system element variables such as inflow cannula elbow angle, LVAD rotational orientation, and LVAD outflow graft orientation may adversely affect the overall thrombogenicity of the *HeartMate II* (Thoratec Corp., Pleasanton, CA, USA). The lowest TP was generated combining an inflow cannula elbow angle of 140° with a 0° circumferential orientation of the LVAD with respect to the sagittal plane, and a 60° anastomotic angle, to connect the outflow graft to the ascending aorta (Figure 1.10).

These results confirmed the hypothesis previously made by Taghavi *et al.* [36], who identified an inflow cannula elbow angle greater than 55° to minimize the risk for thrombosis. On the other hand, Chivukula *et al*. [37] deeply investigated the impact of surgical angulation of the VAD inflow cannula on intraventricular thrombogenicity. The TP of 5 LVAD inflow cannula angulations (0°, ±7° and ±14°) was evaluated based on platelet shear stress history. Angulation of the inflow cannula >7° from the apical axis led to markedly unfavourable hemodynamics (Figure 1.11).

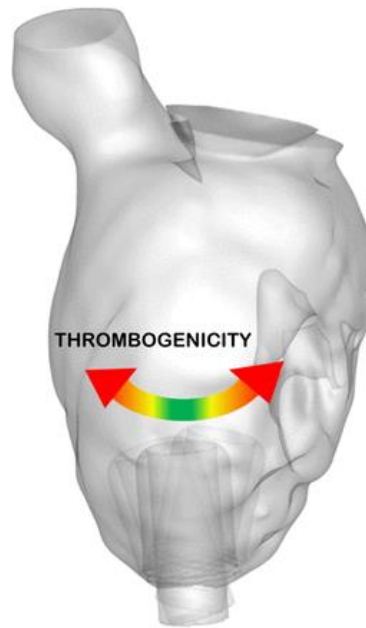Figure 1.11: Range of thrombogenicity of inflow cannula angulation, indicating optimal angle in green.

In order to optimize how the LVAD unloads the left ventricle and reduce thrombosis preferably to a level that does not require anticoagulation therapy, a detailed understanding of the impact of the device on the LV hemodynamic variables, such as stagnation areas, recirculation patterns, and shear stress, is crucial.

1.3. Aim of the Thesis

As previously mentioned, LVADs are responsible for a number of postoperative complications, the most relevant being device-related thrombosis. In the last decade, several studies [25-28, 35-37] were able to identify a wide range of mechanisms enhancing and promoting thrombogenesis, such as: shear stress mediated platelet prothrombotic activity, LVAD inflow cannula/outflow graft surgical implantation configurations, development of infections, haemolysis, intraventricular aberrant flow patterns and surface contact activation.

We hypothesize that the residual contractility of a dilated ventricle can act as an additional thrombogenic factor, since the degree of cardiac impairment associated with HF seems to have a role in altering LV hemodynamics. Altered intraventricular hemodynamics might promote prothrombotic conditions, especially in the LV apical region, where the LVAD inflow cannula is inserted.

Hence, it is suggested that the thrombus-favourable LV flow dynamics is able to trigger platelet activation, while LVAD inflow cannula acts as a substratum for thrombus formation, apposition, and progressive growth.

Therefore, given that both the myocardial residual contractility and the LVAD have a role in determining LV hemodynamic variables (areas of stagnation, recirculation patterns, wall shear stress), here we analyzed the mutual interactions between these two factors.

Investigation of this hypothesis was carried out by setting up a computational fluid dynamics (CFD) model, that systematically analyses the contribution of LV residual contractility and LVAD inflow cannula implantation configurations on the LV thrombogenic potential.

Therefore, the present work is focused on the development of a CFD model aimed to analyse the LV hemodynamics of a LVAD-supported heart. The model is patient-specific. Blood flow characteristics, such as shear stresses, stagnation zones and recirculation patterns were assessed, *pre-* as well as *post*-implantation of the LVAD.

The model allows to describe, at a first stage, LVAD thrombogenic potential variations depending on the degree of myocardial residual contractility, and, in a second phase, as a function of different inflow cannula positions.

On varying the residual contractility, a *pre*-implant LV model (i.e., without the LVAD) is used as a basis for comparison with the *post*-implant configurations.

2. State of the Art

In the present chapter, most relevant numerical studies that have previously evaluated the fluid dynamic conditions of a pathologically dilated LV are described, together with several studies that, in the last decade, investigated the thrombogenic potential of the LVAD-assisted heart. In addition, a comprehensive description of the major techniques through which ventricular wall motion can be reproduced in a CFD model is included, as a means of modelling realistic LV hemodynamics. Furthermore, we present the analysis of studies describing *in vitro* characterization of the intraventricular flow patterns in the LVAD-assisted heart.

The combined use of numerical simulations and clinical imaging for research and diagnosis can provide additional information and is a valuable tool to investigate the relationship between cardiac pathology and the associated abnormal flow pattern [38].

Global and regional hemodynamic variables, such as ventricular wall motion, spatial and temporal distribution of blood pressure, and myocardial stress and strains, can be obtained through CFD simulations [39].

Patient-specific LV CFD simulations aim at mimicking realistic cardiovascular hemodynamics to evaluate the intraventricular blood flow patterns for different purposes, such as diagnostic analysis, evaluation of surgical outcomes, and preoperative analysis to examine different possible treatment options. There are two main approaches for the numerical simulation of LV using CFD techniques: the geometry-prescribed method, in which the movement of the LV myocardial wall is imposed as a boundary condition for the fluid domain; the fluid-structure interaction (FSI) method, that numerically solves the governing equations of both the fluid and structure domains [40].

For what concerns the first approach, the LV myocardium motion is prescribed either directly by extracting wall motion data from imaging data, or indirectly by setting up

mathematical equations to formulate wall motion. The FSI method, instead, couples both the CFD and the structural solver. When a fluid interacts with a deformable or moving structure, stress and strains are exerted on the solid object. If these deformations are large, the fluid velocity and pressure fields will change as a result. In other words, the fluid flow affects the structural deformations, and the structural deformations affect the fluid flow.

To achieve a detailed and reliable hemodynamic analysis whose results are not overly approximated, a left ventricular CFD model should have the following properties:
- reproduce the patient-specific geometry of the LV;
- the imposed LV wall motion should replicate the cardiac one, thus accounting for myocardial fibres torsion, as well as for LV wall contraction/dilation over the different phases of the cardiac cycle.

These specifications are required since vortex dynamics, stagnation areas and recirculation patterns are strongly dependent on the LV morphology and cardiac wall motion.

2.1. Hemodynamics of a Pathologically-Dilated LV: Numerical Characterization

Intraventricular flow features differ depending on the cardiac condition, so the investigation of different clinical cases through CFD analysis can provide insights on how pathologies alter flow fields. The occurrence of cardiac disease may produce flow patterns deviating from what is considered normal and optimal, reducing the cardiac function.

In this section, three numerical studies characterising the hemodynamics of a pathologically-dilated LV are described: two are based on a paradigmatic LV geometry, while the third one is patient-specific. For all of them, LV wall motion was implemented through the prescribed-geometry approach. Torsion is completely neglected, only contraction/dilation of the LV is modelled.

2.1.1. Paradigmatic Geometries

Loerakker *et al.* [41] developed a numerical model to investigate the influence of dilated cardiomyopathy on vortex dynamics and flow patterns in the LV; the study is based on an axisymmetric fluid dynamic model of a LV, coupled with a lumped parameter model (LPM) of the systemic circulation. The LV was modelled as a truncated prolate ellipsoid with a long axis of 8 cm and a short axis of 5 cm. The upper end was connected to a 1 cm long tube, through which the fluid entered the ventricle during diastole, and left it during systole (Figure 2.1).

Simulations were performed for a healthy ventricle, an end-stage DCM ventricle and a VAD-assisted DCM ventricle. The LVAD flow was varied between 1 and 6 L/min, with 1

L/min increments. Strength, area and mean vorticity of the intraventricular vortices were derived from the computed flow patterns.
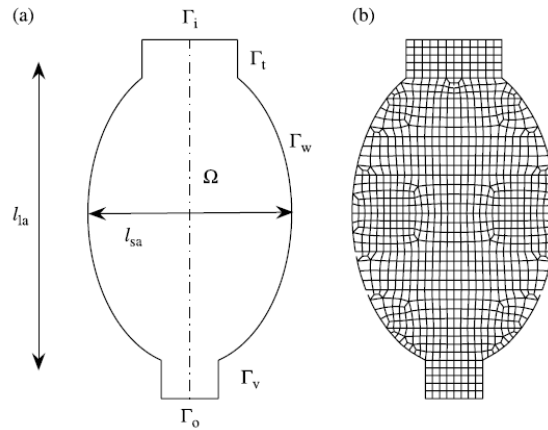

Figure 2.1: Model of the left ventricular cavity. (a) l_{la} and l_{sa} denote the long and short axis of the truncated prolate ellipsoid, respectively, Γ is a boundary of the mesh on which boundary conditions are specified and Ω is the fluid domain. (b) Elements used in the mesh.

The relation between LV pressure and volume was modelled with a one-fibre model, where it was assumed that stress and strains were uniformly distributed within the ventricular wall. The volume change calculated with this model was used to move the ventricular wall in CFD simulations. Deformation of the fluid elements of the mesh was obtained by solving a linear elastic problem, where the deformation of the LV wall was used as a Dirichlet boundary condition to compute nodal displacement.

Results showed that the single vortex ring that was developed in the DCM ventricle (Figure 2.2, bottom panel) had less strength than the leading one in the healthy ventricle model (Figure 2.2, top panel). Furthermore, vortex core area was found to be smaller in the DCM ventricle than in the healthy situation, in contrast with other studies in literature [42], probably because the weakness and the impairment of the simulated DCM LV was so severe (residual ejection fraction equal to 16% and end-diastolic volume of 228 ml) to prevent the incoming fluid jet from inducing a large vortex ring.
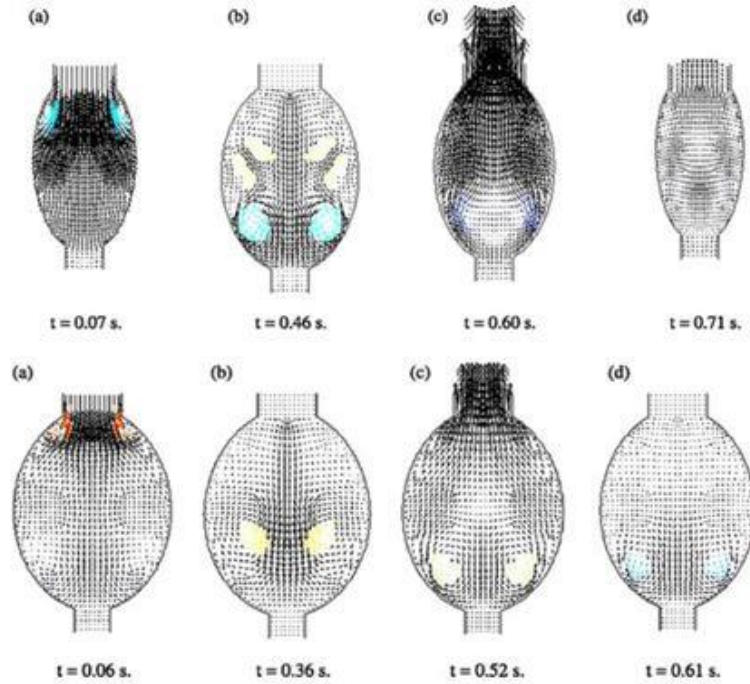
Figure 2.2: Top panel: Flow fields in a healthy ventricle at (a) maximum filling rate; (b) end of filling phase; (c) maximum ejection rate and (d) end of ejection phase. The leading vortex ring is coloured in light blue.

Bottom panel: Flow fields in a DCM ventricle at (a) maximum filling rate; (b) end of filling phase; (c) maximum ejection rate and (d) end of ejection phase.

The upper tube served as atrium/aorta, depending on the phase of the cardiac cycle, while the lower tube represented the inflow cannula of an LVAD, considered in other simulations not reported here. In the described simulations, the lower tube was set as wall.

Even though this study can be considered as the first computational model quantitatively analyzing vortices in a LV, it is affected by some limitations. First of all, the model geometry is paradigmatic and ignores detailed internal structure, simplifying ventricular shape on one hand, but increasing the probability of obtaining non-realistic results.

Moreover, the LV deformation is computed by means of weighting functions, a predefined ratio between LV long and short axis and a prescribed volume change (LPM-derived), so that the behaviour of the LV wall could not be related to physiological wall deformations. Despite so, the model still detects intraventricular vortices very well, enabling quantitative analysis of vortex structures.

Chan *et al.* [43] investigated the effect of ventricular size and geometrical modifications in a DCM LV on the LV haemodynamics, using the geometry-prescribed approach. The LV was modelled as an axisymmetrical half truncated prolate spheroid, whose values of height and radius were set as to simulate two degrees of DCM, that is moderate and severe dilation. In addition, a normal LV was considered, to serve as a baseline for comparison.

The LV wall motion was derived from the instantaneous blood flow rate Q(t) through the mitral valve (Figure 2.3), based on a simple elastic membrane model, used to describe the LV deformations. According to this model, the rates of change of the LV radius R and height H were (eq. 1):

$$
\begin{cases}
\dfrac{dR}{dt} = \dfrac{3Q(t)}{\pi} \dfrac{2H^2 - R^2}{10H^3R - 4HR^3} \\[4mm]
\dfrac{dH}{dt} = \dfrac{3Q(t)}{\pi} \dfrac{H^3}{2H^2R} \dfrac{2H^2 - R^2}{10H^3R - 4HR^3}
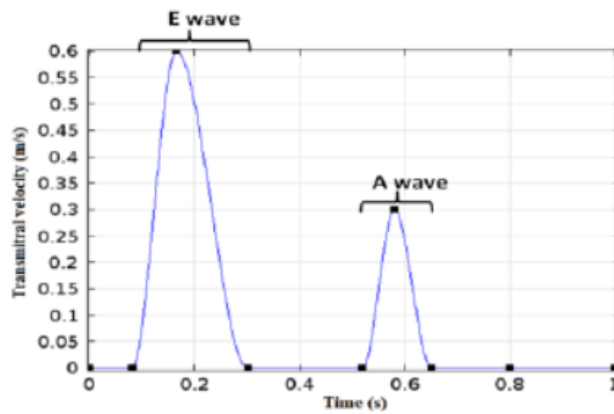\end{cases} \tag{1}
$$

Figure 2.3: Inlet flow velocity profile.

Results showed that vortex strength and pressure gradients were significantly reduced in a dilated heart (Figure 2.4), leading to an increased risk of thrombus formation and impaired ventricular filling. The process of vortex ring formation occurred during the filling phase

26

and was thought to play an important role in determining the pumping efficiency during systole. In detail, the normal ventricle was characterized by the greatest vortex strength as compared to the moderately and severely dilated ventricles. Hence, due to the weaker vorticity magnitude, the vortex ring was propelled towards the apex by weaker convective acceleration and thus had less energy. As a consequence, vortex washout was reduced, leading to blood stagnation in the apical region.

Despite providing detailed information as for the altered haemodynamics at the LV apex, given the paradigmatic LV geometry, the model was not able to capture the asymmetric vortex profile occurring in the cardiac cycle.
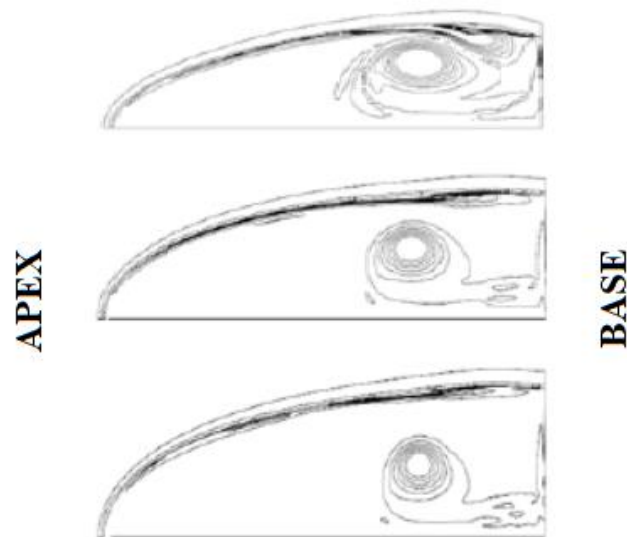

Figure 2.4: Vorticity in the ventricle with end-diastolic volume: (top) 130 ml; (middle) 268 ml; and (bottom) 400 ml at t = 0.36 s in the geometry-prescribed implementation.

2.1.2. Patient-specific Geometry

In a 2016 study, Bavo *et al.* [38, 44] created a patient-specific CFD model of the LV, with prescribed moving boundaries, to evaluate the abnormal flow patterns in impaired hearts. Comparative analysis of the hemodynamics in three patients with various degrees of impaired diastolic function allowed to detect the diversity of the flow field as a function of the morphology of the LV, of the shape of the mitral valve, and of the heart residual contractility, identifying distinct flow features, such as pattern of vortex formation and evolution.

The model was based on segmented real-time transesophageal echocardiographic images (rt-TEE), from which the patient-specific geometry, the position of the LV and fully three-dimensional mitral valve (MV) were derived. To obtain image-derived models of the LV, a semi-automated image segmentation of the LV was performed at one frame in systole, and the registered deformation was used to propagate that segmentation to all the other frames in the image series.

The result of the segmentation process was a set of triangulated input surfaces with a frame rate of 18 frames/cycle (Figure 2.5a), but to replicate the motion of the walls, a time interpolation was performed through Natural Cubic Splines.
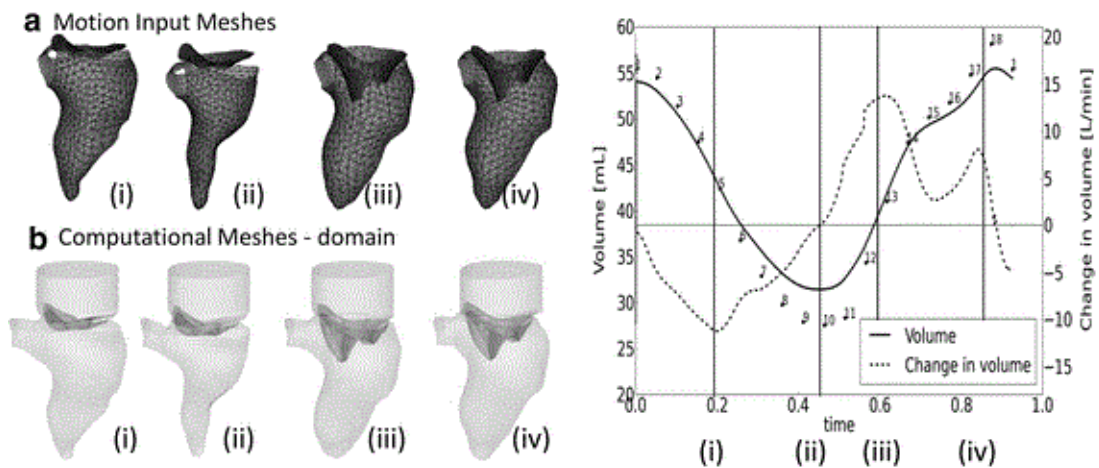

Figure 2.5: Prescribed motion of the boundaries. Comparison between (a) the motion input meshes and (b) the computed meshes, complete domain in four time-points of the cardiac cycle.

28

Each boundary point x_i of the computational mesh was associated with the three closest points $(x^i_{0ref}, x^i_{1ref}, x^i_{2ref})$ on the input surface (Figure 2.6). Then, every single computational point was projected (x^i_{proj}) on a triangle T^i, generated by the three aforementioned points, and its barycentric coordinates (α, β, γ) with respect to the triangle, were identified.

Finally, the grid point displacement was determined as a linear combination of the displacements of the three points, weighted with the barycentre coordinates.

As a consequence of the wall motion, all the fluid grid needed to be modified throughout the computation. LV motion was mathematically described and implemented in the model with user-defined functions (UDF), compiled and loaded in the commercial software ANSYS Fluent.

The aortic valve and the inner topology of the LV (trabeculae and papillary muscles) were not included in the model and the torsion of the ventricle during systole was not analyzed. As a matter of fact, due to the interpolation process from the input mesh to the computational mesh (Figure 2.5b), the in-plane motion was not represented accurately. Consequently, no torsional effects of the ventricle were recreated.
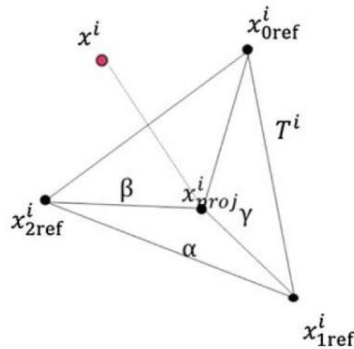

Figure 2.6: Grid node displacement computation.

Results showed that in early diastole, the vortex structure originated in the proximity of the valvular edges; in particular, when the most severe degree of DCM was considered (P3), this vortex was broader than for the other subjects. Velocity streamlines were also reported: due to the different dimensions of the three LVs, the peak velocities differed (Figure 2.7).

As this work was focused on the analysis of the diastolic phase, the absence of the systole may introduce approximations in the calculated flow field, especially in the case of a regurgitant mitral valve, in which a systolic transmitral backflow would influence the vortex formation and the ventricular hemodynamics.
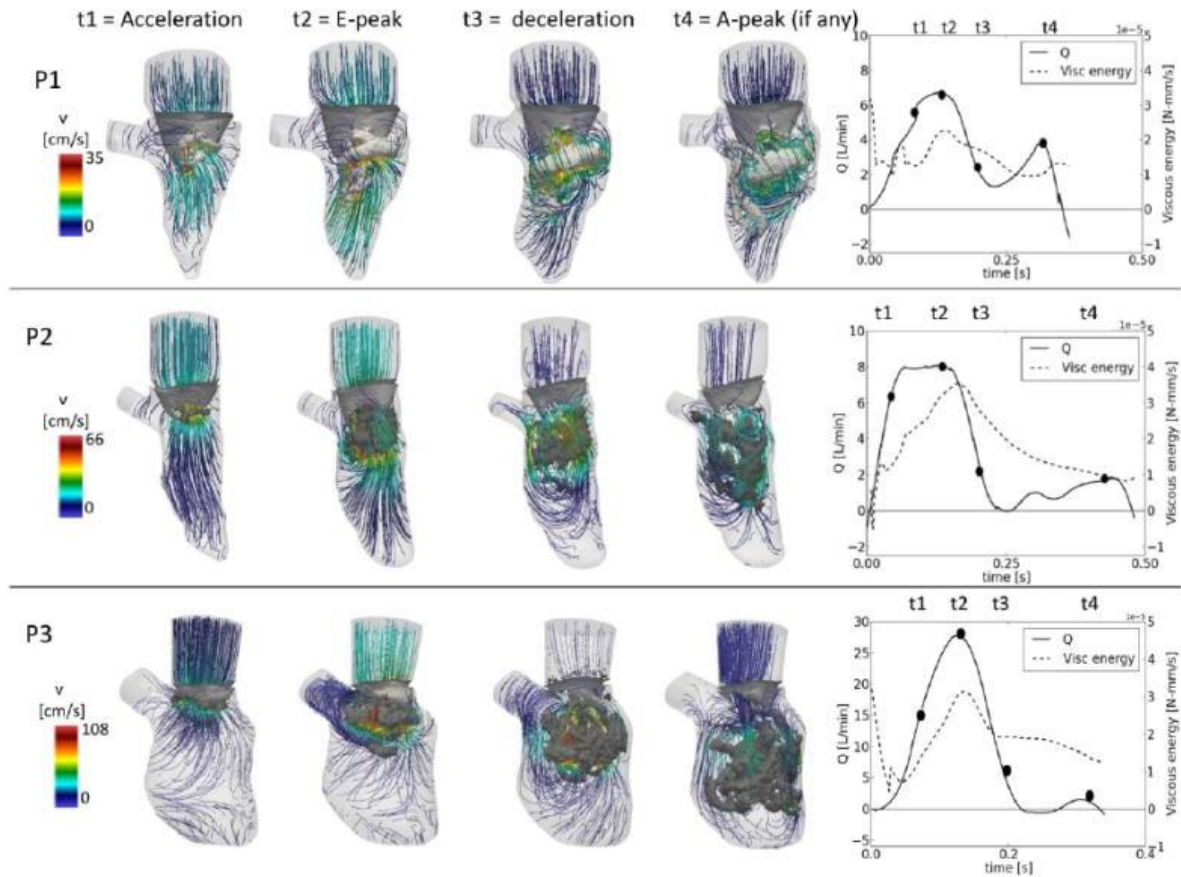
Figure 2.7: Intraventricular vortex visualisation and velocity streamlines at four relevant time-points. Right panels: flow curve and viscous energy dissipation curve.

P1 had a moderate concentric hypertrophy, with a preserved ejection fraction (52%). P2 showed a reduced ejection fraction (36%) and a ventricle with an elongated shape. P3 had a severe ventricular dilation (residual ejection fraction 22%), with dimensions substantially larger than the other subjects.

2.2. Numerical Characterization of the LVAD-assisted Heart Hemodynamics

Several studies in literature investigated the disturbed hemodynamics and the thrombogenic potential of the LV in presence of LVAD through CFD approach, which provides detailed characterization of the ventricular flow, such as velocity profiles, shear stress distributions, and re-circulation patterns. The most crucial element that can alter the physiological hemodynamics of the LV is the inflow cannula, whose geometry, insertion depth, insertion angle and position may modify the intraventricular flow fields.

In this section, five numerical studies analyzing the fluid dynamics of a LVAD-assisted LV are reported. These studies are classified according to the type of model geometry (i.e. patient specific *vs.* paradigmatic) and further subdivided based on the presence of LV wall motion.

2.2.1. Paradigmatic Geometries

Static LV Wall

Different inflow cannulae tip structures were proven to cause various degrees of thrombosis and suction leading to obstruction that may further influence the LVAD's performance.

Liu *et al.* [45] analyzed the blood flow patterns in four different LVAD inflow cannulae (blunt, bevelled, trumpet-tipped and caged), in order to compare their performances in terms of blood compatibility and suction generated in the LV, once being inserted in the LV apex.

The geometry of the LV was simplified, neglecting its real morphological and structural features, cannula insertion depth, and angle. The four cannulae were assumed to be straight pipes, with an inner diameter of 12 mm.
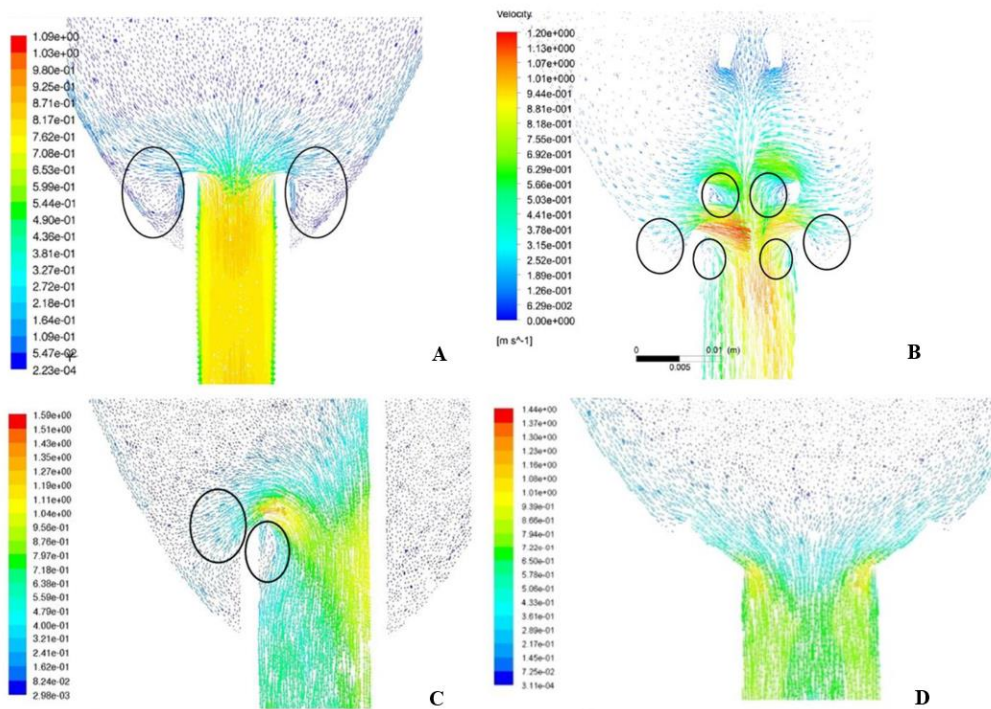
Figure 2.8: Velocity vector distribution near the cannula tip: (A) blunt; (B) caged; (C) bevelled; (D) trumpet. The black circles identify vortex regions.

The results showed that the cannula tip structure affected LVAD performance; furthermore they identified the trumpet tip as the most suitable for long-term LVAD implantation, due to the uniform velocity field generated, lack of vortices and flow stasis at the cannula insertion point (Figure 2.8D).

In this study the ventricular geometry was simplified and cannula insertion angle and insertion depth were neglected, but these factors may change the flow distribution in the LV. Furthermore, the LV wall was considered to be a fixed and rigid boundary.

LV Wall Motion

An alternative method to the prescribed wall motion was used by Ong *et al.* [46-47] to investigate the correlation between LVAD cannula placement and potential for thrombus formation, using a two-way fluid structure interaction (FSI) model.

In that study, the LV wall was considered as a passive structure, and modelled as a Mooney-Rivlin hyperelastic material, with strain energy density function W_s as:

$$W_s = C_{10}(I_1 - 3) + C_{01}(I_2 - 3) + \frac{1}{2} k(J_{el} - 1)^2$$

where I_1 and I_2 are the first and the second invariants of the left isochoric Cauchy-Green deformation tensor, J_{el} is the elastic Jacobian, $C_{i,j}$ are the material parameters, and k is the bulk modulus.

The cannula wall was modelled as a linear elastic silicone material, with a density of 1100 kg·m^3, Young's modulus of 3.6 MPa, and Poisson ratio of 0.49. As set up for the study, three different cannula insertion lengths were considered (Figure 2.9).

The simulations where performed using the commercial software COMSOL, which employs the arbitrary Lagrangian-Eulerian (ALE) method. Through the incompressible Navier-Stokes equation and the mass continuity equation, the fluid flow was described.
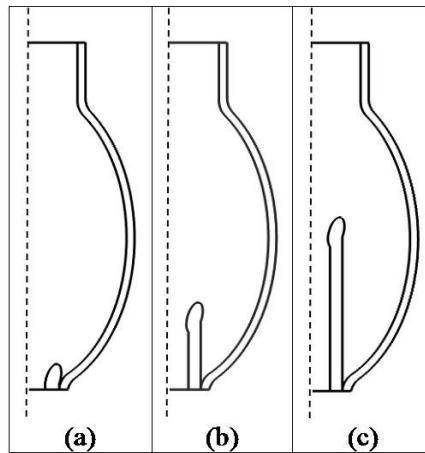

Figure 2.9: Three different configurations of cannula placement are used in the simulations: (a) near the apex; (b) one fourth of LV and (c) half LV.

The calculated LV stress was used to compute the LV displacement at every point in the wall. The resultant LV displacement was, in turn, employed to calculate the fluid velocity, given that, at the fluid-LV interface, wall and fluid velocities were assumed to be equal.

It was reported that the one-fourth placement of the cannula into the LV achieved the best performance in terms of reducing the risk of thrombus formation, because of a negligible amount of stagnation flow near the apical wall, higher vortex intensity, but lower values of wall shear stress when compared to the other configurations (Figures 2.10).

The idealized geometry coupled with smooth surface and isotropic material properties limited this study. Actually, the LV is a complex geometry with non-smooth endocardial surface and anisotropic material properties, which may result in localized stress distributions. Furthermore, the LV was considered as a passive structure, its deformation due to the velocity profile imposed at the mitral valve rather than to a movement prescribed to the mesh nodes, depending on the LV residual contractility.
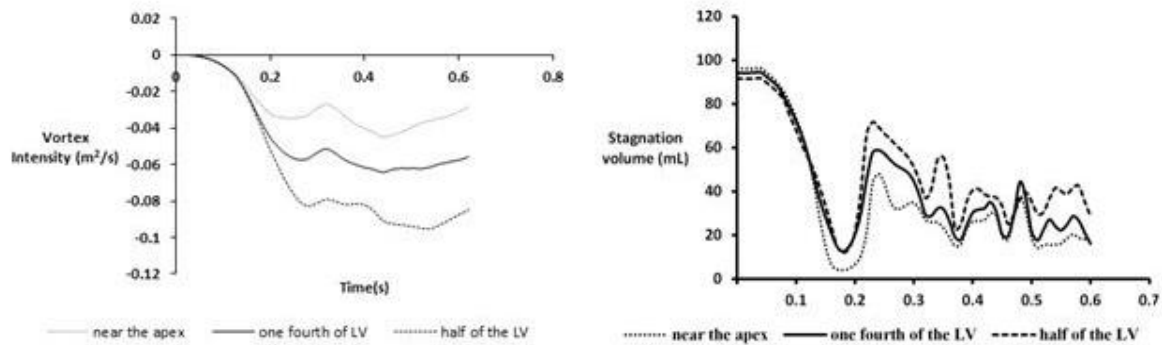

Figure 2.10: Left panel: Time course of the average vortex intensity in the model, under different cannula placements. Right panel: Time course of total stagnation volume, under different cannula placements.

2.2.2. Patient-specific Geometries

Static LV Wall

In 2016, Liao *et al.* [48] determined the effects of various inflow cannula geometries on intraventricular flow, under full LV support in a patient-specific model. However, the model neglected LV wall motion.

CT imaging data were used to extract the LV volume from a candidate to LVAD implantation. Five different cannulae geometries (crown tipped (A), thin walled tubular (B), large filleted (C), trumpet like (D) and inferiorly flared (E), as reported in Figure 2.11) were modelled based on clinically available designs.
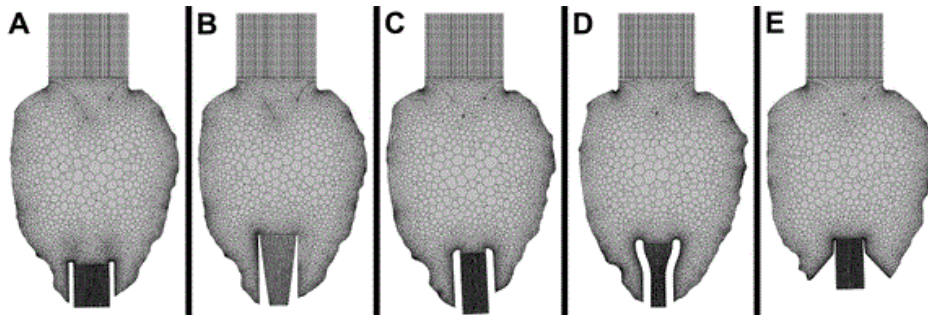
Figure 2.11: Meshing of cannulated LV models A, B, C, D and E.

Regions of potential thrombus formation were defined by fluid volumes with low velocity magnitudes (less than 0,001 m/s) and strain rates of less than 2 s^{-1}. Comparative analysis allowed to identify that cannula E (inferiorly flared) had the lowest amount of persistent stagnation areas, which was possibly due to the smoother transition between the cannula and the endocardium (Figure 2.12).

Intraventricular end-diastolic flow profiles presented a large dominant clockwise rotation, which confirmed echocardiographic data; in particular, the simulation with cannula E

revealed more distinct vortices close to the ventricular apex, confirming enhanced blood mixing and reduced stagnation areas.

Overall, all cannulae had similar rates of LV washout and exhibited similar blood residence times, but the inferiorly flared cannula was found to have the lowest risk of thrombus formation, that, in general, is not solely dependent on cannula insertion length but also on cannula geometry.

One major limitation of the presented model is the static LV. Indeed, some low residual contractility of the LV might be still present in LVAD implanted patients, so that the addition of a wall moving boundary would change regions of possible stagnation and rate of LV washout.
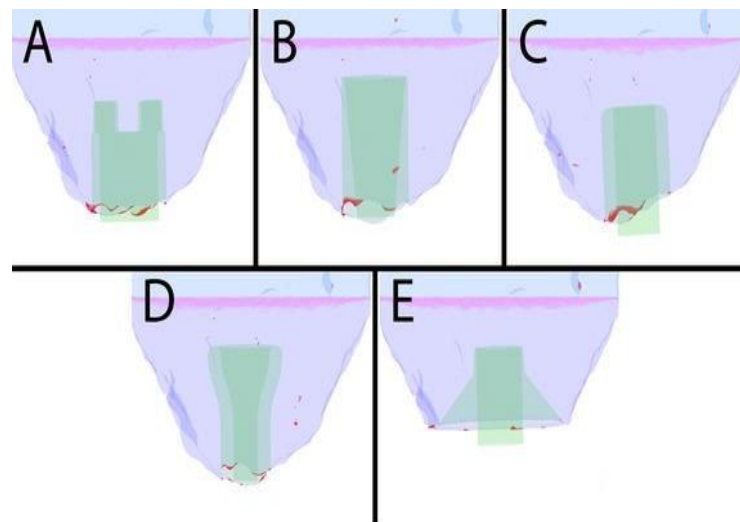

Figure 2.12: Thrombus risk rendering of the cannulation region, with the persistent stagnation volumes shown in red. Cannula design references are labelled A–E.

In a 2017 study, Prisco *et al.* [30] hypothesized that LVAD inflow cannula insertion site could affect stagnation of blood flow within the LV. For what concerns LVAD implantation, two potential surgical configurations were modelled: apical and diaphragmatic (Figure 2.13).

In the apical configuration, the inflow cannula was inserted into the LV apex, where its long axis is perpendicular to the mitral valve, while, in the diaphragmatic implantation model the cannula was positioned parallel to the short axis of the LV and anterior to the papillary muscle insertion.
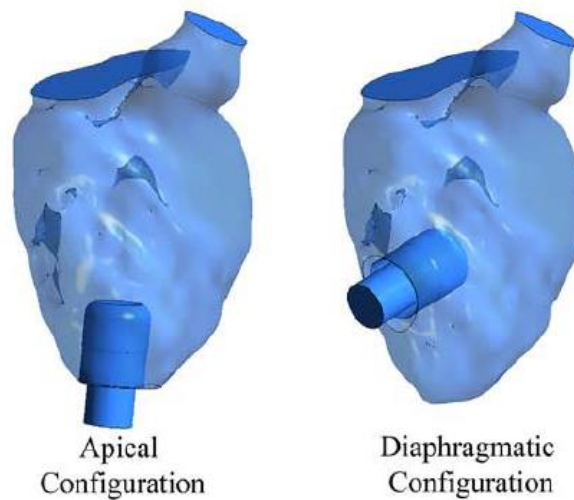
Figure 2.13: Inflow cannula configurations.

To test VAD-induced blood stagnation, the inflow cannula 3D geometry was derived from the *HeartWare* VAD model (HeartWare Inc., Miami, FL, USA), while the 3D LV model was reconstructed from a set of CT scan images of a patient affected by HF. The ventricle was modelled as a rigid body with no moving wall condition, assuming the LV cross section to vary minimally during the cardiac cycle, in an advanced HF patient.

CFD simulations were run for a total of 12 one-second cardiac cycles, comparing not only diaphragmatic and apical configurations, but also testing whether intermittent AV (Aortic Valve) opening would decrease the amount of stagnating blood with respect to a condition characterised by an always closed AV.

A modest difference in stagnation was observed between the apical and diaphragmatic configurations, but significantly lower stagnation was observed when intermittent AV opening was modelled (Figure 2.14).
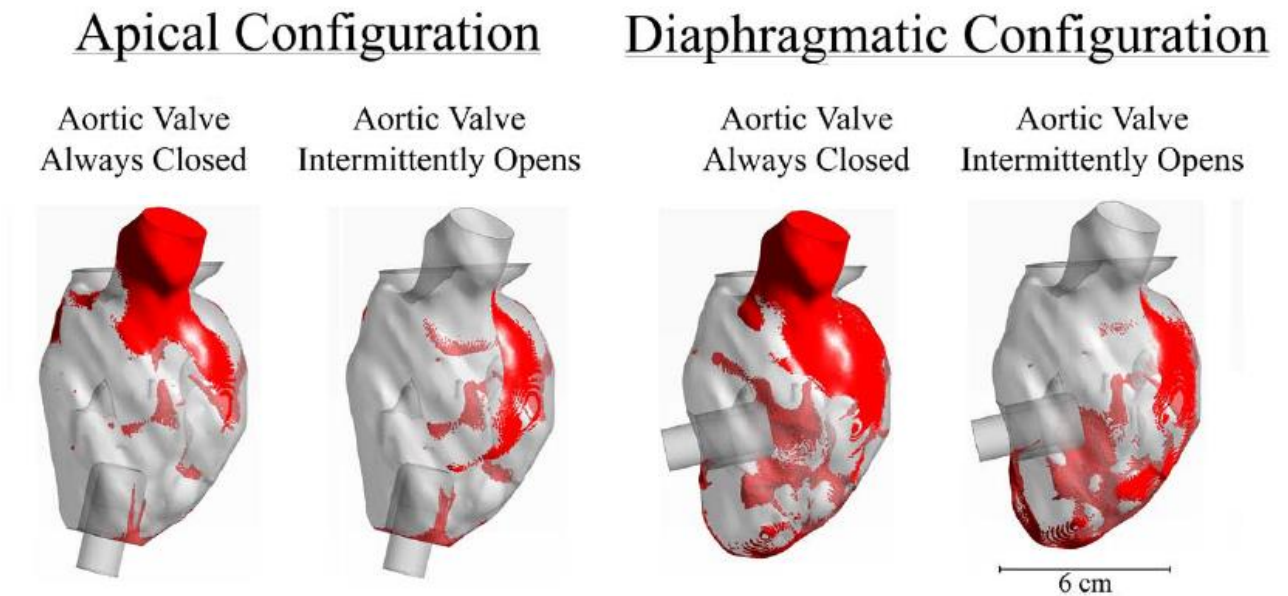

Figure 2.14: Visualization of stagnation zones. After 12 seconds of simulation, the remaining red ink was visualized in each geometry.

Three limitations were acknowledged: the heart was modelled as a rigid structure, the LV blood flow was assumed to be laminar, and a single-patient geometry was considered.

LV Wall Motion

More recently, Liao *et al.* [49] published a new study presenting a 3D multiscale computational fluid dynamic model of the LV, to evaluate the risk of thrombosis with varying inflow cannula insertion lengths, in a dilated LV. The multiscale numerical model consisted of 3 sub-models: a CFD model of the LV, a lumped parameter network (LPN) of the cardiovascular system and a finite element model of the LV wall.

The geometry of a severely dilated LV (end-systolic volume equal to 460 ml) was reconstructed from computed tomography, with the cannula longitudinal axis intersecting the apex and the mitral valve (MV) plane. Four different cannula insertion lengths were analyzed, as it is shown in Figure 2.15.
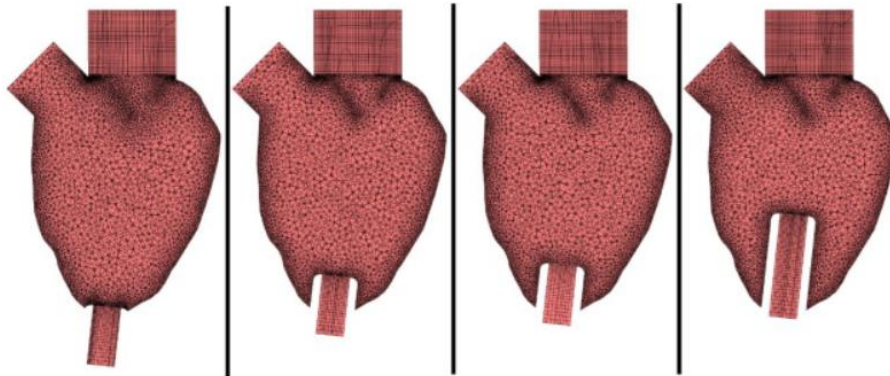
Figure 2.15: Meshed cannulated LV models with different insertion lengths. From left to right: 5 mm, 19 mm, 24 mm and 50 mm.

As a pre-processing step, a finite element model was carried out to compute the ventricular wall displacement. In such model, the heart wall was described by a constant fictitious material, loaded with a LV time-dependent pressure that, in turn, was generated by the LPN of the circulation.

Moreover, the LPN transferred this LV pressure profile and the transmitral flow rate (Figure 2.16) to the CFD model. The pressure was constantly applied to the cannula outlet, while the transmitral flow rate was applied to the MV. After each iteration, the cannula flow rate was measured and compared to the LPN LVAD flow rate to balance any possible difference.
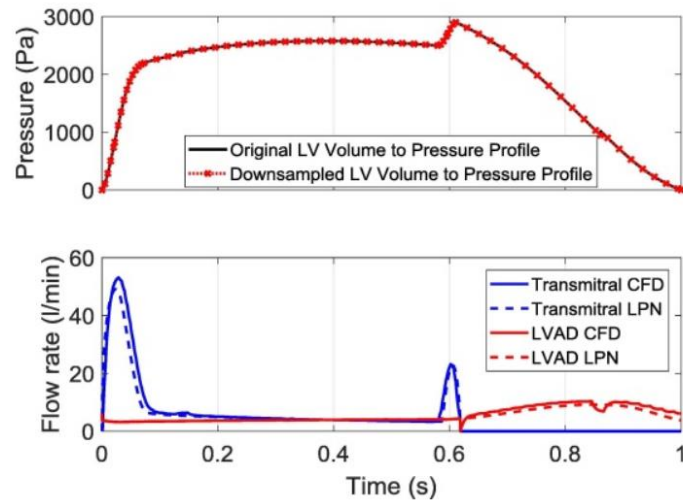
Figure 2.16: Top panel: the converted LV volume profile to pressure with downsampled and shifted data points. Bottom panel: comparison of the ideal flow rates obtained from the LPN and flow rates in the CFD model.

Results suggested that a longer cannula insertion length promoted LV washout, evaluated thanks to a virtual ink approach, and increased velocities around the left ventricular outflow tract, consequently decreasing the risk of thrombosis. Mean stagnation volumes over 2 cardiac cycles (identified as areas where the instantaneous velocities < 0.001 m/s and the strain rate < 100 s^{-1}), in a region 10 mm above the apex, are shown in Figure 2.17.

Limitations of this work are the single patient-specific LV investigation and the balloon-like movement assumed for the LV, neglecting internal features.

Figure 2.17: Mean stagnation volumes for different cannula insertion lengths.

2.3. *In Vitro* Analysis of LV-LVAD Hemodynamics

Computational analysis is playing a major role in the development and evaluation of LVADs performances. It is useful for predicting flow three-dimensional velocities and wall-shear rates t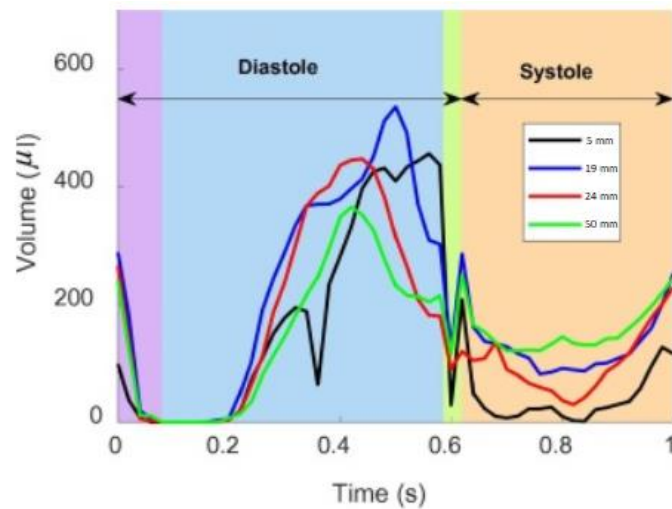hrough the entire LV geometry. Though, for a complete review of the methodologies and approaches implemented in literature, we report studies describing *in vitro* characterization of the intraventricular flow patterns in the LVAD-assisted heart. However, *in vitro* testing, when associated to a computational model, can be used to assess the accuracy and reliability of CFD simulations.

In vitro Particle Image Velocimetry (PIV), an optical flow measurement technique, is used for computational validation. Generally, the experiments are conducted in a mock circulatory loop, allowing hemodynamic physical reproduction of the heart and circulatory system. Physiological atrial and aortic compliances are simulated [50] using piston-type compliance chambers. The systemic resistance is usually mimicked by a parallel plate resistor, located downstream of the aortic compliance chamber. Finally, the preload to the LVAD chamber is controlled by a reservoir located between the systemic resistance and the atrial compliance. PIV analysis is used to obtain non-invasive, instantaneous, spatially resolved velocity measurements [50].

Through PIV, Laumen *et al.* [51] investigated the effect of various inflow/outflow cannula tip geometries and positions on ventricular and greater vessels flow patterns to evaluate ventricular washout.

As PIV needs a camera to record the particles moving, a transparent model of the left ventricle was required. Therefore, MRI data of a patient with dilated cardiomyopathy were employed to reconstruct the LV geometry, the final model representing a dilated LV in end systole, with an internal volume of 250 ml. The LV was printed by a rapid prototyper using an acrylic photopolymer and then coated with a silicone layer of 2-mm thickness.

Ventricle pulsatility was reproduced suspending the LV in a water/glycerol-filled pressure chamber connected to a pump, that, by changing the pressure within the chamber, deformed the ventricle.

Through the LV apex, two different cannulae were inserted: a cannula with an angular tip design, and a cannula with a trumpet-shaped tip (Figure 2.18).
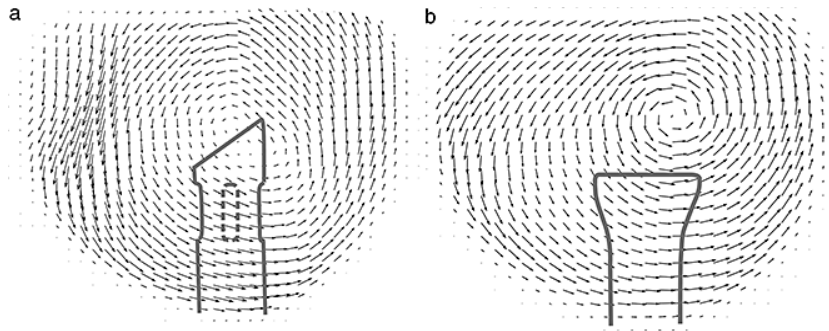
Figure 2.18: Cannulae geometry: a) angular design; b) trumpet-shaped.

The flow field was measured with PIV, which is based on the detection of the movement of illuminated particles released within the flow stream, and the recorded images were analyzed. Results showed that cannula placement had a high impact on blood flow. Measurements suggested placement of the LVAD inflow cannula in the LV outflow tract (LVOT) to improve ventricular chamber washout, while the tip design had smaller influence on the vortex centres creation.

Wong *et al.* [52] quantitatively evaluated the flow patterns in the LVAD-assisted LV, with a focus on alterations in vortex development and stasis, again using PIV in a mock circulatory loop.

To anatomically mimic the flow geometry of the assisted-ventricle, the *HeartMate II* LVAD (Thoratec Corp., Pleasanton, CA, USA), was inserted into a transparent LV, modelled with a thin-walled silicon rubber sac and suspended in a fluid filled chamber. To generate the pulsatile cardiac function of a HF patient, a velocity profile, reproducing transmitralic and aortic flow rate patterns, was applied to the LV by the simulator's piston pump.

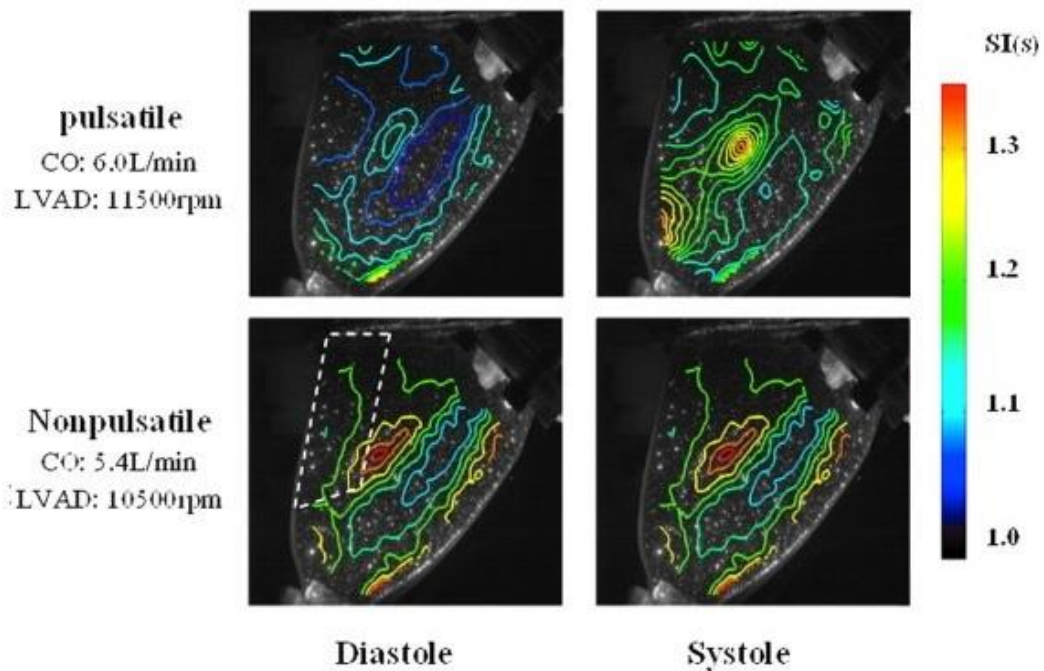Figure 2.19 : Spatial distribution of the stagnation index, SI, over the ventricular midplane in different flow conditions. The higher the SI value, the lower the local velocity and the greater the flow stasis.

Simulator settings were varied over a wide range to ensure coverage of physiological conditions. Seven different LVAD rates (6500–12500 rpm) and simulated cardiac function (On/Off) were combined to create a matrix of 15 test conditions. The 15 flow settings resulted in four basic intraventricular flow patterns: *pre*-LVAD, parallel pulsatile, series pulsatile and nonpulsatile. The velocity field was measured in the cardiac simulator using digital PIV.

The results of this *in vitro* study demonstrated that, under pulsatile conditions, vortex formation in early diastole was relatively unchanged by LVAD support, but vortex decay followed a different course. Flow stasis in the LVOT under pulsatile conditions did not vary during diastole with LVAD support, but increased in systole and was high and constant with nonpulsatile flow conditions, i.e. when the heart was not contracting (Figure 2.19). These findings suggested that continuous flow LVAD support did not substantially disrupt normal vortex dynamics unless cardiac function was minimal and pulsatility was absent. The altered blood flow introduced by the LVAD resulted in flow stasis adjacent to the LVOT, which increased the risk of thrombus formation in the heart.

Since the simulator design was based on a 3-element Windkessel model to simulate the circulatory system impedance, the experimental setup could not adapt to changes in pressure and flow like the native cardiovascular system; hence, the impedance remained unvaried until the settings were changed. Furthermore, as in the previous study, pulsatile cardiac function was achieved by compressing the ventricle, neglecting the effect of myocardial twist, which has shown to be relevant as for cardiac energetics. Lastly, LV size decreases and native ventricular contractility can be partially recovered in patients after LVAD implantation, a condition that was not considered in this study.

To summarize, several literature studies [38, 41, 43] provided insights on how cardiac pathologies, such as dilated cardiomyopathy, alter intraventricular flow field. Moreover, a conspicuous number of studies [30, 44-48] focused on analysing the disturbed flow dynamics and the thrombogenic potential of the LV in presence of LVAD inflow cannula. However, two weak points, affecting most of the examined literature, were identified: first of all, when modelling ventricular wall motion, only myofibers contraction was included, and the complete absence of torsion prevented to achieve realistic simulations of cardiac dynamics; secondly, when characterizing LV-LVAD hemodynamics, the LV was generally considered as a rigid and static body, neglecting any residual contractility. After LVAD implantation, LV size decreases due to cardiac remodelling, and native ventricular contractility can be partially recovered. The addition of a wall moving boundary in CFD simulations would change regions of possible stagnation and rate of LV washout.

In this study, we hypothesized that HF-LV residual contractility can be identified as a possible thrombogenic factor, among other mechanisms promoting intraventricular thrombus formation (see §1.2.2): accordingly we sought to evaluate the mutual contribution of low values of residual contractility, and of fluid flow alterations due to the implantation of a LVAD inflow cannula, as for generation of intraventricular hemodynamics enhancing prothrombotic conditions.

Furthermore, in order to overcome some of the limitations of current literature studies, the dynamics of the heart was modelled including both myofibers contraction and torsion,

through the prescribed moving boundaries approach, by assembling a set of mathematical equations to formulate wall motion; wall motion was implemented for the *pre* as well as for the *post* implant models.

In addition, the cannula real insertion point and orientation were retrieved from imaging-based reconstruction techniques of a patient-specific LV model.

3.   Materials and Methods

In this study, LV residual contractility was evaluated as one of the contributing factors promoting thrombogenesis in a LVAD-supported heart: low values of residual ejection fraction (EF%), through which LV residual contractility was quantified, combined with intraventricular hemodynamics alterations due to the implantation of the LVAD, were hypothesized to drive prothrombotic conditions.

We were interested in characterizing how the mutual interactions between residual contractility in a failing ventricle, degree of LVAD support (i.e. the LVAD flow rate), and LVAD inflow cannula positioning alter intraventricular flow dynamics and how they contribute to the LV thrombogenic potential.

A patient-specific LV model was developed, able to accurately reproduce the disturbed intraventricular blood flow patterns induced by dilated cardiomyopathy as well as the hemodynamics associated to the LVAD implantation.

Through a geometry prescribed approach (see § 2, p. 21), LV contraction and torsion were implemented. In particular, LV wall motion was imposed through the implementation of User Defined Functions (UDFs), which assign a displacement to the mesh nodes, to faithfully reproduce LV movement during systole and diastole.

Three sets of simulations were conceived in order to analyze the complex phenomena described above:

- Set 1 (*Pre-implant*): This set consists of three simulations, the fluid dynamic domain being a pathologically dilated patient-specific LV.
  Transient CFD simulations of the whole cardiac cycle were carried out, considering a set of three residual EF% (15% - 10% - 5%), corresponding to increasing levels of cardiac impairment, that is from moderate to severe LV HF.
  Through this set of simulations, the role of LV residual contractility as a possible thrombogenic factor was explored, by analyzing blood velocity patterns, blood stasis, and associated WSS trends in the apical region. Furthermore, results from

these simulations were used as basis for comparison with *post* inflow cannula implantation data.

- Set 2 (*Post-implant A*): The CFD model is based on the same pathologically dilated patient-specific LV of Set 1, *post* LVAD implantation. Patient-specific inflow cannula positioning was derived from imaging techniques and reconstruction process. This set consists of a matrix of 8 test conditions, obtained combining 4 values of residual EF% (0 - 5 - 10 - 15%) with 7 levels of support (LVAD flow rates). This way, the interplay between myocardial residual contractility and LVAD flow rate was evaluated.

- Set 3 (*Post-implant B*): This set consists of 2 test conditions, selected from Set 2 simulation matrix. These 2 configurations were chosen considering the total cardiac output (CO) provided to the patient, that is the sum of native residual CO and LVAD flow rate. Total CO was assigned equal to 5 L/min, a condition mimicking the average cardiac output at rest, so as to refer to real clinical data.
  In this set of simulations, cannula position was varied: it was modelled so that the inflow cannula longitudinal axis intersects the LV apex and the centre of the mitral valve orifice.
  The aim was to quantify the impact of cannula position on LV thrombogenicity, so to identify the most hemodynamically favourable LVAD implantation configuration.

In each simulation set, blood flow characteristics, such as shear stress, stagnation zones and recirculation patterns were assessed.

3.1. Geometry of the Fluid Dynamic Domain

3.1.1. Segmentation of the Pathological Patient-Specific LV Model

The geometrical model of the pathological patient-specific LV was provided by the Biomechanics Group of the DEIB of the Politecnico di Milano.

In detail, imaging data were collected by means of 3D trans-thoracic echocardiography (3DTTE), with ECG gating over 4 consecutive cardiac cycles (VIVID-E9, GE Healthcare, Little Chalfont, Buckinghamshire, UK), performed on a candidate to LVAD implantation, in collaboration with the medical staff of San Raffaele Scientific Institute and the research staff of UniSR.

The examined patient is affected by dilated cardiomyopathy, a condition in which, due to reduced contractility of myocardial fibres, the heart is no longer able to pump blood properly and, therefore, a lower ejection volume is produced, if compared to the physiological one.

Two acquisitions were performed:

- pre-implantation (*pre*): data were obtained positioning the probe as for acquiring an LV-focused apical 4-chamber view;
- 1-month post-implantation (*post*): data were registered positioning the probe as for acquiring a long-axis parasternal 3-chambers projection, avoiding LVAD-related artifacts.

An in-house reconstruction strategy, *ad-hoc* developed within the Biomechanics group of Politecnico di Milano, was exploited. The *pre*-dataset was processed in order to reconstruct the 3D surface of the endocardium (*Endo-pre*), while the *post* dataset allowed to determine the inflow cannula position. Finally, the cannula profile was rigidly co-registered onto the 3D LV surface, creating the final geometry LV+LVAD (Figure 3.1).

In detail, the point cloud of the cannula profile was rigidly co-registered onto *Endo-pre*; the associated roto-translation was identified as the spatial transformation that makes the annular profile of the *post*-dataset (*Ann-post)* matching with the annular profile of the *pre*-dataset (*Ann-pre)* both in position and orientation. In particular, it was imposed that *i)* the

centroid of *Ann-post* would match the centroid of *Ann-pre*, *ii)* the least-square fitting plane of *Ann-post* would have the same normal as compared to least-square fitting plane of *Ann-pre*, and *iii)* the saddle-horn (SH, namely, the peak of the anterior tract of the MV annular profile) *-post* would match *SH-pre*.
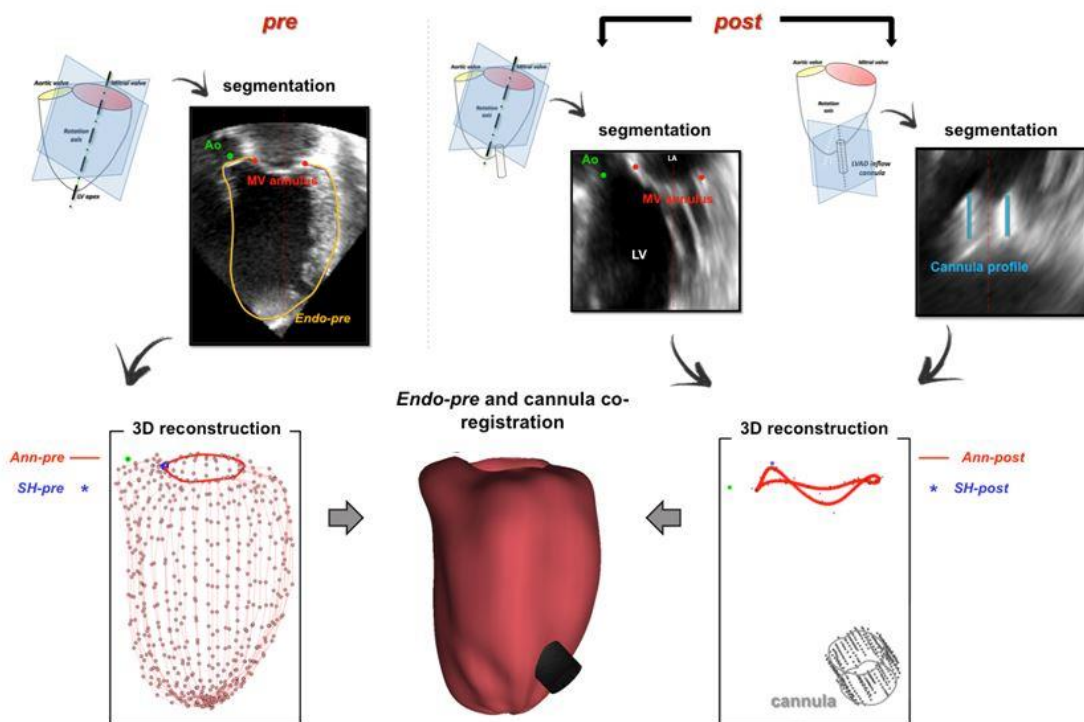
Figure 3.1: Schematics of the procedure for co-registration of the cannula onto the pre-implant LV endocardium volume, allowing reconstruction of the patient-specific 3D model of the LV+LVAD inflow cannula.

A STL file, that is a raw, unstructured triangulated surface, of the LV in the end-diastolic configuration was provided via segmentation of the 3DTTE data and subsequent reconstruction process. Then, the STL file was imported, smoothed and remeshed in Meshmixer (Autodesk Inc.), in order to improve the smoothness of the ventricular surface. The result is shown in Figure 3.2.

Figure 3.2: Original end-diastolic LV (left) and the result of smoothing and remeshing operations (right).

3.1.2. Pathological Patient-Specific Geometry
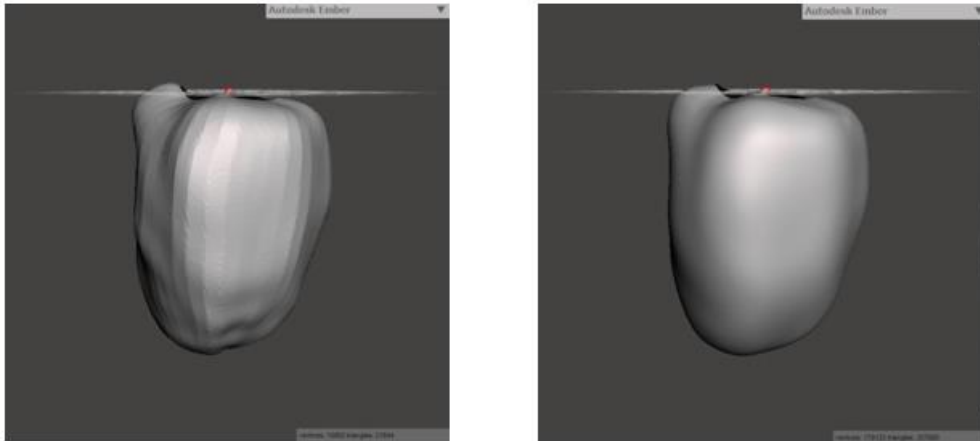
Pre - Implant Model

The STL file of the smoothed LV was imported and processed in the 3D CAD Software SpaceClaim (ANSYS 18.1). A shell of the LV was obtained from the STL thanks to a reverse engineering approach, employing the Skin Surface tool. This tool allowed to create patches, adherent to the surface of the LV and following its curvature, through an automatic surface fitting along triangular facets of the STL file. Eventually, these patches were matched to create the LV shell.

To guarantee a fully developed flow during the simulations, a synthetic/paradigmatic portion of the atrium chamber and of the proximal aorta were created.
The left atrium was modelled as a circular truncated cone, whose interior profile matched that of the mitral valve of the LV model, while the major basis was a circle (radius 27 mm), sketched about 10 mm above the mitral plane. These values guaranteed fully developed blood flow within the LV.

The aorta was approximated with a cylinder (radius equal to 12 mm, 14 mm of length), with the interior profile matching that of the aortic valve in the LV model.

The complete geometry is reported in Figure 3.3.
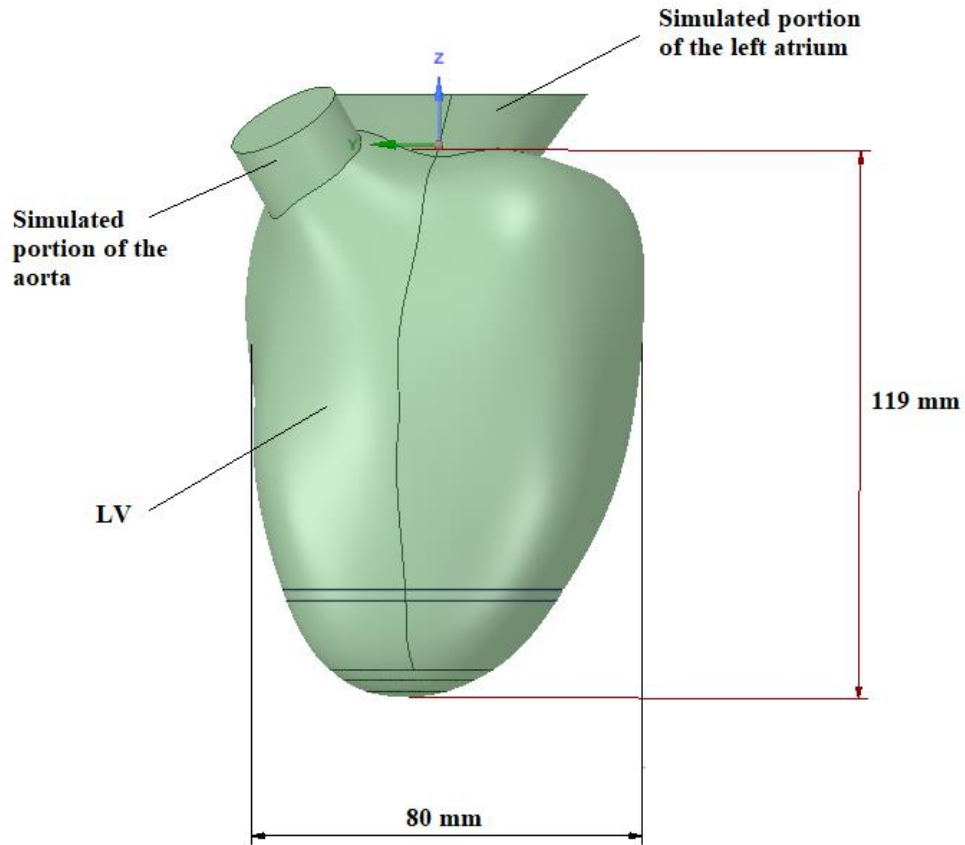
Figure 3.3: *Pre-implant* geometry.

Post - Implant Model A

The 1-month post-implantation (*post*) STL file provided the exact insertion positioning of the LVAD inflow cannula in the LV myocardial wall.

To model the LV+LVAD inflow cannula *post*-implant geometry, the *pre*-implant fluid domain and the 1-month *post*-implantation STL file were overlapped in SpaceClaim (ANSYS 18.1), in order to accurately co-register the cannula insertion region from the STL

file to the *pre*-implant LV body. Then a cylinder was used to recreate the cannula, once its position and its physical dimensions (radius 9 mm, length 15 mm) were known. The cannula protrusion depth was 18 mm. Moreover, the cannula length was increased from 15 mm to 50 mm, to ensure a fully developed fluid flow along its length (Figure 3.4).
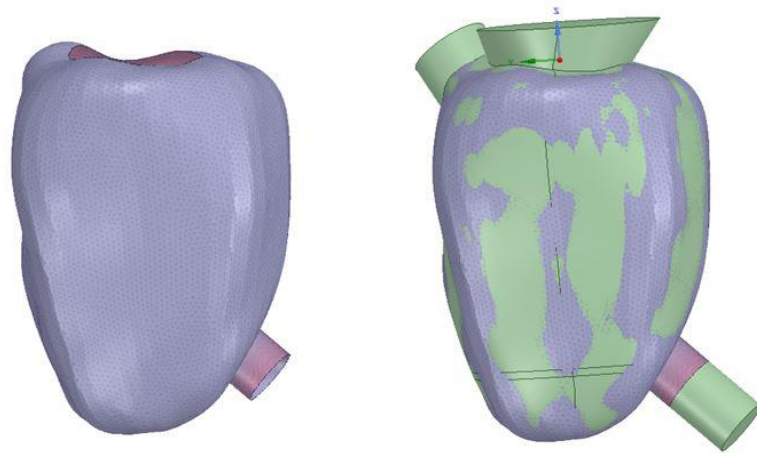

Figure 3.4: Left: 1-month post-implantation STL file provided by the segmentation process. Right: Overlapping of the pre-implant geometry and the 1-month post-implantation STL file; as it can be noticed, the designed and the STL cannula profiles correctly match.

Finally, the ventricle and the cannula were combined (the shared volume was selected and deleted from the ventricular body) and an automatic shared topology function in SpaceClaim was applied on the two bodies to guarantee mesh continuity.

The complete geometry is shown in Figure 3.5a.

Post - Implant Model B

The third fluid dynamic domain was obtained combining the *pre-implant* LV geometry and the LVAD inflow cannula design from *post-implant* A model. Herein, the cannula tip was inserted directly into the LV apex, so that the inflow cannula longitudinal axis intersects the LV apex and the centre of the mitral valve orifice. Finally, again, the ventricle and the cannula were combined (the shared volume was selected and deleted from the ventricular

body) and a shared topology function was applied on the two bodies to guarantee mesh continuity.

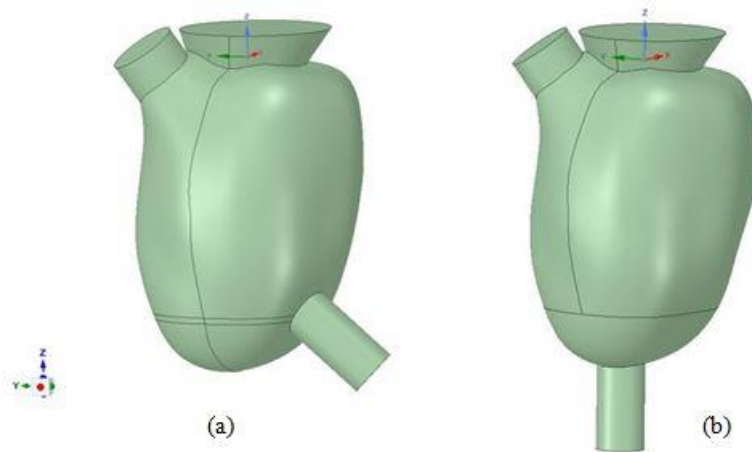The complete geometry is shown in Figure 3.5b.

Figure 3.5: (a) *Post-implant* A geometry (LV+LVAD); (b) *Post-implant* B geometry (LV+LVAD).

3.2. Mesh

3.2.1. Mesh Sensitivity Analysis

A mesh sensitivity analysis was performed in order to identify the proper number of grid elements to guarantee an accurate solution as well as a reasonable computational time.

The mesh independence study was carried out on the *pre-implant* model, being the LV body shared by the *pre, post-implant A* and *B* configurations.

Six tetrahedral meshes were considered, ranging from a coarse mesh of $\sim 10^5$ elements to a finer mesh of $\sim 6 \times 10^5$ elements, assuming an incremental step of $+10^5$ cells between each mesh.

The investigated meshes and relative sizing parameters are collected in Table 3.1.

	Mesh 1	*Mesh 2*	*Mesh 3*	*Mesh 4*	*Mesh 5*	*Mesh 6*
N° of elements	102803	205174	302529	405941	503918	606315
Min Size	10^{-4}	10^{-4}	10^{-4}	10^{-4}	10^{-4}	10^{-4}
Max Face Size	$3.4 \ 10^{-3}$	$2.7 \ 10^{-3}$	$2.37 \ 10^{-3}$	$2.15 \ 10^{-3}$	$2 \ 10^{-3}$	$1.88 \ 10^{-3}$
Max Tet Size	$3.4 \ 10^{-3}$	$2.7 \ 10^{-3}$	$2.37 \ 10^{-3}$	$2.15 \ 10^{-3}$	$2 \ 10^{-3}$	$1.88 \ 10^{-3}$
Growth Rate	1.2	1.2	1.2	1.2	1.2	1.2

Table 3.1: Mesh parameters.

In order to evaluate the solution discrepancy between meshes, velocity magnitude temporal trends averaged in three pre-defined regions close to the ventricular apex (Figure 3.6) were extracted; sensitivity analysis data were computed in this specific zone of the LV since the apex is the region of interest of the study, i.e. we wanted to evaluate the prothrombotic potential associated with the intraventricular hemodynamics at the LV apex.
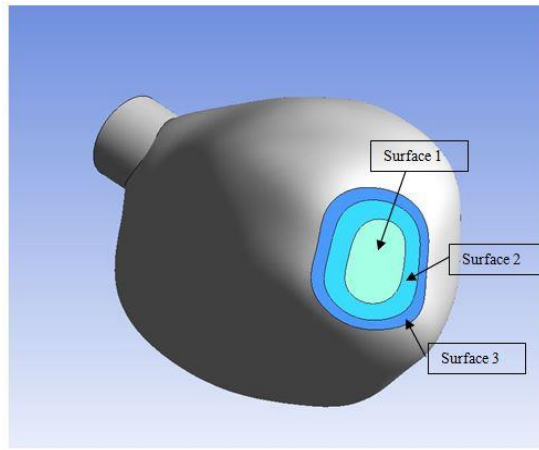
Figure 3.6: Regions close to the ventricular apex exploited for the mesh independency study.

Cell centre velocity magnitude values were extracted and stored in ASCII files at each time step (0.001 s in all the simulations), for each grid element of the three zones. Thanks to a MATLAB script, the ASCII files were processed obtaining average velocity magnitude trends, one for each of the three regions. This procedure was repeated for all the meshes. Then, considering one region at time, at each time step, the percentage error between average velocity magnitude values, for two subsequent meshes, was determined (Figure 3.7a). After that, the mean percentage error (MPE) was computed, so that three MPE were defined per mesh, one for each apical region (Figure 3.7b).

We imposed that the proper mesh must guarantee, for each of the considered zones, a value of MPE lower than 2%. The mesh that fulfilled this criterion was *Mesh 4* (see Table 3.2).

	Surface 1	*Surface 2*	*Surface 3*
MPE - Mesh 1-2	6.88%	4.03%	3.69%
MPE - Mesh 2-3	2.08%	2.26%	2.21%
MPE - Mesh 3-4	1.95%	2.29%	1.58%
MPE - Mesh 4-5	1.40%	1.75%	1.26%
MPE - Mesh 5-6	1.39%	0.74%	1.61%

Table 3.2: MPEs between subsequent meshes, computed for each of the apical surfaces.

A

B

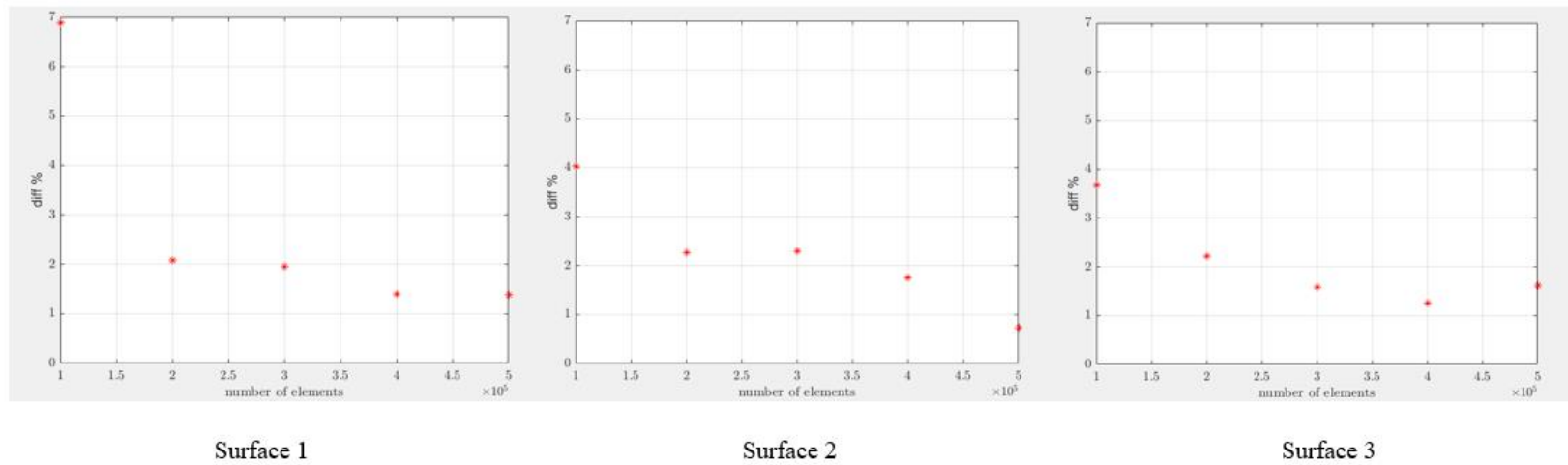Surface 1   Surface 2   Surface 3
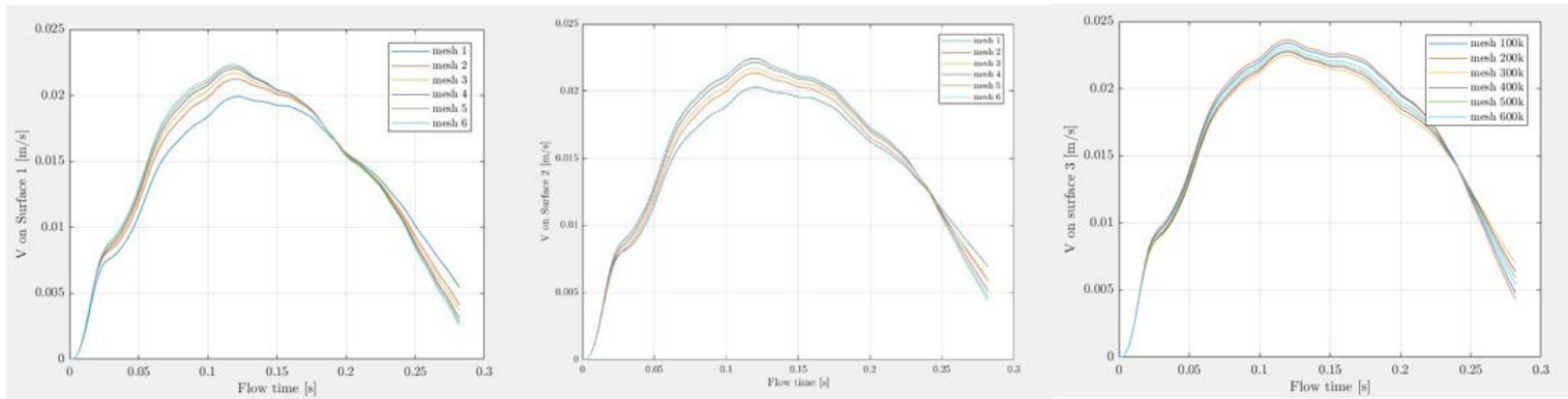
Figure 3.7: (A) Comparison between average velocity magnitude trends, extracted from Surface 1 (left), Surface 2 (middle), and Surface 3 (right) in all the considered meshes. (B) MPEs between subsequent meshes. Data refer to Surface 1 (left), Surface 2 (middle), and Surface 3 (right).

3.2.2. *Pre - Implant* Model

According to the sensitivity analysis, the geometry was discretized in the meshing component of ANSYS 18.1 with 405941 tetrahedrons and 71772 nodes. The mesh is shown in Figure 3.8.

A uniform size function was selected, in order to create a homogenous grid in the entire domain, the mesh refinement based on the parameters listed in Table 3.1, for the selected mesh.

For what concerns the named selections, the following surfaces were labelled: *ventricle, aorta, aortic valve, atrium, mitral valve,* to assign proper boundary conditions (Figure 3.8).
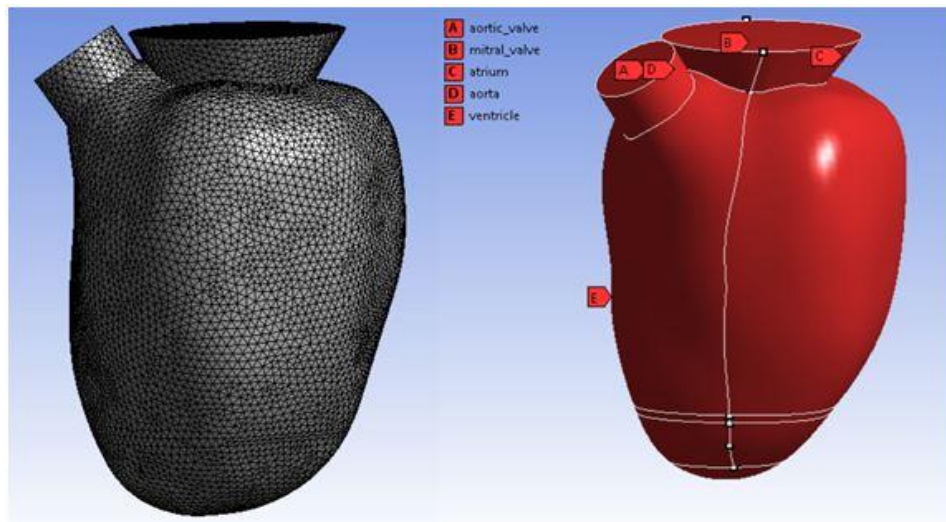
Figure 3.8: Left: Selected mesh for the *pre-implant* configuration. Right: Named selections.

3.2.3. *Post - Implant* Models A and B

The *pre-implant* mesh sizing parameters were also exploited to generate the *post-implant* meshes, obtaining a grid of 414028 tetrahedrons and 73428 nodes for model A and a grid of 412824 elements and 73206 nodes for model B.

The meshes are shown in Figure 3.9.
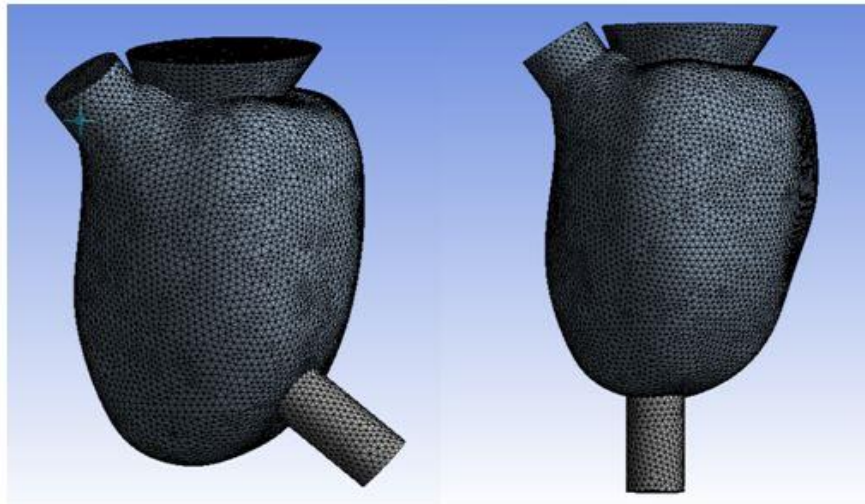
Figure 3.9: *Post-implant* A (left) and B (right) meshes.

Three more named selections were added: *i) cannula*, *ii) cannula2* to assign boundary conditions on two portions of the cannula, the first one is the portion external to the ventricular apex and the second one is that protruding inside the ventricle; *iii) velocity_inlet* for the cannula base outside the ventricle (Figure 3.10-3.11).

The second base of the cannula, internal to the LV, was not named to connect the fluid domain of the cannula with the one of the ventricle.
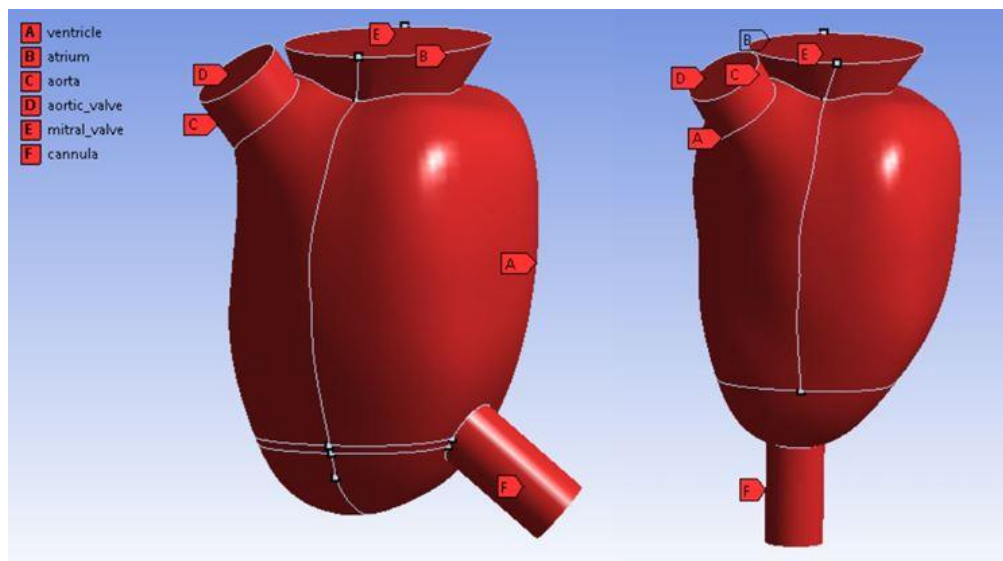
Figure 3.10: *Post-implant* A (left) and B (right) models named selections.
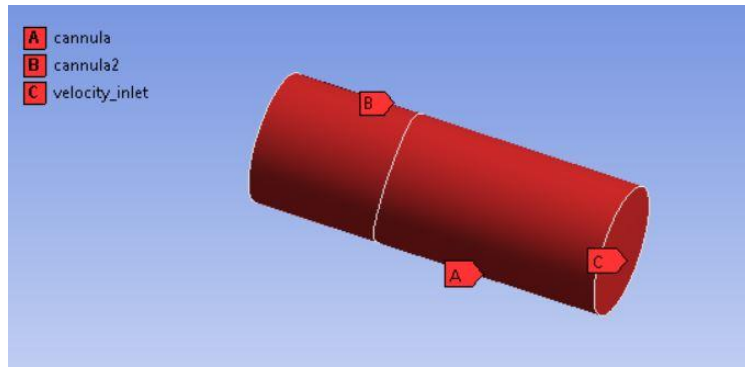
Figure 3.11: Cannula named selections.

3.3. Grid Motion

In the present study, wall motion was defined through a set of mathematical equations, according to a geometry-prescribed approach, so that the movement of the LV wall was imposed as a boundary condition of the fluid domain.

In a cardiac cycle, the ventricular motion is characterised by contraction and twist during systole, and dilation and untwist during diastole. To reproduce this peculiar movement, the mesh motion functionality of ANSYS Fluent 18.1 was exploited, by compiling and loading a specifically set up User-Defined Function (UDF).

A UDF is a function that can be dynamically loaded with the Fluent solver to enhance the standard features of the code. UDFs are written in the C programming language.
The UDFs used in the simulations were generated exploiting a MATLAB code (The MathWorks Inc., Natick, MA, USA) developed in a previous work [53], that was adapted to current geometries and modified so as to allow ventricular motion of the LV+LVAD models. Indeed, this feature was not present in the previous code and it was originally developed in the present work.

3.3.1. Left Ventricle Wall Motion: *Pre - Implant*

When modelling LV wall motion, it must be considered that the valvular plane and the ventricular region above the cut-off plane shown in Figure 3.12 remained fixed. As a consequence, the UDF applied the mesh motion only to the LV grid nodes below this plane.

In order to replicate LV rotation and translation, the UDF assigned, to each node of the ventricular grid, three values of displacement, u_x, u_y and u_z, along the three directions of the Cartesian reference system.
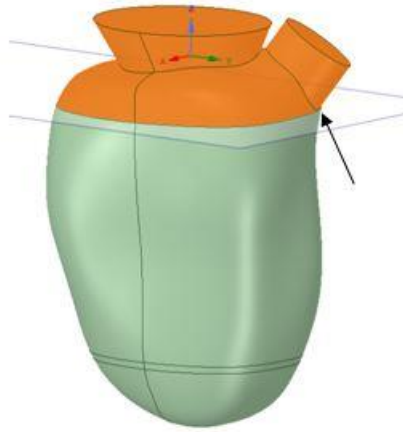
Figure 3.12: Visualisation of the fixed (orange) and moving (green) regions of the LV. The cut plane is orthogonal to the z axis and passes through the contact point (black arrow) between the LV wall and the aorta.

Contraction and Dilation

The contraction/dilation movement was obtained by assigning to each node a displacement $u_\perp(z,t)$, normal to the ventricular wall and expressed as (eq.1):

$$u_\perp(z,t) = \pm k\,\delta(z)f(t)\sigma(z)g(t) \qquad (1)$$

where the + refers to the systolic phase of the cardiac cycle, while the - to the diastolic one.

$\delta(z)$ in (1) is a 15th order polynomial that was used to assign the proper displacement to the mesh nodes as a function of the z coordinate, namely the axial direction of the ventricle. This function was calculated under the hypothesis of homothetic contraction of the LV.

The $\delta(z)$ function was determined for each simulation setting, following a standardized procedure. It was obtained by interpolating the elements of a distances vector; these distances were computed between sampled points of two semi-ellipsoids, the end-systolic and the end-diastolic, through which the ventricular profile was described.

As first step of the standardized procedure, the moving portion of the LV (in the end-diastolic configuration, starting point of all simulations) was modelled as a half prolate ellipsoid, whose geometrical parameters are reported in Figure 3.13.

The LV long axis (semi-major axis of the ellipsoid) was defined as the distance among the LV apex and a plane passing through the contact point between the LV wall and the aorta, closest to the apex.

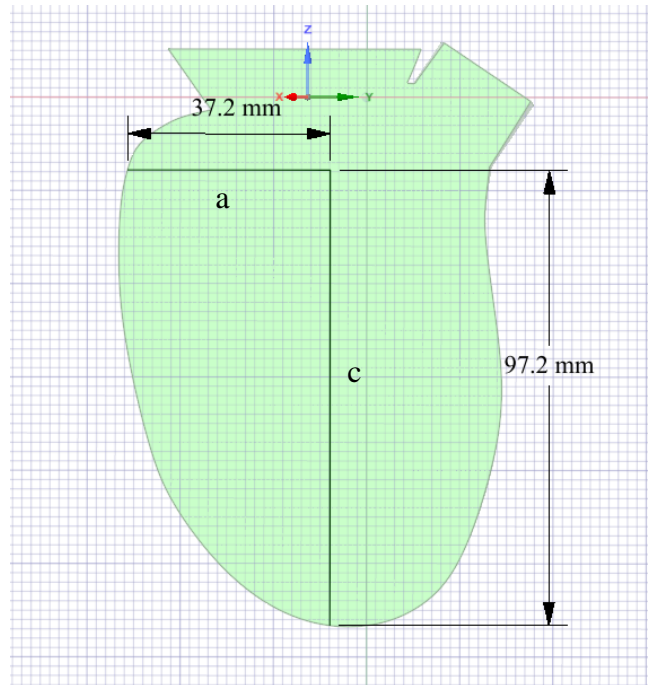Figure 3.13: LV semi-major (c) and semi-minor axis (a) are 9.72 cm and 3.72 cm long, respectively.

Then the end-diastolic volume of the moving zone was evaluated thanks to the following equation (eq. 2):

$$V_{end-diastole} = \frac{\frac{4}{3} \pi \, a \, b \, c}{2} \qquad (2)$$

where a and b are the two semi-minor axis in the xy plane, considered as equal, and c is the above-defined semi-major axis (Figure 3.13). This equation allowed to evaluate the volume of a semi-ellipsoid.

Depending on the desired residual EF% (as mentioned before, EF% was used to assign different degrees of LV residual contractility), a volume variation was applied to the end-diastolic ellipsoid, computed as follows (eq. 3):

$$\Delta V = V_{end-diastole} - V_{end-systole} = EF\% * V_{end-diastole} \qquad (3)$$

This equation allowed to determine the volume of the semi-ellipsoid approximating the end-systolic configuration. Moreover, by applying again equation (2), and assuming that, because of homothetic contraction, the ratio between the semi-axis remained constant for the two semi-ellipsoids, the end-systolic semi-ellipsoid geometrical parameters (i.e. semi-major and semi-minor axis) could be determined.

Then, each of the two semi-ellipsoids was sampled with a set of points, and distances between corresponding sampled points on the two surfaces were computed.

At this stage, all the elements of the displacement vector were determined: a 15th order polynomial was employed to interpolate these displacement values, obtaining the function $\delta(z)$.

Then, $\delta(z)$ function was applied to the mesh nodes to shrink or expand the ventricle, depending on the cardiac phase being simulated, until a complete overlapping of the starting semi-ellipsoid (end-diastolic) and the calculated one (end-systolic) was achieved.

Given that, in the two phases of the cardiac cycle, the ventricular profile was described by means of ideal approximating semi-ellipsoids, the ΔV (LV ejection volume) obtained in each simulation was generally lower than the expected one, making it necessary to introduce a corrective factor. The factor k ensured to obtain the desired ejection volume and was identified thanks to a trial and error process.

In systole, the function $f(t)$ in (1) is a cosine Fourier series, reproducing the physiological ejection flow rate trend in time (Figure 3.14a); on the other hand, during diastole, a sine and cosine Fourier series was used to model the physiological LV filling flow rate pattern over time (Figure 3.14b).

(a)   (b)
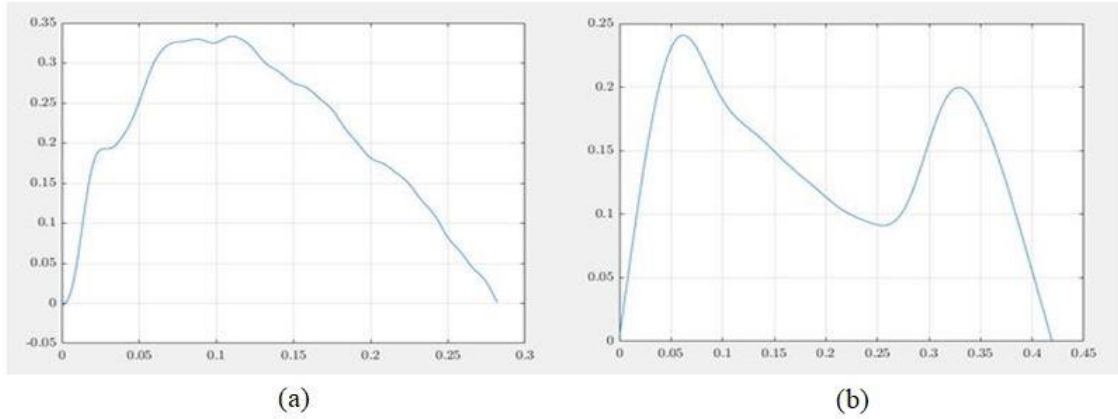
Figure 3.14: Time function f(t) during systole (a) and diastole (b).

Furthermore, the Fourier series is multiplied, both in systole and diastole, by a parabolic function $g(t)$ in (1), in order to make the mass flow rate through the mitral valve to follow the physiological trend showed in Figure 3.14b, because, actually, in diastolic phase simulations, the second peak was noticed to be overestimated. $g(t)$ is expressed as follows (eq. 4):

$$g(t) = \begin{cases} 5.7\left(\left(\dfrac{1}{k}\right)^{\frac{1}{8}} - 1\right)t^2 + 1 & in\ diastole \\[4ex] 12.6\left(\left(\dfrac{1}{k}\right)^{\frac{1}{8}} - 1\right)(t^2 - 0.564t) + \left(\dfrac{1}{k}\right)^{\frac{1}{8}} & in\ systole \end{cases} \qquad (4)$$

64

As earlier mentioned, when applying the mesh motion, only the ventricular wall moved while the valvular plane was standing still, so that a piecewise function was required to connect this two portions of the considered geometry. The function $\sigma(z)$ in (1) guaranteed a smooth link between the still and the moving regions and it was equal to 0 when the z coordinate was negative, namely when the nodes belonged to the fixed geometrical domains; 1 when the z coordinate was greater than 20 mm in the examined LV models, approximately below 1/5 of the overall vertical extension of the ventricle; otherwise was expressed by a parabolic function in (eq.5).

$$\sigma(z) := \begin{cases} 0 & if\ z \leq 0\ m \\ 8.14\ \sqrt{z + 0.0004} - 0.1628 & if\ 0 \leq z \leq 0.02\ m \\ 1 & if\ z \geq 0.02\ m \end{cases} \quad (5)$$

Torsion

For what concerns the rotational movement of the LV, it is well known that during the ejection phase the ventricular apex rotates in a counter clockwise direction while the upper portion is twisted clockwise, whereas the opposite in diastole [54].

Hence, in order to replicate the torsion, a displacement tangential to the ventricular wall $u\|(z,t)$ was assigned to each node of the mesh, in the x-y plane, defined as (eq. 6):

$$u\|(z,t) = \pm 0.0174 \ 0.56 \ R \ \delta_{rot}(z) \ f_{rot}(t) \ \sigma(z) \quad (6)$$

where, again, + refers to the systolic phase of the cardiac cycle, - to the diastolic one.
The systolic twist, which resembles the wringing of a towel, and the subsequent recoil that occurs in diastole, were realized maintaining the base fixed and linearly increasing the rotation along the ventricular axis, moving towards the apex.

In (6), R is the radius of the circumference approximating the ventricular semi-ellipsoid cross section (Figure 3.15), in the x-y plane, where each node to be moved is located. R was defined applying the Pythagoras' formulation as (eq. 7):
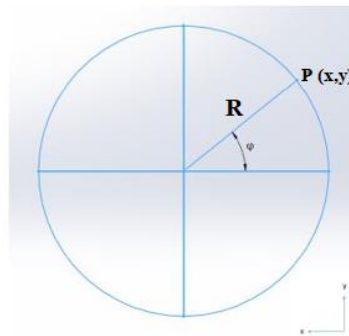
$$R = \sqrt{x^2 + y^2} \quad (7)$$

Figure 3.15: Representation of R, defined as the distance between the centre of the approximating circumference and the node P.

$\delta_{rot}(z)$ is a linear function that assign the maximum rotation to the ventricular apex, whose coordinate is referred as to z_{max}, and null rotation to the LV base (z_{min}) (eq. 8):

$$\delta_{rot}(z) = \frac{z - z_{min}}{z_{max} - z_{min}} \qquad (8)$$

$f_{rot}(t)$ has two different expressions, depending on the phase of the cardiac cycle being simulated. In systole, $f_{rot}(t)$ is a sine and cosine Fourier series describing the temporal evolution of the LV twist rate, thus interpolating the difference between the apical rotational rate and the basal one (Figure 3.16b, black curve between the two vertical dashed lines).

(a) LV rotational curves   (b) LV rotational rate curves
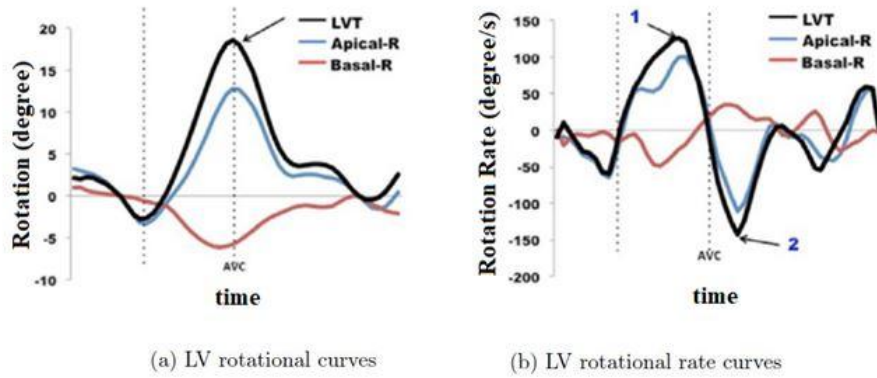
Figure 3.16: Temporal sequence of LV twist. Red lines correspond to the base, blue to the apex, black to the difference between basal and apical rotation (a) and rotational rate (b). These values are taken from a healthy subject. The point AVC corresponds to the aortic valve closure.

Similarly, in diastole $f_{rot}(t)$ is a sine and cosine Fourier series, this time representing the twist rate trend after the aortic valve closure (Figure 3.16b, second portion of the black curve). The 0.56 correction factor in (6) was introduced to take into account the reduced twisting capacity of the pathologically dilated ventricle. According to Omar *et al.* [54], patients affected by dilated cardiomyopathy and reduced ejection fraction show lower values of peak rotational rate, if compared to the physiological ones, because of the twist mechanism weakening or depletion. In dilated cardiomyopathy, twist mechanics is blunted

because of the increased LV sphericity, which leads to widening of the apex and loss of the oblique architecture of the apical fibres. Actually, for these subjects, the peak rotational rate is found to be equal to 70 °/s (Figure 3.17), while healthy patients exhibit a value of about 125 °/s (Figure 3.16b).
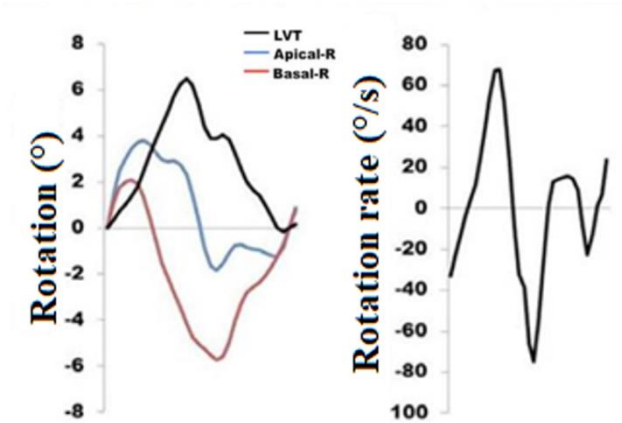
Figure 3.17: In HFREF, all rotational values were decreased, signifying exhaustion of LV twist reserve mechanisms, contributing to the reduced EF. Blue lines represent apical rotation, red lines represent basal rotation, while the black lines refer to the difference between basal and apical rotation.

$\sigma(z)$ is the same linking function previously described for the contraction/dilation movement, while the constant 0.0174 is the converting factor to transform °/s to rad/s.

Now, $u_\perp$ and $u\|$, which define nodal translation and rotation, respectively, ought to be projected on the three directions of the Cartesian reference system. In doing so, three values of displacement , u_x, u_y and u_z were determined, to be assigned to the grid point for mesh motion. $u_\perp$ and $u\|$ spacial projection were identified by means of ϑ and φ angles (Figure 3.18), defined as follows (eq. 9):

$$\vartheta = arctg \; \frac{z - z_p}{\sqrt{x^2 + y^2}} \qquad \varphi = arctg \; \frac{y}{x} \qquad (9)$$

where x, y and z are the spatial coordinates of each node in the grid, while z_p is a linear function of the z coordinate, whose mathematical expression is (eq.10):

$$z_p = 0{,}8535z \qquad (10)$$

(a)   (b)
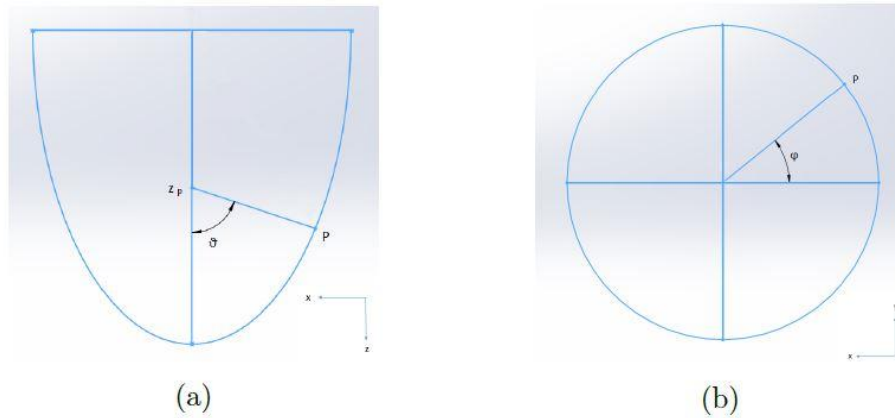
Figure 3.18: Definition of the angles ϑ (a) and φ (b).

This function assigned, to each node, the z coordinate of the intersection point between the z axis and the perpendicular to the ventricular semi-ellipsoid, passing through that specific node.

Given the definitions of ϑ and φ, the three displacements u_x, u_y and u_z are (eqs. 11-13):

$$u_x = -u_\perp \; cos \, \vartheta \; cos \, \varphi - u_\parallel \; sin \, \varphi \qquad (11)$$

$$u_y = -u_\perp \; cos \, \vartheta \; sin \, \varphi + u_\parallel \; cos \, \varphi \qquad (12)$$

$$u_z = -u_\perp \; sin \, \vartheta \qquad (13)$$

The so far described UDF worked only on ventricular geometries whose reference frame had a z axis pointing towards the ventricular apex. So, in order to apply the implemented function to the considered pathological patient-specific LV geometry, whose Cartesian system is shown in Figure 3.19, it was necessary to transform the absolute nodal coordinates of the current geometry to local ones, that is in a local reference frame with the z axis towards the apex and centred in the mitral valve.
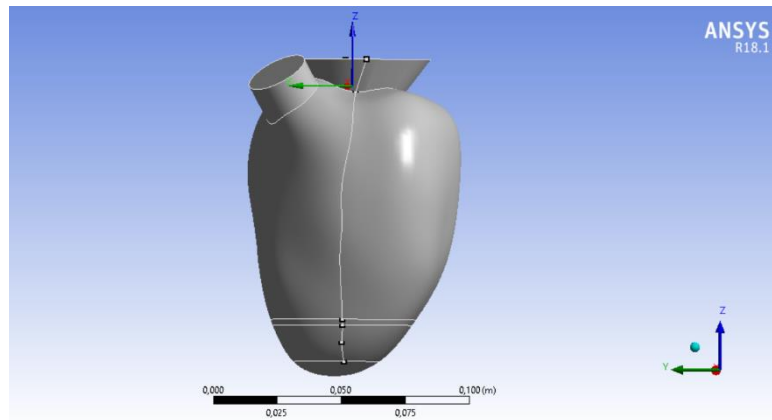
Figure 3.19: Cartesian system (known also as absolute or global) of the pathological patient-specific LV. As it can be noticed, the z axis is not pointing towards the apex.

The transformation of the reference system was obtained through three rotations and a final shift, thus requiring the definition of 3 rotational matrices.

In particular, global Cartesian coordinates of the apical node (x_{apex}, y_{apex} and z_{apex}) were identified. Then, the passage of the local x axis through this point was imposed through two subsequent rotations of the global reference frame by α and β angles.

These angles are defined as follows (eqs. 14-15):

$$\beta = arcsin \frac{z_{apex}}{\sqrt{x_{apex}^2 + y_{apex}^2 + z_{apex}^2}} \qquad (14)$$

70

$$
\alpha = \begin{cases} \arccos\dfrac{x_{apex}}{\cos\beta\;\sqrt{x_{apex}^2 + y_{apex}^2 + z_{apex}^2}} & if\; y_{apex} > 0 \\[4mm] 2\pi - \arccos\dfrac{x_{apex}}{\cos\beta\;\sqrt{x_{apex}^2 + y_{apex}^2 + z_{apex}^2}} & if\; y_{apex} < 0 \end{cases} \tag{15}
$$

Furthermore, an additional rotation of 90° was applied in order to make the local z axis to pass through the apex. Finally, a shift of the local reference frame origin was performed, so that the z coordinates of the nodes belonging to the LV moving portion could start from $z_{local} = 0$.

Summarizing, the global nodal coordinates were transformed in local ones thanks to the following operations (eq.16):

$$
\begin{bmatrix} x_{local} \\ y_{local} \\ z_{local} \end{bmatrix} = [Rot_{90°}]\,[Rot_\beta]\,[Rot_\alpha] \begin{bmatrix} x_{global} \\ y_{global} \\ z_{global} \end{bmatrix} + \begin{bmatrix} 0 \\ 0 \\ z_{shift} \end{bmatrix} \tag{16}
$$

where $Rot_{90°}$, Rot_α and Rot_β are the three rotational matrices, formalized as follows (eqs. 17-19):

$$
[Rot_\alpha] = \begin{bmatrix} \cos\alpha & \sin\alpha & 0 \\ -\sin\alpha & \cos\alpha & 0 \\ 0 & 0 & 1 \end{bmatrix} \tag{17} \qquad [Rot_\beta] = \begin{bmatrix} \cos\beta & 0 & \sin\beta \\ 0 & 1 & 0 \\ -\sin\beta & 0 & \cos\beta \end{bmatrix} \tag{18}
$$

$$
[Rot_{90°}] = \begin{bmatrix} \cos 90° & 0 & -\sin 90° \\ 0 & 1 & 0 \\ \sin 90° & 0 & \cos 90° \end{bmatrix} \tag{19}
$$

Once the computation of the displacements was performed in the local reference system, the inverses of the rotational matrices could be used to re-express the motion vectors in the global reference frame, making possible to update the global nodal coordinates at each time step. The result of the mesh motion is visible in Figure 3.20, where the superimposition of the end-systolic and end-diastolic configurations is reported, for the *pre-implant* model (image provided for a EF of 15%).
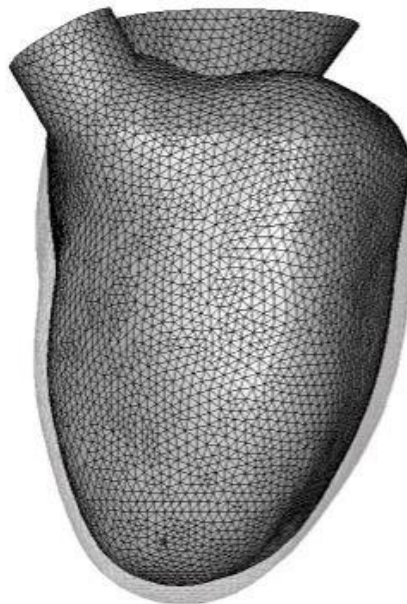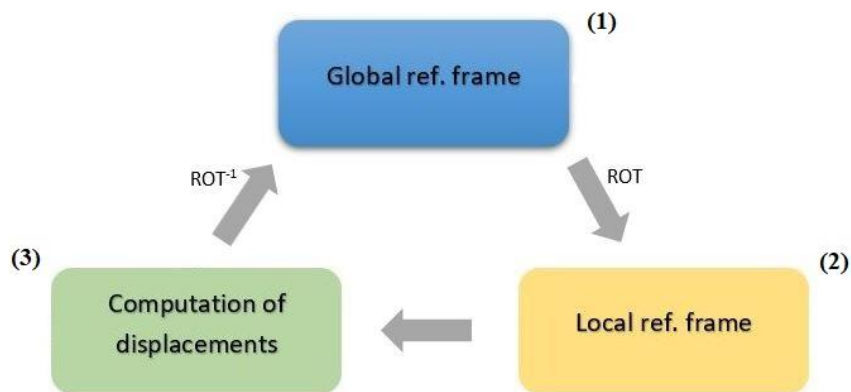
Figure 3.20: Superimposition of the end-systolic and end-diastolic configurations for the patient-specific model *pre implant;* image provided for a EF of 15%.

3.3.2. Left Ventricle Wall Motion: *Post - Implant*

For what concerns the *post* LVAD-implant models, two new UDFs were developed to also account for the cannula motion. Again, since it was necessary to refer to a local reference frame whose z axis points towards the ventricular apex, the absolute nodal coordinates (reference system shown in Figure 3.21) were transformed into local ones through the three rotational matrices, as previously described for the *pre-implant* model (§ 3.3.1).
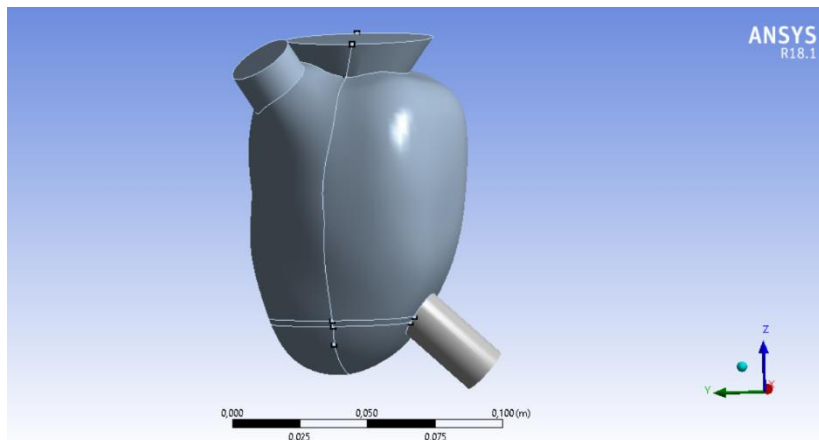
Figure 3.21: Cartesian system (known also as absolute or global) of the pathological patient-specific LV, *post implant* configuration. As it can be noticed, the z axis is not pointing towards the apex.

Since we assumed that the cannula only translates in the z direction, to avoid unwanted deformations of the cannula, the portion of the LV wall in immediate contact should move in the same way. Hence, the LV was subdivided in three zones: *i)* the valvular plane, standing still, *ii)* the central region, whose nodes translate and rotate, and *iii)* the apical region, only translating along the z-axis, as the inflow cannula (Figure 3.22).
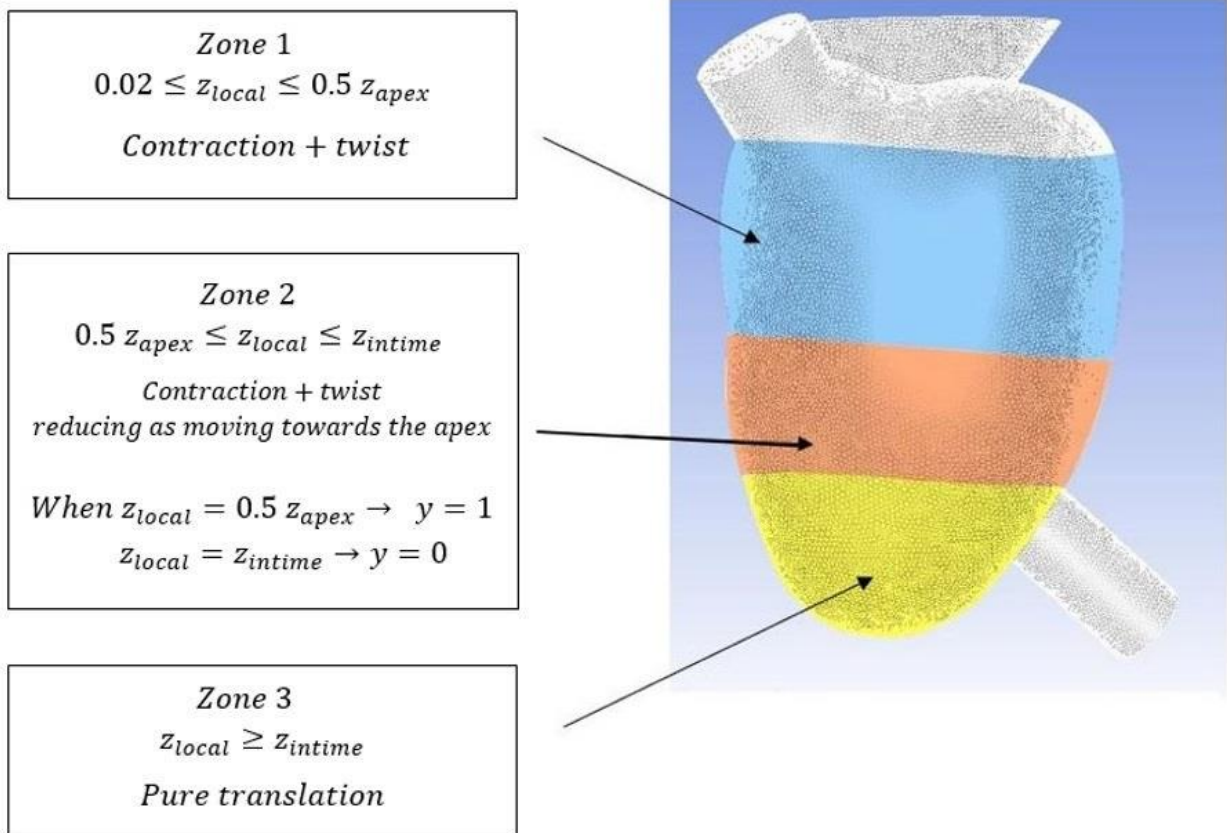
Figure 3.22: Ventricular motion zones: extension and characteristics.

Given the fact that the apex did not contract in the x and y directions, it was necessary to define a linking function y, a parabolic profile joining the different displacement functions applied along the ventricular wall, in order to obtain a smooth deformation of the LV grid. To practically identify the three zones of the ventricle, two functions were introduced: z_{apex} and z_{intime}. The first one stored a combination of the coordinates of the apical node, but, since the ventricle moved throughout the cardiac cycle, an algorithm to find out the updated apical coordinates at each time step was implemented.

```
/* cycle z apex */
conta=0;
begin_f_loop(f,tf)
{
if(conta==0)
        {
        F_CENTROID(j,f,tf);
        zapex= -0.0213*j[0] +0.0606*j[1] -0.9979*j[2]-0.0177;
        conta++;
        }
else
        {
        F_CENTROID(j,f,tf);
        if((-0.0213*j[0] +0.0606*j[1] -0.9979*j[2]-0.0177)>zapex)
        {
        zapex= -0.0213*j[0] +0.0606*j[1] -0.9979*j[2]-0.0177;
        }
        }
}
end_f_loop(f,tf)
```

F_CENTROID (j, f, tf) is a Fluent macro that, within each loop, returns the position of the face centroid (stored in the array *j*) for the face with index *f*, that is on the thread pointed to by *tf*. At each time step, this code assigned to z_{apex} the combination of coordinates with the maximum value.

Instead, the function z_{intime} gave the temporal variation of the z coordinate of the node chosen as contact point between the cannula and the ventricular wall (i.e. the farthest node from the LV apex, between the ones at the cannula-LV wall interface).

The definition of z_{intime} was essential in order to obtain a synchronous movement between the cannula and the LV. In the UDF code, the z coordinate of the chosen contact node was updated at each time step, summing to its current value the displacement $u_z = -u_{\perp} \sin \vartheta$.

The discrete values of z obtained through this procedure (one for each time step) were then interpolated through the MATLAB function *polyfit-polyval*, with a 15th order polynomial function, storing the temporal trend of the z coordinate of the contact point between the cannula and the LV wall.

So, given the definition of z_{apex} and z_{intime}, the mathematical expression for the previously mentioned connecting function y is the following (eq. 20):

$$y(z_{local}) = \sqrt{\frac{1}{a}\left(z_{local} + \frac{b^2}{4a} - c\right)} - \frac{b}{2a} \qquad (20)$$

where:

$$a = \frac{b^2}{8c} \qquad b = 8c - \sqrt{80c^2 - 8cz_{apex}} \qquad c = z_{intime}.$$

More in detail, displacement $u_\perp$ and the functions z_p and $\delta(z)$, when referred to the purely translational ventricular region (Figure 3.22, *Zone 3*), were expressed in terms of z_{intime}, while ϑ was function of z_{intime}, x_{ref} and y_{ref}, being them the x and y coordinates of the contact point cannula/ventricle.

Zone 1 (Figure 3.22) rotated and contracted as previously described for the *pre-implant* geometry (§ 3.3.1): here the applied displacements depended, together with time, on the current z coordinate.

Zones 1 and *3* were linked by *Zone 2* (Figure 3.22) where the parabolic function y (the one defined above) determined the nodal motion such that a smooth passage from the twist and contraction to the mere contraction was guaranteed.

For the sake of simplicity, in this section, only images referring to *post-implant* model A were reported, but, clearly, the cannula wall motion was implemented in the same way for *post-implant* model B, too.

The result of the mesh motion is visible in Figure 3.23, where the superimposition of the end-systolic and end-diastolic configurations is reported, for the *post-implant* models (images provided for a EF of 15%).
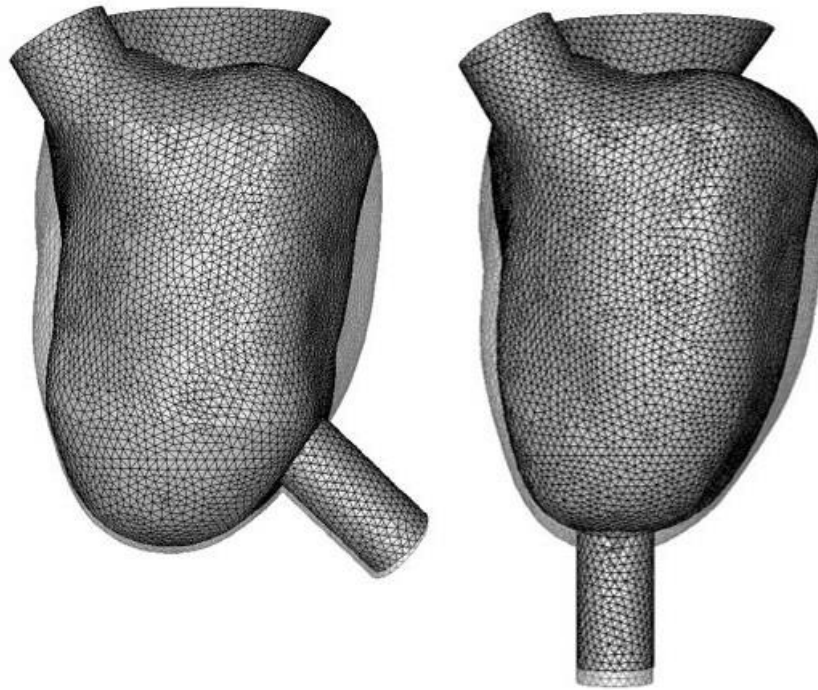
Figure 3.23: Superimposition of the end-systolic and end-diastolic configurations for the patient-specific models *post-implant A* (left) and *B* (right); images provided for a EF of 15%.

3.4. Numerical Inertia

At the beginning of each simulation, the fluid in the LV was at rest so that, in order to reach a periodic solution and a fully developed flow, the computation of several cardiac cycles was required.

In this study the repeatability of the solution at the third cycle was proven, both qualitatively and quantitatively.

Qualitative comparison of velocity magnitude streamlines, evaluated at the same time step, between five subsequent cardiac cycles, revealed that the flow patterns between the third and fourth cycle were roughly identical (Figure 3.24). Here, we replicated the approach described by Doost *et al.* in [55].

In all cycles, velocity streamlines were evaluated on a plane defined with three specific points: *i)* the ventricular apex, *ii)* the ventricle-aorta contact point, and *iii)* the centre of the mitral orifice. Furthermore, the in-plane averaged velocity magnitude difference, between the third and fourth cardiac cycle, was proven to be less than 2%. Consequently, taken the qualitative and quantitative comparisons of the flow development in five sequent cycles, the flow field could be assumed not to change significantly, with an expected minor variation of the hemodynamic parameters, after the third cycle.
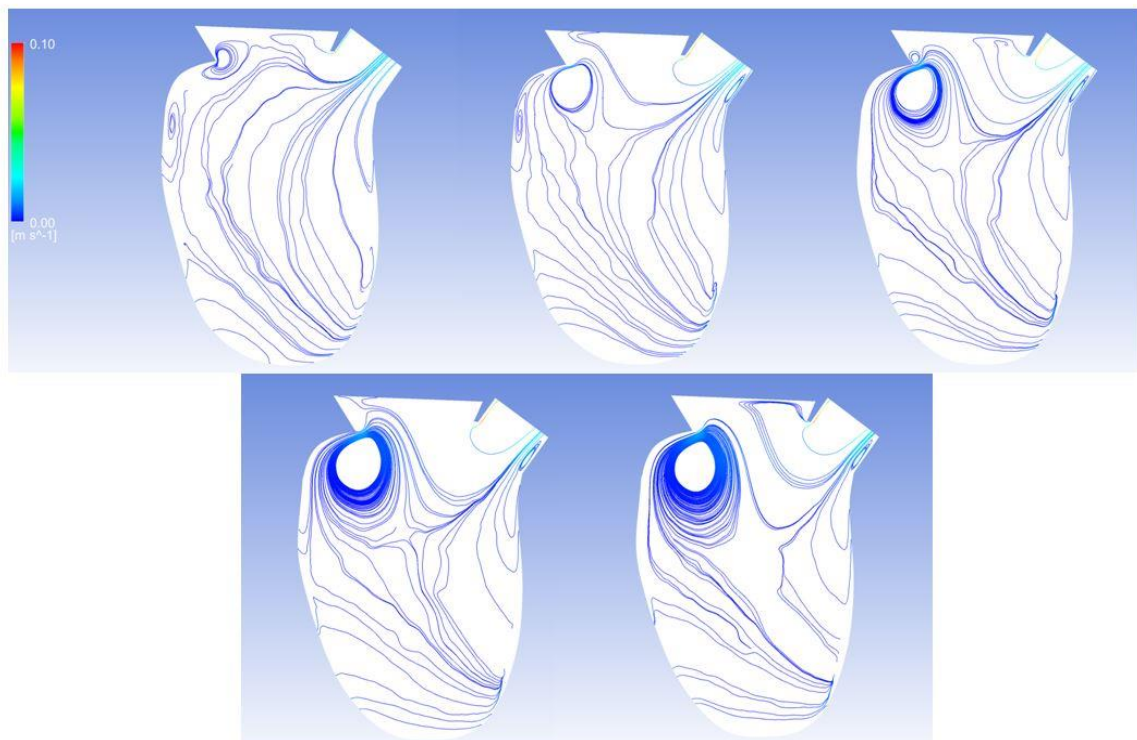
Figure 3.24: End systolic in-plane flow patterns in five subsequent cardiac cycles. Top half, from left to right: Cycles 1, 2 and 3. Bottom half, from left to right: Cycles 4 and 5.

3.5. Numerical Settings

The fluid dynamic simulations (3D, transient) were performed exploiting the software ANSYS Fluent 18.1. Blood was modelled as a Newtonian fluid, with viscosity μ=0.003 Pa·s and density ρ=1060 kg/m^3.

For what concerns the *pre-implant* model, the UDF for the grid motion was compiled, loaded and assigned to the named selection *ventricle* in the enabled *Dynamic Mesh* dialog box. As mesh methods, *Spring Smoothing* and *Local Cell*, *Local Face* and *Region Face Remeshing* were selected.

When dealing with *post-implant* geometries, cannula and ventricle grid motions were recalled thanks to the command DEFINE GRID MOTION in the same UDF text file.
Ventricle mesh motion was assigned to the named selection *ventricle*, while the cannula mesh motion was applied to the named selections *velocity_inlet*, *cannula, cannula2* and *cannula2_shadow*. This way, all the cannula components moved together.
The zone *cannula2_shadow* appeared automatically in ANSYS Fluent 18.1 when the *cannula2* boundary condition type was switched from *interior* to *wall*. It represented the portion of the cannula inside the ventricle, in direct contact with the LV fluid domain.

The Pressure-Velocity Coupling SIMPLE algorithm was chosen as the numerical scheme, with a 2nd order upwind spatial discretization and a 1st order implicit transient formulation, set as default. For what concerns the under-relaxation factors, the following values were set: 0.3 for pressure and 0.7 for momentum. To ensure solution convergence, the residuals for continuity and x, y, z - velocities were set up to 10^{-5}. Calculations were run with a time step equal to 1 ms and 150 iterations/time step. The number of time steps depended on the phase of the cardiac cycle being simulated: 282 time steps for systole and 419 time steps for diastole.

3.6. Simulation Settings

In this study, three simulations sets were designed to characterize the mutual interactions between residual contractility in a failing ventricle, degree of LVAD support (i.e. LVAD flow rate provided to the patient) and LVAD inflow cannula positioning, because these factors were hypothesized to significantly contribute to alter intraventricular flow dynamics and enhance the LV thrombogenic potential.

The implementation details of each set are listed below.
All simulations started with the systolic phase, followed by the diastole.

3.6.1. Set 1: *Pre – Implant* Model

This set consists of three simulations. The fluid dynamic domain is the pathologically dilated patient-specific LV.

Transient CFD simulations of the whole cardiac cycle were carried out, considering three values of residual EF% (15% - 10% - 5%), corresponding to increasing levels of cardiac impairment, that is from moderate to severe LV HF.

Through this set of simulations, the role of LV residual contractility as a possible thrombogenic factor was explored, by analyzing blood velocity patterns, blood stasis and, associated WSS trends in the apical region. Furthermore, results from these simulations were used as basis for comparison with corresponding *post* inflow cannula implantation data.

Simulations details are provided in Table 3.3, were systolic ejection volumes, cardiac outputs, and systolic/diastolic values of k are reported, for each of the three simulations.
A cardiac cycle lasted 0.701 s, while systole and diastole were 0.282 s and 0.419 s long, respectively.

Residual EF %	5.00%	10.00%	15.00%
Stroke volume [ml]	14	28	42
Native CO [L/min]	1.20	2.40	3.60
K Systole	18.4	18.4	18.4
K Diastole	17.8	17.75	17.65

Table 3.3: Stroke volume, Native CO, and k values for 5%,10%, and 15% EF.

3.6.2. Set 2: *Post - Implant* Model A

Set 2 consists of a matrix of 8 test conditions, obtained combining 4 values of residual EF% (0 - 5 - 10 - 15%) with 7 levels of support (LVAD flow rates).

To each one of the residual EF% corresponded a native CO, expressed in L/min.

Pairs of variables (LVAD CO, LV EF%) were identified having as a target a total CO, given by the sum of native CO and LVAD flow rate, equal to 5 L/min.

This way, the interplay between myocardial residual contractility and LVAD flow rate was evaluated.

The CFD model is based on the same pathologically dilated patient-specific LV of Set 1, *post* LVAD implantation. The patient-specific inflow cannula positioning was derived from imaging techniques and reconstruction process described in section §3.1.1.

Simulations details are provided in Table 3.4.

	Residual EF %			
VAD CO [L/min]	0.00%	5.00%	10.00%	15.00%
2.20			CO$_{TOT}$ = 4.60 L/min ΔVd = 38.34 ml K Systole =28.9 K Diastole = 28.55	CO$_{TOT}$ = 5.80 L/min ΔVd = 52.34 ml K Systole =28.8 K Diastole = 28.5
2.70			CO$_{TOT}$ = 5.10 L/min ΔVd = 40.69 ml K Systole =28.9 K Diastole = 28.5	
3.00			CO$_{TOT}$ = 5.40 L/min ΔVd = 42.10 ml K Systole =28.9 K Diastole = 28.5	
3.50		CO$_{TOT}$ = 4.70 L/min ΔVd = 30.45 ml K Systole =29 K Diastole = 28.6		
3.80		CO$_{TOT}$ = 5.00 L/min ΔVd = 31.86 ml K Systole =29 K Diastole = 28.6		
4.10		CO$_{TOT}$ = 5.30 L/min ΔVd = 33.27 ml K Systole =29 K Diastole = 28.6		
5.00	CO$_{TOT}$ = 5.00 L/min ΔVd = 23.5 ml K Systole =29.1 K Diastole = 28.6			

Table 3.4: Total flow rate [L/min] (CO+LVAD), ΔVd applied volume variation [ml] in systole and diastole (i.e. stroke volume), k values, for all the simulations.

3.6.3. Set 3: *Post - Implant* Model B

This set consists of 2 test conditions, selected from Set 2 simulation matrix.

These 2 configurations were chosen considering the total cardiac output (CO) provided to the patient, that is the sum of native residual CO and LVAD flow rate. Total CO was assumed equal to 5 L/min, a condition mimicking the average cardiac output at rest, so as to refer to real clinical data.

In this set of simulations, cannula position was varied: it was modelled so that the inflow cannula longitudinal axis intersects the LV apex and the centre of the mitral valve orifice.

The aim was to quantify the impact of cannula position on LV thrombogenicity so to identify the most hemodynamically favourable LVAD implantation configuration.

Simulations details are listed in Table 3.5.

		Residual EF	
		5.00%	**10.00%**
VAD CO [L/min]	**2.70**		CO_{TOT} = 5.10 L/min ΔVd = 40.69 ml K Systole =22.2 K Diastole = 21.75
	3.80	CO_{TOT} = 5.00 L/min ΔVd = 31.86 ml K Systole =22.4 K Diastole = 21.95	

Table 3.5: Total flow rate [L/min] (CO+LVAD), ΔVd applied volume variation [ml] in systole and diastole (i.e. stroke volume), k values, for all the simulations.

3.6.4. Mass Conservation

To guarantee mass conservation throughout each simulation, the volume variations listed in Tables 3.3-3.5 were imposed to the fluid domain, through the mesh motion.

For what concerns the simulation Set 1 (*pre- implant* model), the calculated stroke volumes were only related to the ventricular residual contractility. During a cardiac cycle, an equal amount of blood was entering and exiting respectively through the mitral valve and the aortic valve.

For each simulation belonging to Set 2 and 3 (*post-implant* models), the systolic stroke volume was set equal to the blood simultaneously exiting from the cannula and the aorta, while the LV volume variation during diastole was computed as difference between the entering blood quantity from the mitral orifice and the exiting blood from the pump.

In other words, the volume variations imposed in the *post-implant* models were related both to the LVAD suction action and to the LV contraction.

3.7. Boundary Conditions

Set 1: Pre - Implant Model

For the systolic phase simulation, the following boundary conditions were imposed:

- *Moving wall* for the named selection *ventricle* (motion relative to adjacent zone given by components).
- *Stationary wall* for the named selections *mitral_valve, aorta, atrium*.
- *Pressure outlet*, with a pressure value equal to 0 Pa, normal to boundary, for the named selection *aortic_valve*.

For the diastolic phase simulation, the following boundary conditions were imposed:

- *Moving wall* for the named selection *ventricle* (motion relative to adjacent zone given by components).
- *Stationary wall* for the named selections *aortic_valve, aorta, atrium*.
- *Pressure inlet*, with a pressure value equal to 0 Pa, normal to boundary, for the named selection *mitral_valve*.

These boundary conditions were set equal in every simulation belonging to Set 1.

A pressure of 0 Pa was chosen as boundary conditions for both the *aortic_valve* and the *mitral_valve*, in systole and diastole respectively, since in our model the LV hemodynamics was strongly influenced by two main factors, the EF% and the LVAD flow rate, and, to a lesser extent, by the systemic circulation. Furthermore, this boundary condition was set equal in all the simulations considered in this study, so that the same bias was introduced in the results.

Set 2: Post – Implant Model A

For the systolic phase simulation, the following boundary conditions were imposed:

- *Moving wall* for the named selections *ventricle, cannula, cannula2, cannula2_shadow,* with motion relative to adjacent zone given by components set as option.
  The zone *cannula2_shadow* appeared automatically in ANSYS Fluent 18.1 when the boundary condition type was switched from *interior* to *wall*. It represented the portion of the cannula inside the ventricle, in direct contact with the fluid domain.
- *Stationary wall* for the named selections *mitral_valve, aorta, atrium*.
- *Pressure outlet*, with a pressure value equal to 0 Pa, normal to boundary, for the named selection *aortic_valve*.
- For the named selection *velocity_inlet* the velocity specification method was set as velocity magnitude, normal to boundary, with different cannula suction velocities depending on the test conditions (Table 3.6). Since the LVAD is a continuous flow pump, the suction velocity for the cannula is constant in both phases of the cardiac cycle.

		Residual EF			
		0,00%	5,00%	10,00%	15,00%
	2,20			0,14409	0,14409
VAD CO [L/min]	2,70			0,17684	
	3,00			0,19649	
	3,50		0,22924		
	3,80		0,24888		
	4,10		0,26853		
	5,00	0,3275			

Table 3.6: Inflow cannula suction velocity [m/s] for all the simulations.

For the diastolic phase simulation, the imposed boundary conditions were the same ones used for the systolic phase, except for:

- *Stationary wall* for the named selection *aortic_valve.*
- *Pressure inlet,* with a pressure value equal to 0 Pa, normal to boundary, for the named selection *mitral_valve.*

Set 3: Post – Implant Model B

For the systolic phase simulation, the following boundary conditions were imposed:

- *Moving wall* for the named selections *ventricle, cannula, cannula2, cannula2_shadow,* with motion relative to adjacent zone given by components set as option.
- *Stationary wall* for the named selections *mitral_valve, aorta, atrium.*
- *Pressure outlet*, with a pressure value equal to 0 Pa, normal to boundary, for the named selection *aortic_valve.*
- For the named selection *velocity_inlet* the velocity specification method was set as velocity magnitude, normal to boundary, with different cannula suction velocities depending on the test conditions (Table 3.6). Since the LVAD is a continuous flow pump, the suction velocity for the cannula is constant in both phases of the cardiac cycle.

For the diastolic phase simulation, the imposed boundary conditions were the same ones used for the systolic phase, except for:

- *Stationary wall* for the named selection *aortic_valve.*
- *Pressure inlet,* with a pressure value equal to 0 Pa, normal to boundary, for the named selection *mitral_valve.*

3.8. Solution Data Export

In order to obtain a sufficiently large amount of data for post-processing purposes, all the simulations were run with an autosave set in the Calculation Activities task page. In particular, data files, and associated case files, were saved every 5 time steps, hence every 0.005 s, exporting, as data files quantities, static pressure, velocity magnitude, and vorticity magnitude. Furthermore, for each time step, the LV surface WSS data were automatically exported in ASCII files, containing WSS moduli and x, y, and z components.

3.8.1. Analysis of Vortex Dynamics

In this study, vortex dynamics was analyzed applying the Q-criterion. This method looks at the second invariant of the velocity gradient tensor, Q.

Q-criterion is a three-dimensional vortex identification method, developed by Hunt *et al.* [56], in 1988, which defines a vortex as a spatial region where (eq.1):

$$Q = \frac{1}{2}\left[|\Omega|^2 - |S|^2\right] > 0 \qquad (1)$$

i.e. where the Euclidean norm of the vorticity tensor dominates that of the rate of strain.

In (1), $S = \frac{1}{2}\left[\nabla v + (\nabla v)^T\right]$ is the rate-of-strain tensor, and $\Omega = \frac{1}{2}\left[\nabla v - (\nabla v)^T\right]$ is the vorticity tensor.

Hence, a vortex is defined as an area where Q > 0. Essentially, this means a vortex is a connected region of fluid where the asymmetric component of ∇v, that is the vorticity tensor, dominates over the symmetric one.

3.8.2. Extraction of Wall Shear Stress (WSS) Patterns

In the present study, the evaluation of wall shear stress on the apical portion of the ventricular wall was carried out since WSS is a mean to assess blood stasis.

Blood stasis and recirculation patterns in the LV chamber are recognized risk factors for intraventricular thrombosis and potential thromboembolic events, as they promote thrombosis through the accumulation of both activated and sensitized platelets, who may get trapped because of the LV limited washout and exposed to low dynamic shear stress for elongated durations, i.e., additional prothrombotic conditions.

The WSS were extracted considering a complete cardiac cycle in three pre-defined regions close to the LV apex. The WSS modulus and its three-dimensional components were recorded and stored in ASCII files at each time step (282 steps for systole and 419 for diastole) for the cell centre of each element on the ventricular wall.

Then, thanks to a MATLAB script, the data were processed in order to obtain the WSS trends in time averaged over each of the above mentioned regions. These regions (Figure 3.25) were identified in between two z coordinates, expressed as percentage of z_{apex}, as follows:

$$1^{st} \ Region \ for \qquad z > 0.99 \ z_{apex}$$

$$2^{nd} \ Region \ for \qquad 0.97 \ z_{apex} < z < 0.99 \ z_{apex}$$

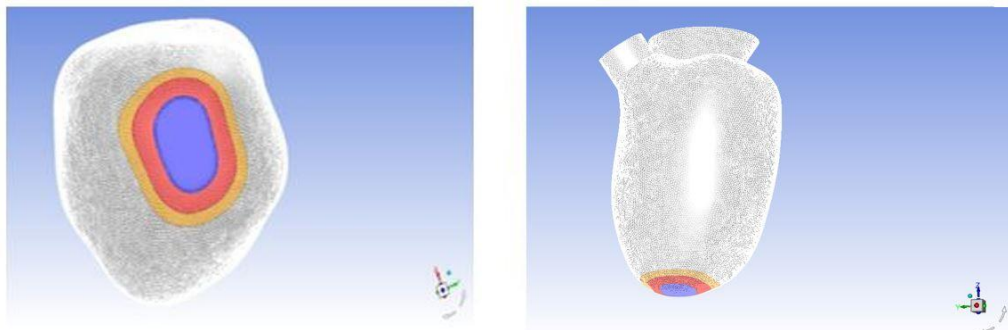$$3^{rd} \ Region \ for \qquad 0.95 \ z_{apex} < z < 0.97 \ z_{apex}$$

Figure 3.25: Apical regions, 1st region in blue, 2nd region in red, 3rd region in yellow. Left: bottom view. Right: lateral view.

The WSS were extracted in these three regions to comprehensively map blood behaviour close to the LV apex. Blood stasis was expected to become more evident as moving towards the LV apex.

3.9. Healthy LV Model

In this section, a brief description of the healthy patient-specific LV model, developed in a previous work [53], is reported. Results from the healthy LV model simulations were used as basis for comparison with *pre* and *post* inflow cannula implantation data.

The patient-specific LV geometry at end-systolic configuration, reconstructed from 3D-TT-ECHO images and acquired from a healthy volunteer, is shown in Figure 3.26a.

The healthy LV geometry was discretized with 445125 tetrahedral elements. The mesh is shown in Figure 3.26b. The result of the mesh motion is visible in Figure 3.26c, where the superimposition of the end-systolic and end-diastolic configurations is reported, assuming a stroke volume of 70 ml.

For the systolic phase simulation, the following boundary conditions were imposed:

- Moving wall (motion relative to adjacent zone given by components) for the named selection *ventricle*.
- The physiological temporal trend of aortic pressure was assigned to the named selection *aortic valve*.
- Stationary wall for the named selection *mitral valve*.

For the diastolic phase simulation, the following boundary conditions were imposed:

- Moving wall (motion relative to adjacent zone given by components) for the named selection *ventricle*.
- The physiological temporal trend of mitral pressure was assigned to the named selection *mitral valve*.
- Stationary wall for the named selection *aortic valve*.

The number of time steps (time step = 1ms) set for the simulation depended on the phase of the cardiac cycle: 282 for the systole and 419 for the diastole.
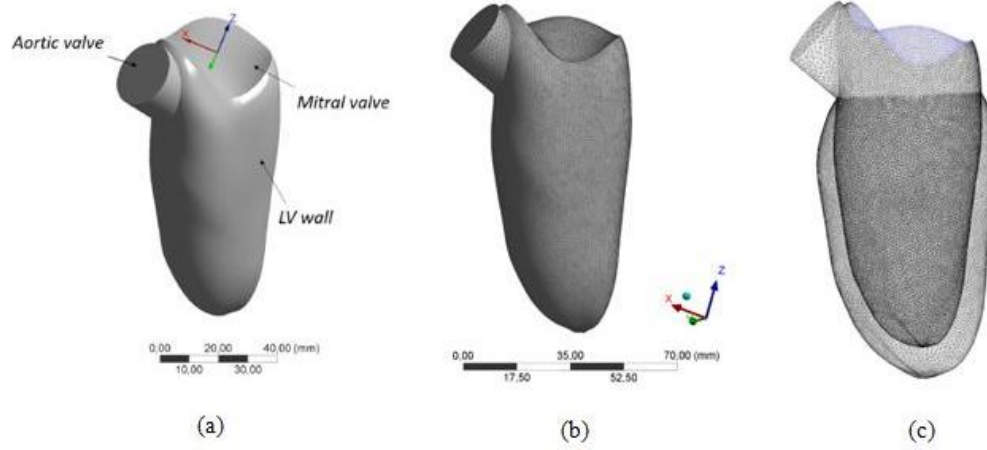

Figure 3.26: (a) Healthy patient-specific LV geometry at end-systolic configuration; (b) Mesh; (c) Superimposition of the end-systolic and end-diastolic configurations (stroke volume 70 ml).

4. Results and Discussion

In this chapter, the results obtained from the simulation sets (for details see § 3.6) are reported, pointing out ventricular hemodynamics fundamental characteristics and major features responsible of the thrombogenic potential of the different analyzed conditions.

Data are presented and discussed for each of the three simulation sets:

1. Set 1 *pre-implant*, LV residual contractility ranging from 5 to 15%;

2. Set 2 *post-implant A*, in which the effect of different values of LVAD flow rate and LV residual contractility was analyzed;

3. Set 3 *post-implant B*, in which the cannula position was varied with respect to the *post-implant* model A.

The characterization of the LV hemodynamics in the apical region was central in the present work, because this critical area is particularly prone to intraventricular thrombus formation (see § 1.2.2).

4.1. Set 1 *Pre - Implant* Model

This set consists of three CFD simulations of the whole cardiac cycle, each simulation associated with a value of residual EF% (15% - 10% - 5%), namely to increasing levels of cardiac impairment.

Patterns of vortex formation and evolution in the LV were analysed, since blood vorticity in the LV allows the smooth redirection of blood flow toward the LV outflow tract during systole, thus facilitating systolic blood ejection and ventricular washout.

Moreover, the role of LV residual contractility as a possible thrombogenic factor was explored, by analyzing blood velocity patterns, blood stasis, and associated WSS trends in the LV apical region.

4.1.1. Patterns of Vortex Formation and Evolution

A fundamental role in determining LV hemodynamics is played by vortexes, given that these structures are responsible for blood mixing, proper cardiac filling and emptying in the diastolic and systolic phases, respectively.

In this study, vortex dynamics was analyzed applying the Q-criterion. This method looks at the second invariant of the velocity gradient tensor, Q (see § 3.8.1).

In healthy LVs, a vortex forms when, during systole, the LV contracts and blood flow impacts the mitral valve, allowing for smooth redirection of flow toward the LV outflow tract (LVOT) during systole. Specifically, physiologic vortices within the LV increase cardiac efficiency by maintaining the momentum of inflowing blood during diastole, thereby facilitating the systolic ejection of blood into the LVOT [33]. In Figure 4.1, patterns of vortex formation and development are reported, comparing the case of a healthy LV with those associated with the different values of EF% that were simulated in the pathologic dilated HF LV(15%, 10% and 5%). The healthy patient-specific LV model was

developed in a previous work [53]; simulation results were extracted in order to allow for comparison with the examined pathological conditions.

For the healthy LV, during the systolic acceleration (Figure 4.1a), the contraction of the LV wall produces multiple vortical structures, distributed along the upper portion of the LV and the LVOT. In peak systole and in the deceleration phase (Figure 4.1b and c), vortexes are disrupted because of the ejection of blood through the aortic valve.

By contrast, results from simulation Set 1 show that, during systole, two vortexes develop close to the mitral valve; the smaller vortex remains coherent near the mitral orifice during systolic acceleration, peak and deceleration, while the main one slowly moves downwards, towards the centre of the LV and the LVOT (Figure 4.1).

In normal subjects, as the basal posterior LV wall contracts, the space beneath the mitral valve decreases and became so small as to make the vortex to be absorbed with the outflow stream [57]. On the other hand, in subjects with reduced EF%, enlargement of the LV results in postero-basal space large enough to form a vortex even in mid or late systolic phase (Figure 4.1b and c).

Furthermore, results show that the dimension and strength of formed vortexes depend on ventricular residual contractility, namely the higher the residual EF%, the larger and the more persistent the vortex. Patterns of vortex formation and evolution are similar for EF of 10% and 15%, while vortex structures are barely present in case of severe cardiac impairment (5% EF).

In Figure 4.2, velocity contours and vectors on a longitudinal plane across the mitral/aortic orifices and the LV apex are shown, in this way blood velocity magnitude values and vortexes directions of rotation can be identified. Data are presented for the healthy LV and the pathological LV with a residual EF of 15%. One pathological condition was chosen for the comparison given that vortex direction of rotation was found to be the same in each examined test condition; we refer to 15% EF since blood velocity values are more significant.
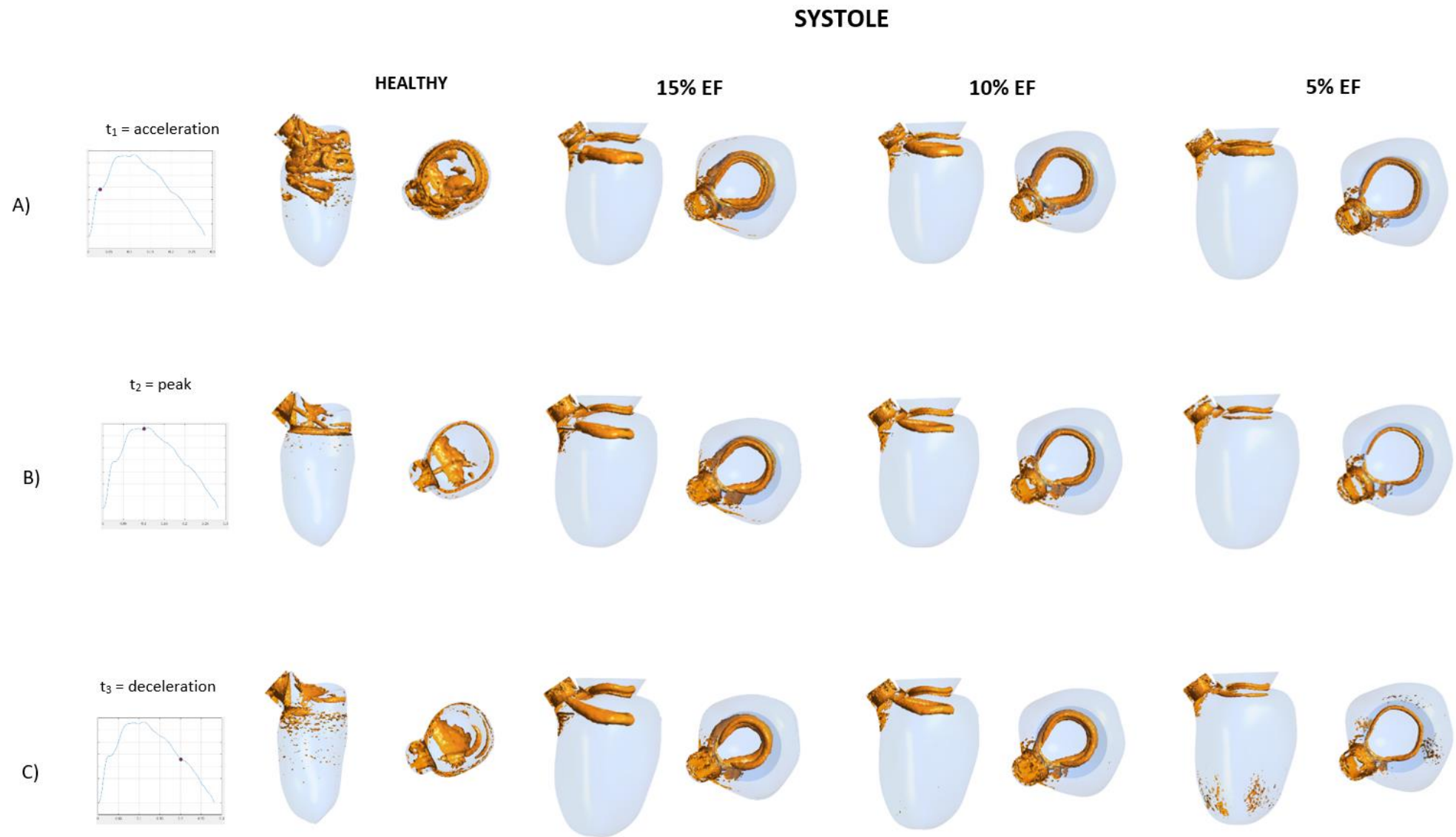
SYSTOLE

Figure 4.1: 3D Vortex field in systole obtained applying the Q-criterion; (A) systolic acceleration; (B) systolic peak; (C) systolic deceleration. Results are shown (from left to right) for the healthy LV model, for a residual EF of 15%, of 10% and of 5%.
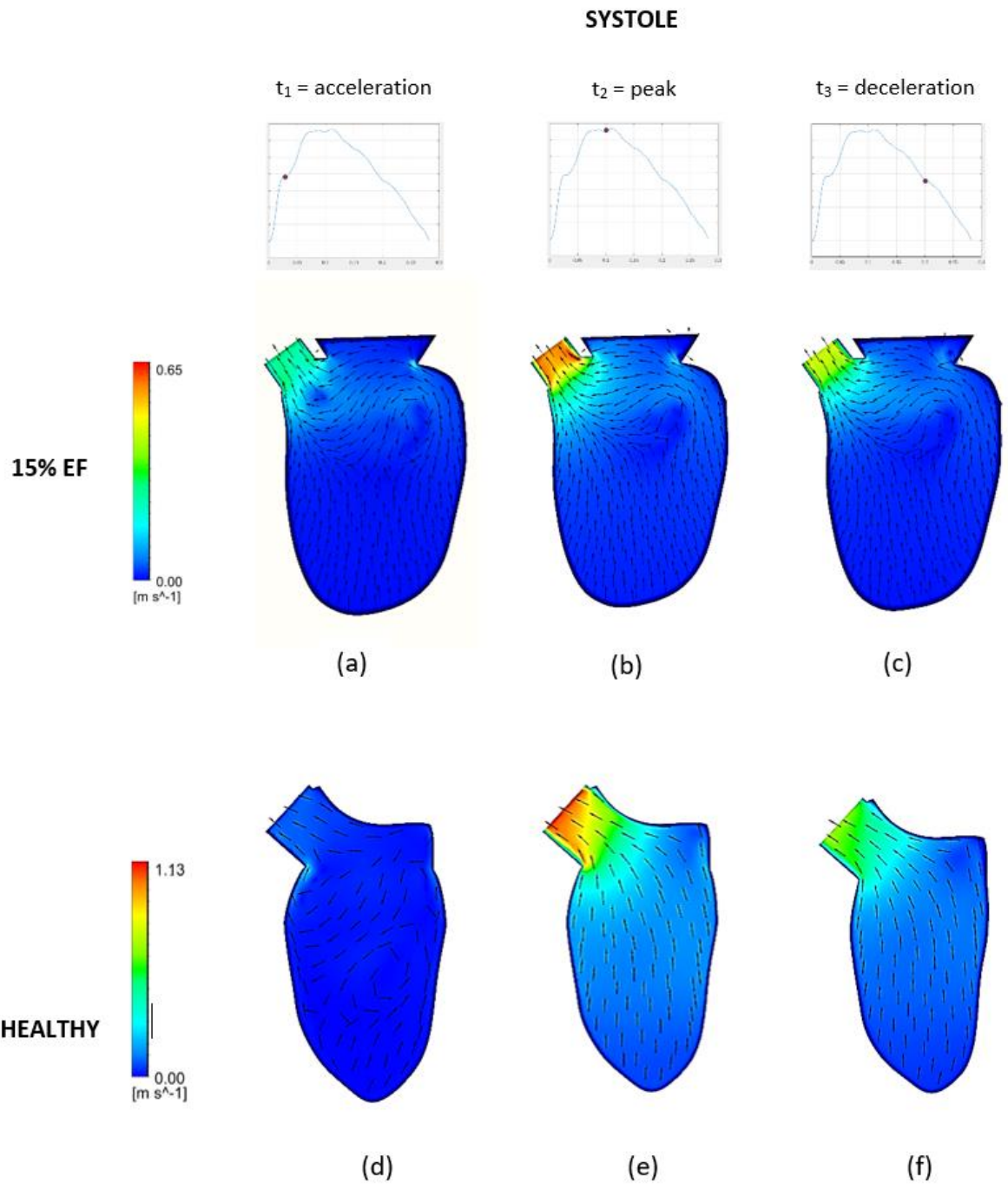
Figure 4.2: Systolic intraventricular flow, considering a residual EF of 15% (top), and for the healthy LV model (bottom). Vectors and velocity magnitude contours were obtained at systolic acceleration (a and d), systolic peak (b and e), and systolic deceleration (c and f).

96

Considering the healthy LV, in early systole (Figure 4.2d), two main asymmetrical vortexes are generated; the closest to the LV apex is counter clockwise while the second one, closer to the LVOT, moves clockwise. At peak and in late diastole, blood flows towards the aortic valve, and no vortexes are generated (Figure 4.2e and f).

On the other hand, considering a dilated LV with residual EF of 15%, during the systolic phase, a clockwise vortex is formed due to the contact between the blood stream and the LV wall, redirecting the fluid towards the LVOT and the aortic valve, coherently with literature data (Figure 4.2b).

Tang *et al.* [33], analyzed the hemodynamics in a pathologic DCM LV by using echocardiographic particle image velocimetry (E-PIV). In the systolic phase, the clockwise vortex occurring at the centre of the LV was proven to move toward the LVOT. In addition, during the rapid blood ejection phase, all vortices decreased; only the clockwise vortex close to the LVOT converted into a laminar flow for blood circulation (Figure 4.3, panels E,F). Small vortices still existed under the mitral valve leaflets.
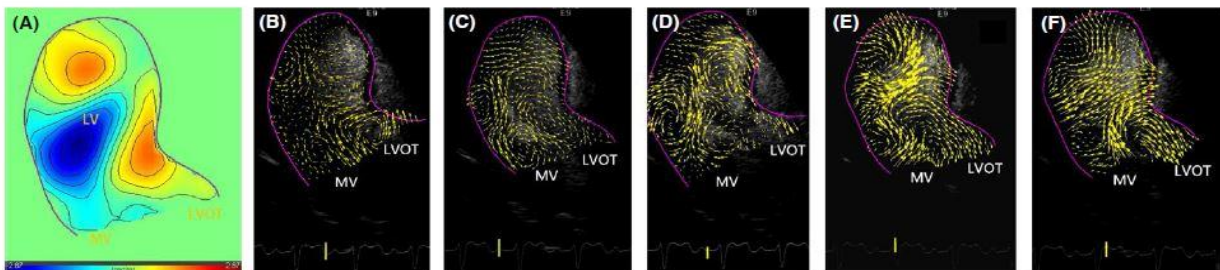

Figure 4.3: General flow patterns of the LV in patients with DCM. B was taken in the rapid filling period, C was taken in the reduced filling period, D was taken in the isovolumetric contraction period, and E and F were taken during the ejection period

For the healthy model, throughout the diastolic phase, vortices number and dimensions increase, with a unique prevalent vortex arisen beneath the mitral valve evolving in a chaotic distribution of multiple vortexes close to the LVOT (Figure 4.4).

For what concerns the pathological scenarios, diastolic vortexes (Figure 4.4) are localized just below the mitral valve and hardly propagate towards the apical region of the LV,

because of limited wall contractility and pathological dilation, increasing the risk for blood stasis and the potential for thrombus formation.

When DCM occurs, for EF of 15 and 10%, in early diastole and at the E wave (Figure 4.4a and b), the formed 3D vortex ring remains rather compact in the upper part of the LV.

In late diastole (Figure 4.4c and d), two compact rings develop in the centre of the LV inducing only local circulation of blood. These vortexes are of greater extent when EF is equal to 15%. In case of severe dilation (5% EF), the described pattern of vortex formation and evolution is barely present.

In Figure 4.5, velocity contours and vectors on a longitudinal plane across the mitral/aortic orifices and the LV apex, are shown, for both the healthy and 15% residual EF conditions. As it can be noticed comparing the ventricular flow fields, with LV dilation and abnormal myocardial contraction in DCM, aberrant fluid mechanics (many vortices with different directions of rotation) appear in the LV, which cause the flow to be disorderly, and this redirects the blood flow from the LV base toward the LV posterior wall, the LV apex, and the LVOT. This effect reduces the blood flow for systolic ejection in the LVOT and increases the residual blood flow in the LV cavity, as reported by [33].

In early diastole and at the peak of the E-wave, indeed, two vortices are formed around the bilateral side of the transmitral inflow (Figure 4.5a and b), while in the healthy LV, blood flows undisturbed from the MV to the apex (Figure 4.5e-h).

Furthermore, the reduced cardiac function (15% EF) weakens the diastolic mitral jet (Figure 4.5c and d), which penetrates less deeply into the wider LV, if compared to the healthy condition, and is unable to support flow redirection towards the outflow. The diastolic vortex dynamics here described is in good agreement with data presented in the work of Mangual *et al.* [34].
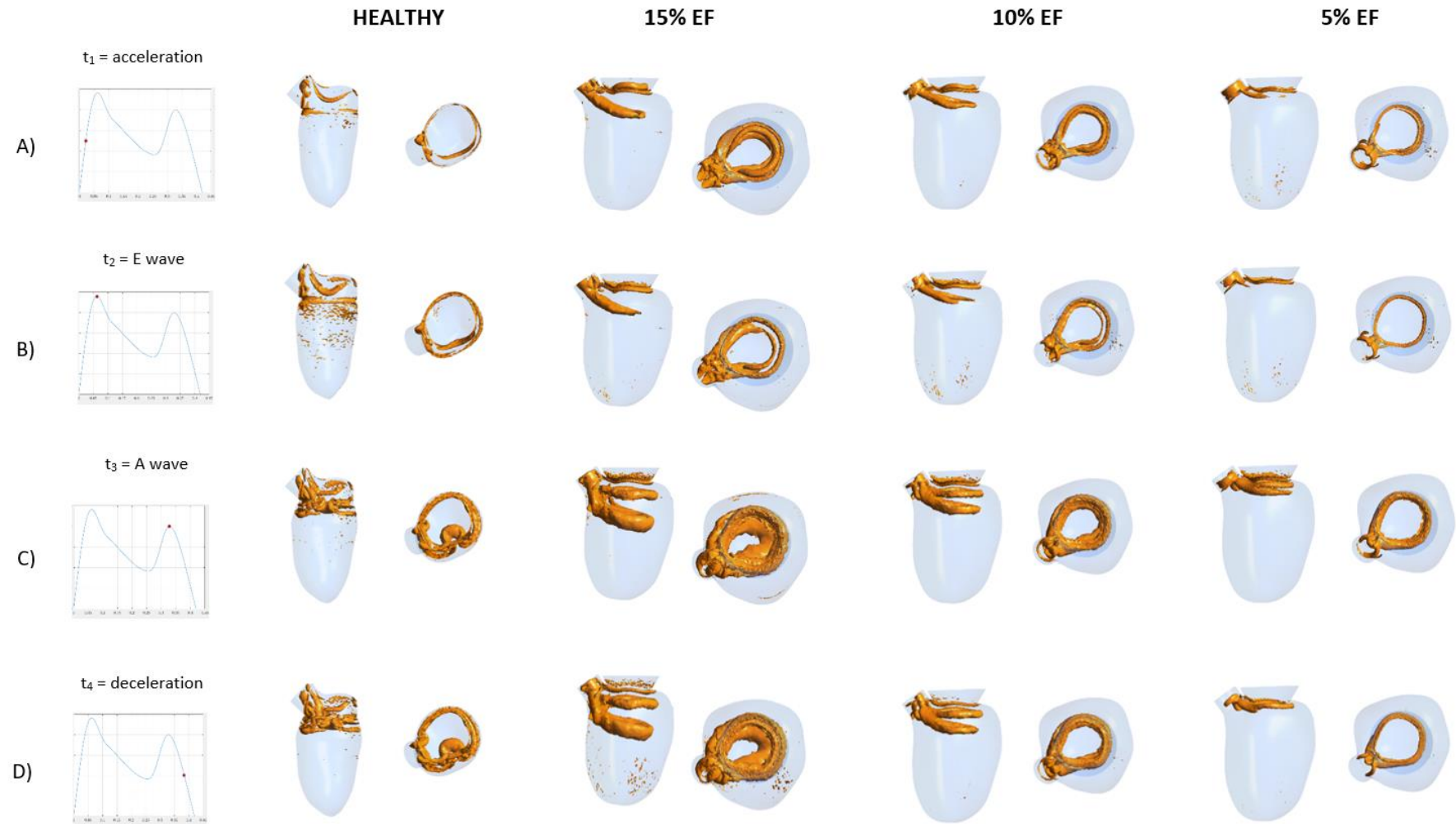
Figure 4.4: 3D Vortex field in diastole obtained applying the Q-criterion; (A) diastolic acceleration; (B) E wave; (C) A wave; (D) diastolic deceleration. Results are shown (from left to right) for the healthy LV model, for a residual EF of 15%, of 10% and of 5%.

Figure 4.5: Diastolic intraventricular flow, considering a residual EF of 15% (top), and for the healthy LV model (bottom).Vectors and velocity magnitude contours were obtained at diastolic acceleration (a and e), E wave (b and f), A wave (c and g), and diastolic deceleration (d and h).

4.1.2. Thrombogenic Potential: the Effect of LV Residual Contractility
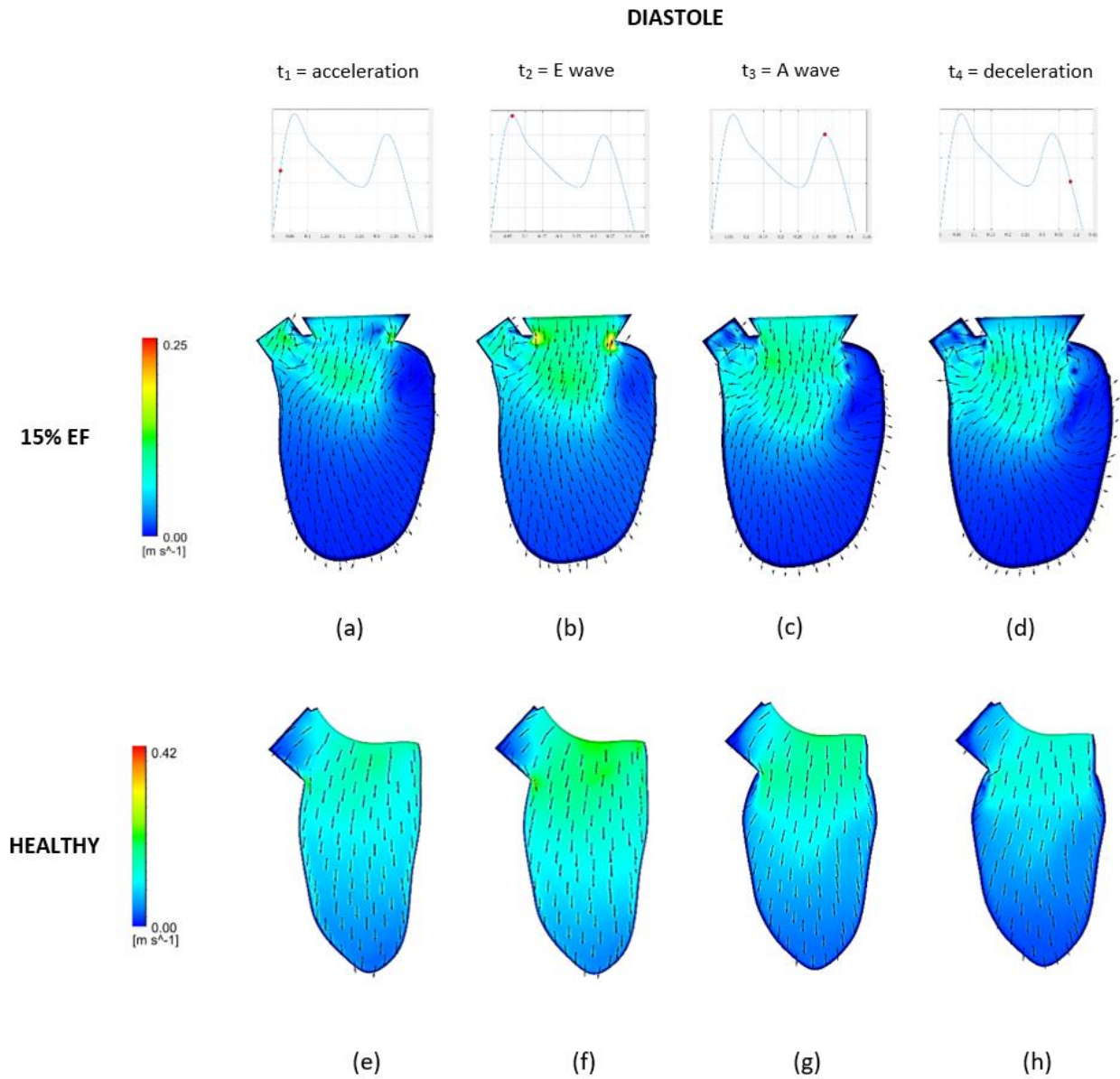
In the pathological dilated LV with low residual contractility, the apical region of the ventricular chamber is considered a critical area due to potential proneness to intraventricular thrombus formation, because of blood stasis and blood recirculation patterns [32].

In the present study, the evaluation of wall shear stress in the apical portion of the ventricular wall was carried as a mean to assess blood stasis.

The WSS were extracted considering a complete cardiac cycle in three pre-defined regions close to the ventricular apex (Figure 4.6).
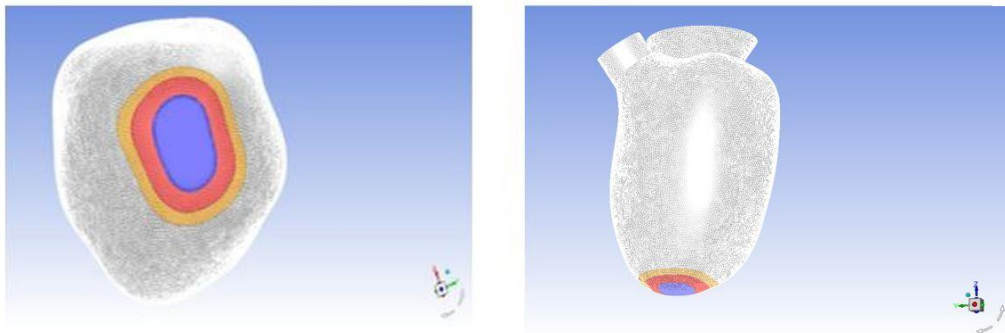
Figure 4.6: Apical regions, 1st region in blue, 2nd region in red, 3rd region in yellow. Left: bottom view. Right: lateral view.

WSS trends extracted from those apical regions for each considered residual EF% are reported below (Figure 4.7).

WSS were analyzed in terms of three-dimensional components and modulus, but x and y components were approximately zero over the whole cardiac cycle, so that only zWSS, that is WSS along the axial direction of the LV, were reported.

The obtained results were compared to the zWSS trends of a healthy LV (Figure 4.7a) evaluated, with the same approach, in a previous study [53].

Figure 4.7: zWSS trends over a whole cardiac cycle for the three different surfaces; (A) healthy LV, pathological LV with 15% EF (B), 10% EF (C), 5% EF (D).

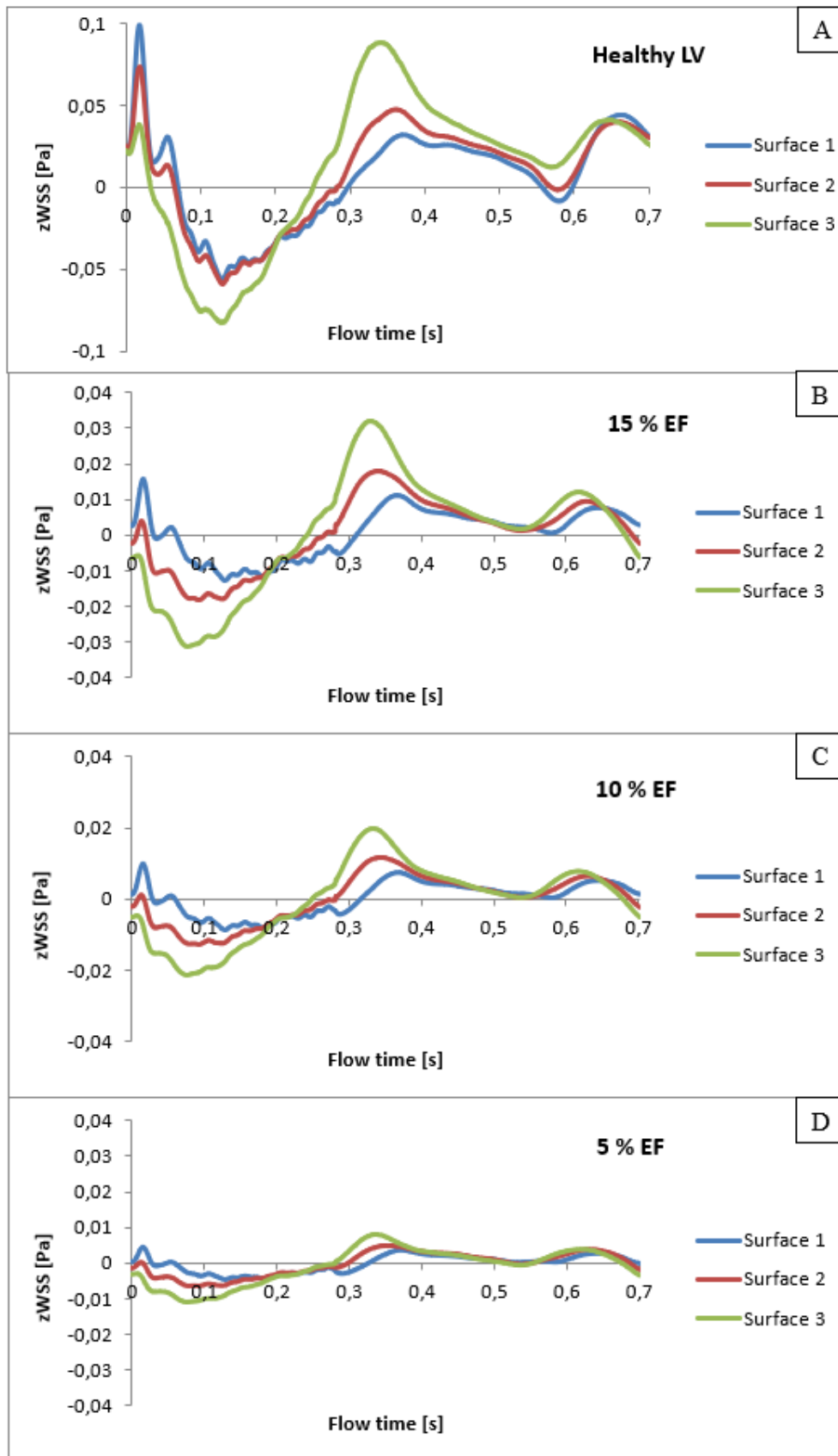As it can be noticed, WSS peak values in the examined pathological conditions (Figures 4.7b-d) are approximately two order of magnitude lower than those in the healthy LV (Figure 4.7a), revealing the presence of a huge stagnation region in the ventricular apex.

Figures 4.7b-d show that surface 1, the closest to the ventricular apex, is characterized by the lowest values of WSS, for all the considered values of residual EF. When analyzing WSS trends for decreasing levels of residual EF% (from 15 to 5%), the maximum WSS value is lowered by one of order magnitude, from 0.015 Pa (15% EF) to 0.005 Pa (5% EF). This behaviour can be observed in Figure 4.8, where zWSS trends obtained for the three EF%, on surface 1, were plotted on the same graph.
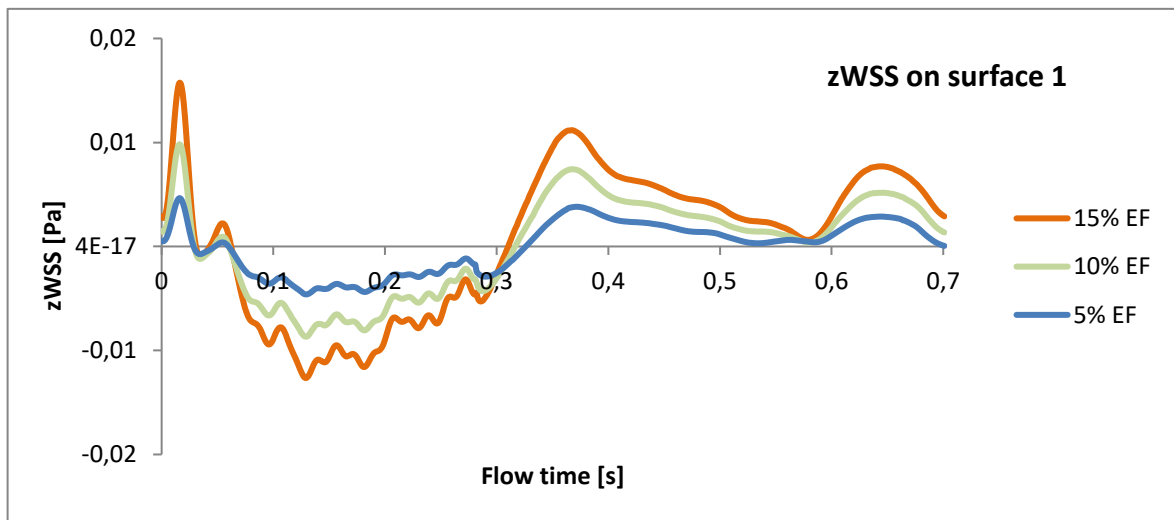
Figure 4.8: zWSS trends on surface 1 for 15%, 10%, and 5% EF.

Hence, our results suggest that LV residual contractility plays a key role in promoting potential thrombus formation in a pathologically dilated LV.

Decreasing values of residual LV contractility determine a progressive reduction of blood velocity through the cardiac cycle, modifying significantly blood flow in the apical region so to create stagnation areas and, eventually, thrombosis.
The above described phenomenon was investigated and quantified extracting blood peak values, both in systole and diastole, in different areas of the LV, in particular in the apical region.

v_{MAX} (m/s) - Systolic Peak				
	Healthy LV	**15% EF**	**10% EF**	**5% EF**
Aortic Valve	1.17	0.27	0.18	0.089
Surface 1	0.063	0.0074	0.0053	0.0040
Surface 2	0.067	0.0081	0.0056	0.0044
Surface 3	0.070	0.0086	0.0060	0.0048

Table 4.1: Blood maximum velocity values at the systolic peak, computed at the aortic valve and in the apical region of the LV. Values are expressed in [m/s].

v_{MAX} (m/s) - E Wave				
	Healthy LV	**15% EF**	**10% EF**	**5% EF**
Mitral Valve	0.42	0.12	0.08	0.04
Surface 1	0.051	0.020	0.022	0.024
Surface 2	0.058	0.028	0.027	0.028
Surface 3	0.065	0.031	0.030	0.031

Table 4.2: Blood maximum velocity values at the diastolic E wave, computed at the mitral valve and in the apical region of the LV. Values are expressed in [m/s].

At this aim, three planes were defined as transverse planes crossing apical surfaces 1, 2 and 3, respectively; then blood maximum velocity, at systolic peak and during the diastolic E wave, was evaluated on the aortic and mitral valvular planes and in the apical region, exploiting the above defined planes.

As it can be noticed from Tables 4.1 and 4.2, as expected for the healthy condition, blood v_{MAX} is higher in systole than in diastole; moreover, considering the systolic peak (Table 4.1), blood flow v_{MAX} for the healthy LV are one or two order of magnitude greater than those of pathological conditions. In the examined pathological conditions, given the reduced LV contractility, blood flow lack of the driving force to be ejected from the aortic valve to the systemic circulation, because of the exhaustion of the contraction mechanism. Hence, the lower the EF%, the lower the v_{MAX}.

In diastole (Table 4.2), v_{MAX} for the healthy LV was found to be one order of magnitude higher than corresponding values for the pathological cases, only when evaluated on the mitral valvular plane and when LV residual contractility was strongly reduced (10% and 5% EF). Instead, in the apical region, blood velocity peak values are comparable in all the examined conditions.

Furthermore, taking into account the pathological conditions, diastolic v_{MAX} values are one order of magnitude higher than the corresponding values in systole, the opposite being found for the healthy LV.

We hypothesize that this behaviour is due to blood mixing in the apical zone, caused by the impact between blood entering from the MV and layers of fluid still in the LV, that were not ejected during the preceding systolic phase.

However, when LV contractility is reduced, blood velocities are close to zero in the apical region, hence insufficient to ensure proper LV washout, representing a marker for blood stasis.

Blood stasis is a recognized risk factor for intraventricular thrombosis and thromboembolic events as it induces accumulation of both activated and sensitized platelets, which may get trapped in recirculation zones because of the limited washout and exposed to low dynamic -i.e., thrombogenic - shear stress for elongated durations.

4.2.   Set 2 *Post-Implant* A

In this set, the CFD model is based on the same pathologically dilated patient-specific LV of Set 1, post LVAD implantation. Eight test conditions were considered, obtained combining 4 values of residual EF% (0 - 5 - 10 - 15%) with 7 levels of support (LVAD flow rates) (see § 3.6.2 for details).

Patterns of vortex formation, velocity contours, and WSS in the LV apical zone were analyzed to investigate the hemodynamics of the LVAD-assisted LV, and to evaluate the mutual interaction between different values of LV residual contractility and LVAD flow rate.

4.2.1. Patterns of Vortex Formation and Evolution

For what concerns patterns of vortex formation and development, as for the *pre*-implant model, vortex dynamics was analyzed applying the Q-criterion (see § 3.8.1).

Vortex formation and development, and their motion in the LV during systole and diastole, are described here just for one test condition (15% EF + LVAD 2.20), since it was noticed that this process was similar for each condition in the set. We hypothesized this was due to the fact that, in the simulated configurations, the LV volume displacements changed accordingly to the total CO, while the applied kind of motion did not change.

As Figures 4.9 and 4.10 show, the difference between the considered test conditions is in terms of the dimension and coherence of the vortexes, rather than in their number and kind of motion. Moreover, a progressive disappearance of secondary vortexes close to the LVOT was noticed, as the EF% decreases to 0%.

Qualitatively, the greatest difference in terms of vortex coherence was found between test conditions with a residual EF% of 0% and 15%, that is for the extremes of the LV contractility range.

Figure 4.9: 3D Vortex field during systolic acceleration, obtained applying the Q-criterion; Test conditions: (a) 15% EF + LVAD 2.20 L/min; (b) 10% EF + LVAD 2.70 L/min; (c) 5% EF + LVAD 3.80 L/min; (d) 0% EF + LVAD 5.00 L/min.
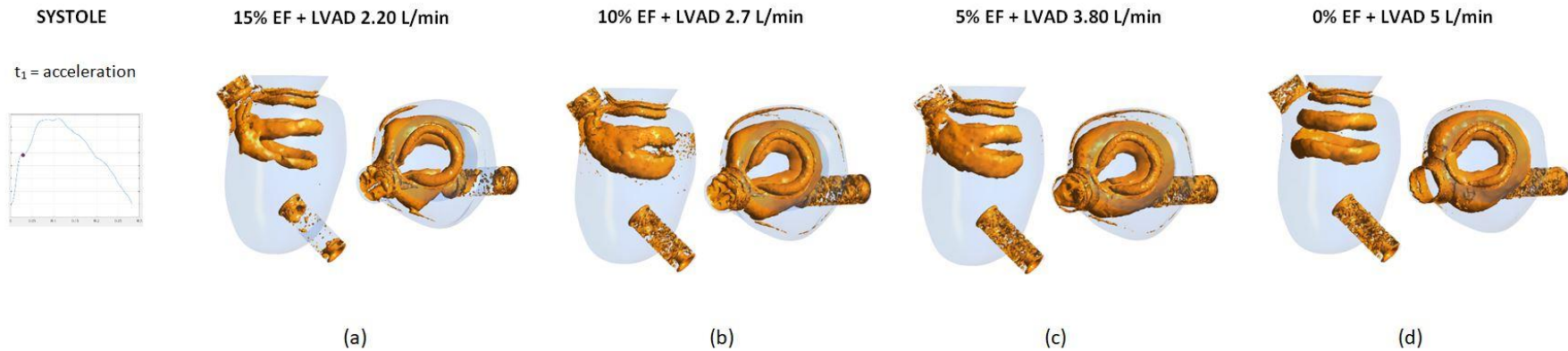

Figure 4.10: 3D Vortex field during diastolic acceleration, obtained applying the Q-criterion; Test conditions: (a) 15% EF + LVAD 2.20 L/min; (b) 10% EF + LVAD 2.70 L/min; (c) 5% EF + LVAD 3.80 L/min; (d) 0% EF + LVAD 5.00 L/min.
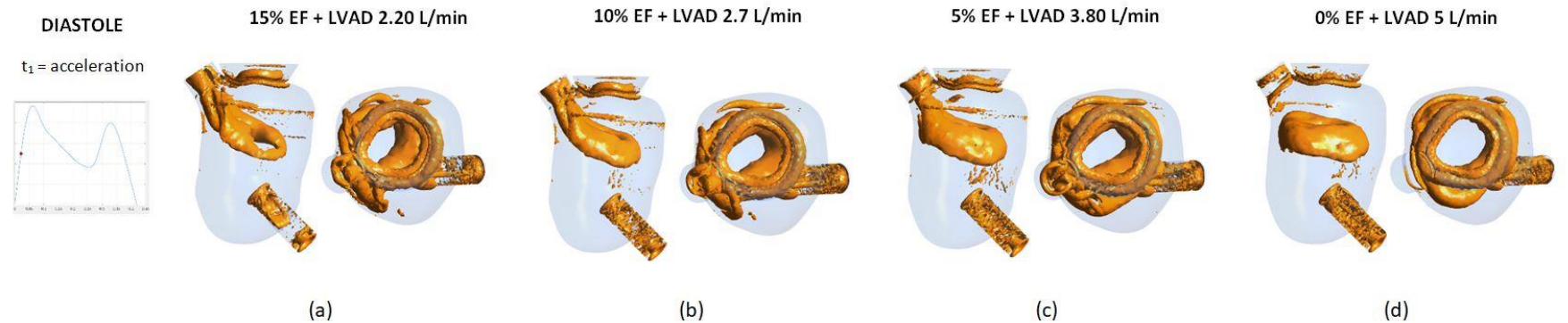
107

Furthermore, it was observed that, comparing conditions with equal LV residual EF%, the increase in LVAD flow rate did not determine a significant variation in vortex dynamics; as a matter of fact, during systole, a rise in LVAD flow rate had the sole effect of increasing the distance between the main vortexes (Figure 4.11), while, in diastole, the main vortex was lightly stretched toward the inflow cannula (Figure 4.12). Hence, these observations suggest that LV residual EF% has a predominant role in determining LV hemodynamics, with respect to the LVAD flow rate. Similar observations can be made for test condition sharing a residual EF of 5%.

Figure 4.11: 3D Vortex field during systolic acceleration, obtained applying the Q-criterion; Test conditions: (a) 10% EF + LVAD 2.20 L/min; (b) 10% EF + LVAD 2.70 L/min; (c) 10% EF + LVAD 3.00 L/min.
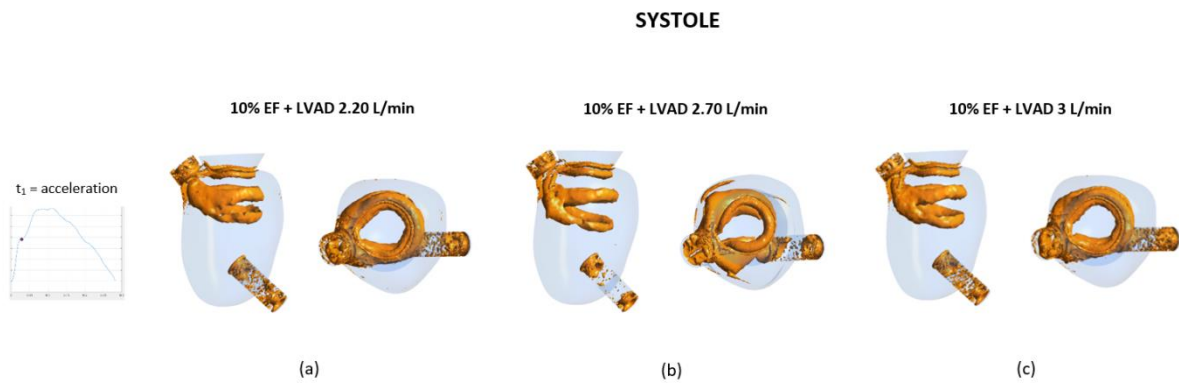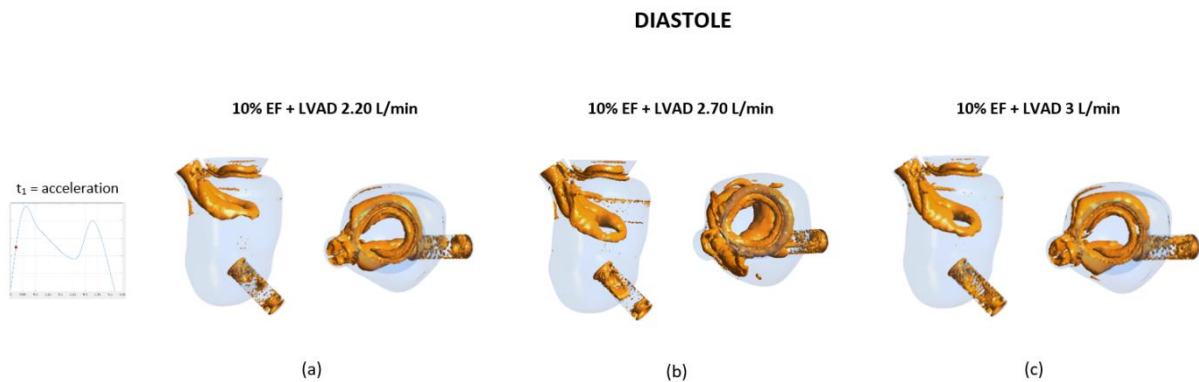

Figure 4.12: 3D Vortex field during diastolic acceleration, obtained applying the Q-criterion; Test conditions: (a) 10% EF + LVAD 2.20 L/min; (b) 10% EF + LVAD 2.70 L/min; (c) 10% EF + LVAD 3.00 L/min.

In Figures 4.13 and 4.14, 3D vortex dynamics for test condition 15% EF + LVAD 2.20 L/min is reported, during systole and diastole, respectively.

In early systole and at the systolic peak (Figure 4.13a and b), three vortexes are generated: the smaller one immediately beneath the MV, while two main vortexes in the centre of the LV. In the deceleration phase (Figure 4.13c) the third vortex is disrupted, while the second one moves towards the LV apex.

In diastole (Figure 4.14), the opposite phenomenon occurs: the main vortex in early diastole (Figure 4.14a and b) moves towards the inflow cannula and, in mid and late diastole, it is followed by a second vortex, as blood enters the LV from the mitral orifice (Figure 4.14 c and d). In both phases of the cardiac cycle, the LV apical zone was not involved in vortical phenomena, thus resulting in an increased risk for potential thrombus formation.
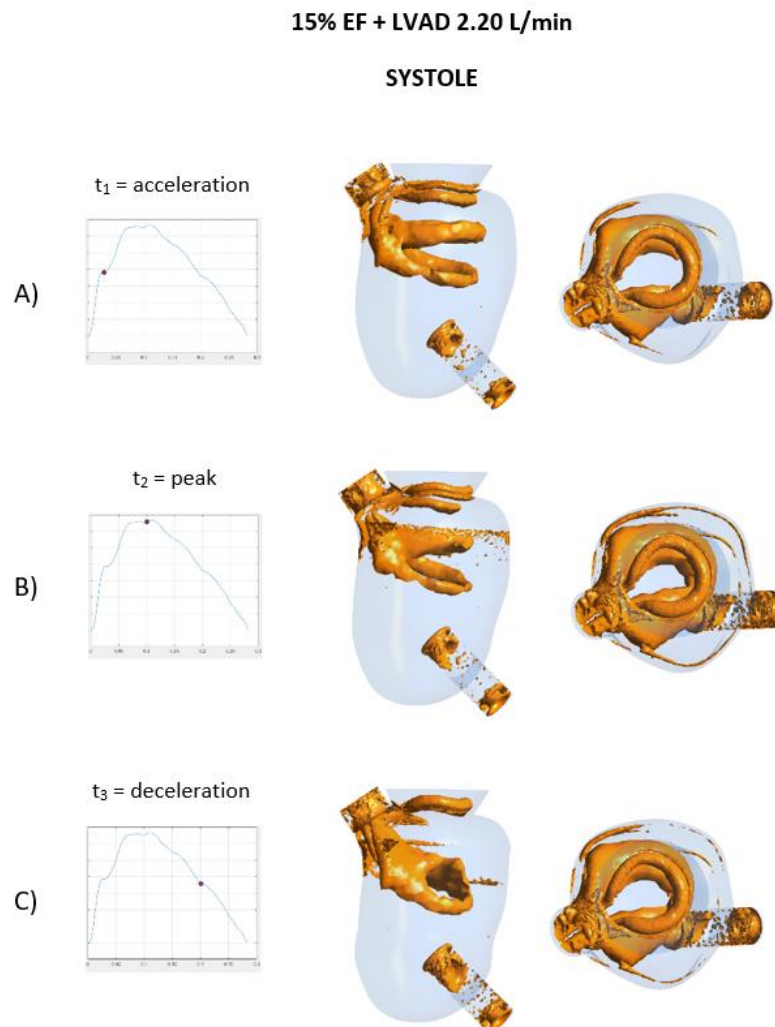
Figure 4.13: 3D Vortex field in systole obtained applying the Q-criterion; (A) Systolic acceleration; (B) Systolic peak; (C) Systolic deceleration. Results are shown for test condition 15% EF + LVAD 2.20 L/min.

15% EF + LVAD 2.20 L/min

DIASTOLE

t_1 = acceleration

A)

t_2 = E wave

B)

t_3 = A wave

C)

t_4 = deceleration

D)
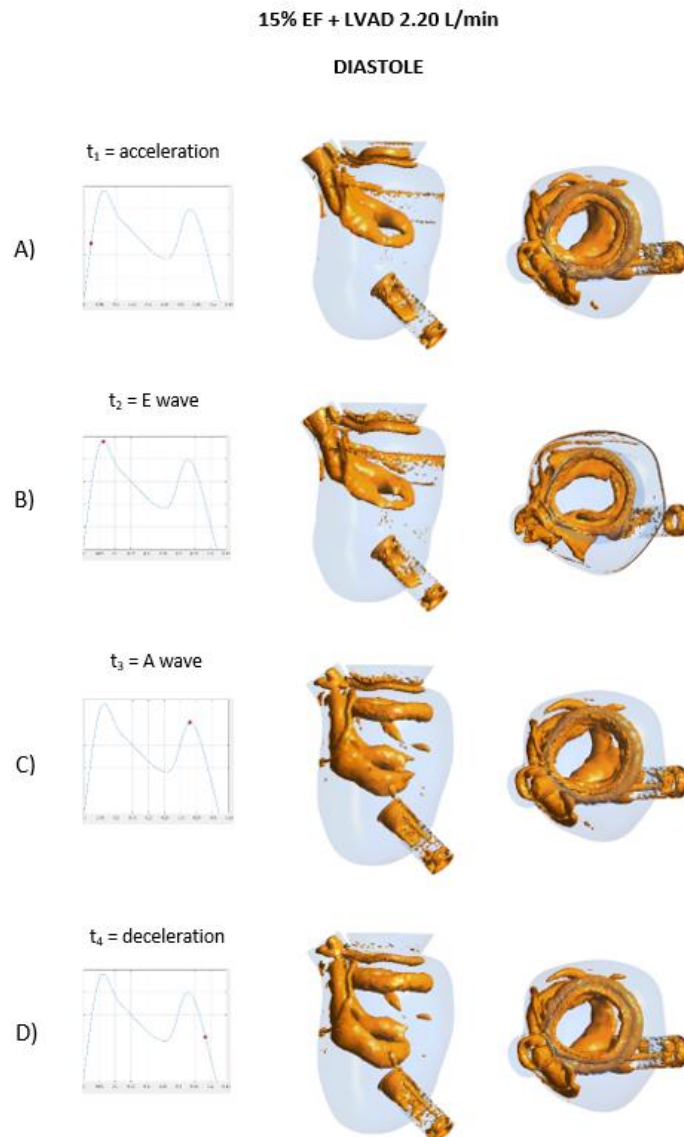
Figure 4.14: 3D Vortex field in diastole obtained applying the Q-criterion; (A) Diastolic acceleration; (B) E wave; (C) A wave; (D) Diastolic deceleration. Results are shown for test condition 15% EF + LVAD 2.20 L/min.

In Figure 4.15 and 4.16, velocity contours and vectors on a longitudinal plane across the mitral/aortic orifices and the LV apex, are shown, for the same test condition analyzed so far; in this way blood velocity magnitude values and vortexes directions of rotation can be identified.

Results showed that, in systole, blood was simultaneously ejected through both the aortic valve and the LVAD inflow cannula, establishing a parallel flow pattern. Thus, many

vortices with different directions of rotation appeared in the LV, which caused the flow to be disorderly.

Hence, during systole, no predominant clockwise or counter-clockwise rotation was observed in the intraventricular flow patterns (Figure 4.15a and b), except when systolic deceleration took place. During this phase (Figure 4.15c), a large counter-clockwise rotation was formed in the LV, driving the blood stream in the LVAD inflow cannula and towards the aortic valve.

On the other hand, in diastole (Figure 4.16), the inflow mitral jet hit the intraventricular septum, generating a large counter-clockwise rotation, so as to direct the blood flow to the inflow cannula. A small, clockwise vortex was formed in the LVOT, the vortical structure more evident in late diastole (Figure 4.16c and d).
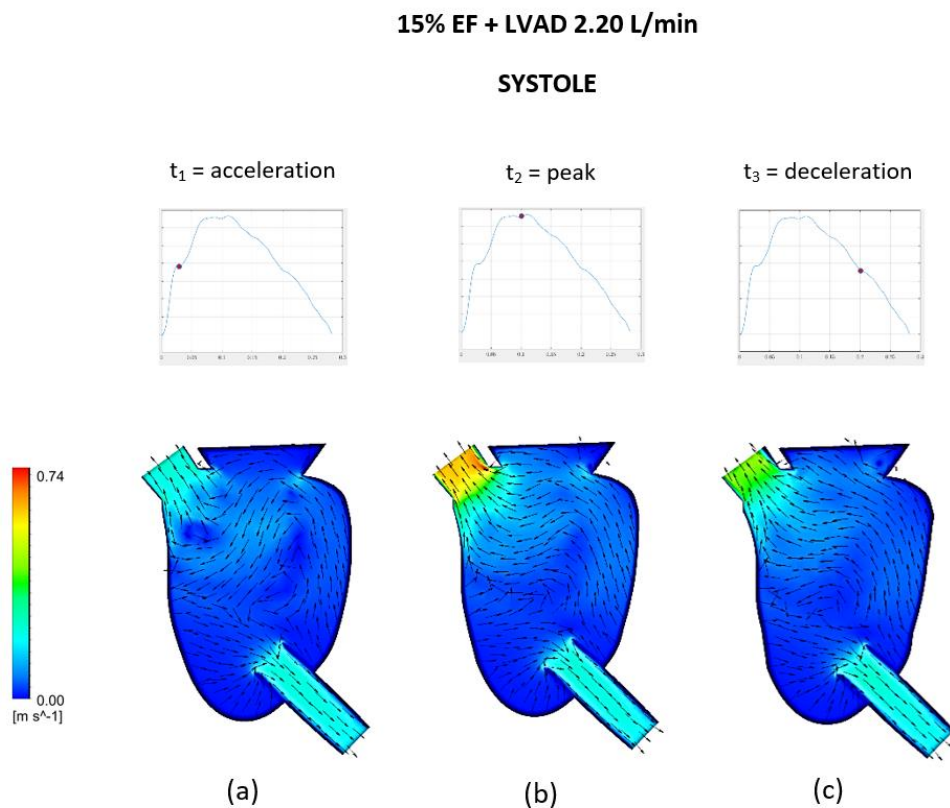

Figure 4.15: Systolic intraventricular flow, considering test condition 15% EF + LVAD 2.20 L/min. Vectors and velocity magnitude contours were obtained for systolic acceleration (a), systolic peak (b), and systolic deceleration (c).

111
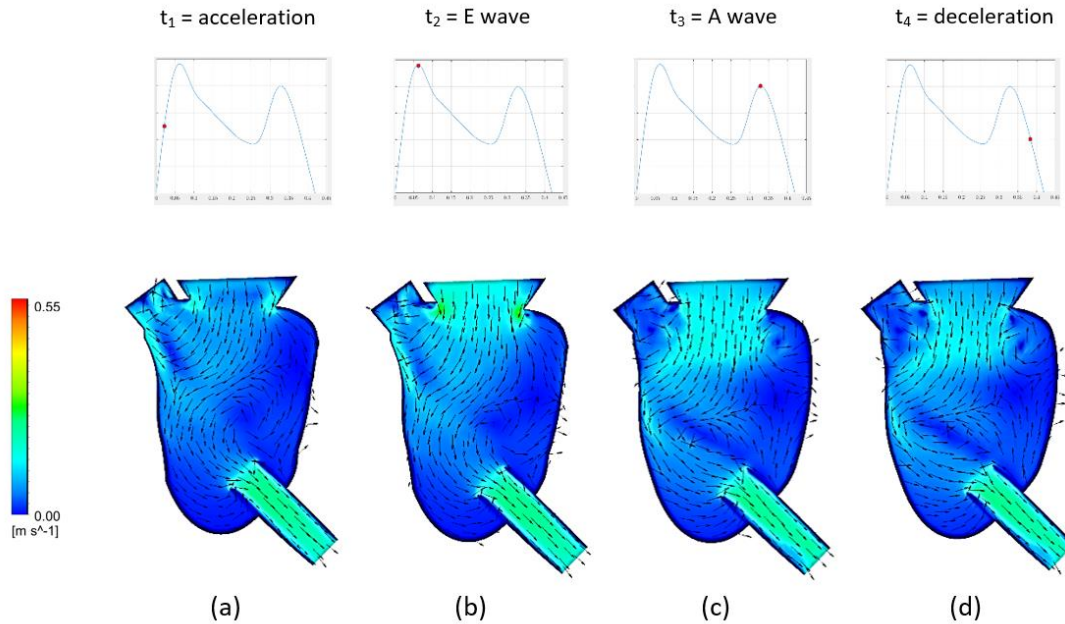
Figure 4.16: Diastolic intraventricular flow, considering test condition 15% EF + LVAD 2.20 L/min. Vectors and velocity magnitude contours were obtained for diastolic acceleration (a), E wave (b), A wave (c), and diastolic deceleration (d).

For what concerns 3D vortex dynamics, as pointed out previously, the considered pathological test conditions differed only for dimension and coherence of the vortexes; the observed variation was more evident between test conditions 15% EF + 2.20 L/min LVAD flow rate and 0% EF + 5 L/min LVAD flow rate.

Here, a detailed comparison between these two pathological conditions is provided.

When EF was equal to 15% (Figure 4.17a and c), vortexes were shifted towards the intraventricular septum and moved toward the LVOT and the aortic valve, while, by contrast, when the LV was fully supported, vortexes were compact and coherent in the LV, and small vortexes appeared all along the inflow cannula (Figure 4.17b and d).
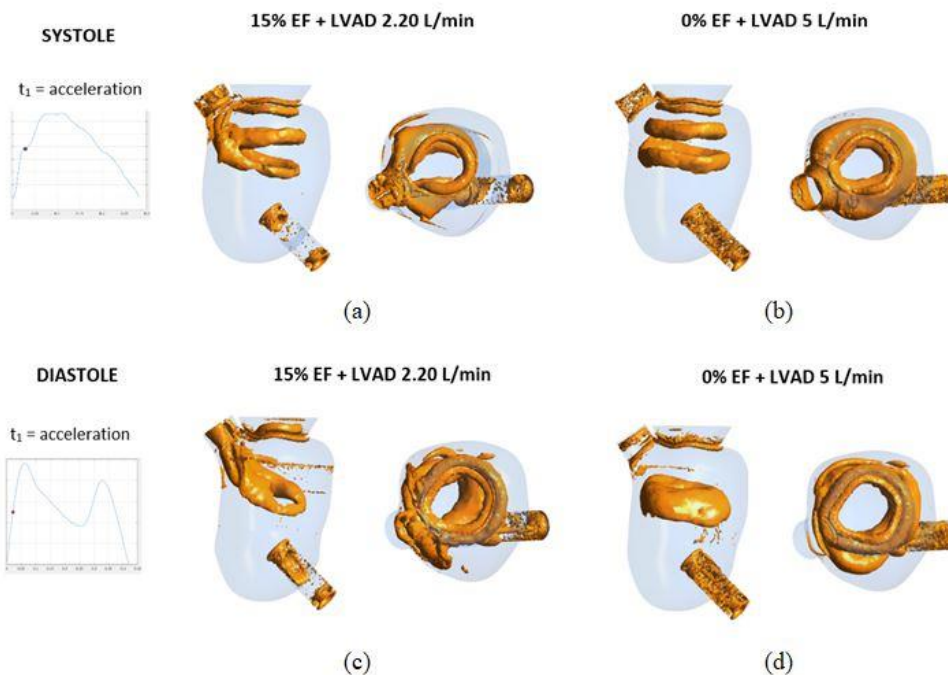
Figure 4.17: 3D Vortex fields at systolic (top) and diastolic (bottom) acceleration phases; (a) and (c) refer to test condition 15% EF + LVAD 2.20 L/min; (b) and (d) refer to test condition 0% EF + LVAD 5.0 L/min.

3D vortex field, for each test condition in Set 2, were further compared with corresponding data from simulation Set 1 (*pre-implant* model), namely considering equal degrees of LV residual contractility (for instance 15% EF *pre-implant* vs. 15% EF + 2.20 L/min LVAD flow rate).

As it can be observed from Figures 4.1 and 4.4, pertaining to the *pre-implant* model, the detected vortexes were confined in the upper portion of the LV (especially for the 10 and 5% EF conditions), resulting more compact and smaller than those analyzed in Set 2 (Figures 4.9-4.14), both in systole and diastole. We suggest that the described phenomenon is due to the cannula suction action that, combined with residual EF, improves LV washout.

A comparative analysis between the healthy condition and the *post-implant* configurations revealed a substantial difference in vortex dynamics. Indeed, during early systole, only two broad vortices were detected in the examined *post* LVAD implantation LV (Figure 4.9), while multiple vortical structures characterized the physiological scenario (Figure 4.1a). Furthermore, in the healthy LV, in peak systole and in the deceleration phase (Figure 4.1b and c), vortexes were completely disrupted because of the ejection of blood through the aortic valve, while they persisted in the *post-implant* LV (Figure 4.13b and c).

Similar observation can be made for the diastolic phase, too (Figure 4.4 for the healthy LV and Figure 4.14 for the *post-implant* LV).

4.2.2. Thrombogenic Potential: the Effect of LVAD Implantation

As for *pre-implant* simulation Set 1, WSS were extracted in the three apical surfaces for Set 2 as well. As for Set 1, WSS were analysed in terms of three-dimensional components and modulus, but x and y components were approximately zero over the whole cardiac cycle, so that only zWSS, that is WSS along the axial direction of the LV, were reported.

In Figure 4.18, WSS trends associated to the boundary values of residual EF, that is 15% and 0%, are compared. As the residual EF approaches 0%, WSS maximum values are lowered of one order of magnitude. Therefore, as for the *pre-implant* configurations, our results suggest that LV residual contractility plays a key role in promoting potential thrombus formation.

Additionally, differently from the *pre-implant* configuration (Figures 4.7b-d), all the apical zones are critical, because WSS trends are overlapped, and WSS values are approximately one order of magnitude lower, especially in the systolic phase (Figure 4.18). Hence, the obtained results suggest that the implantation of a LVAD inflow cannula determines a further significant reduction of WSS peak values.

Furthermore, a comparative analysis between *post-implant* (Figure 4.18) and physiologic (Figure 4.7a) WSS trends revealed that the former were approximately between two (15% EF + 2.20 L/min LVAD flow rate) and three (0% EF + 5 L/min LVAD flow rate) order of magnitude lower, suggesting the presence of a huge stagnation region in the ventricular apex.
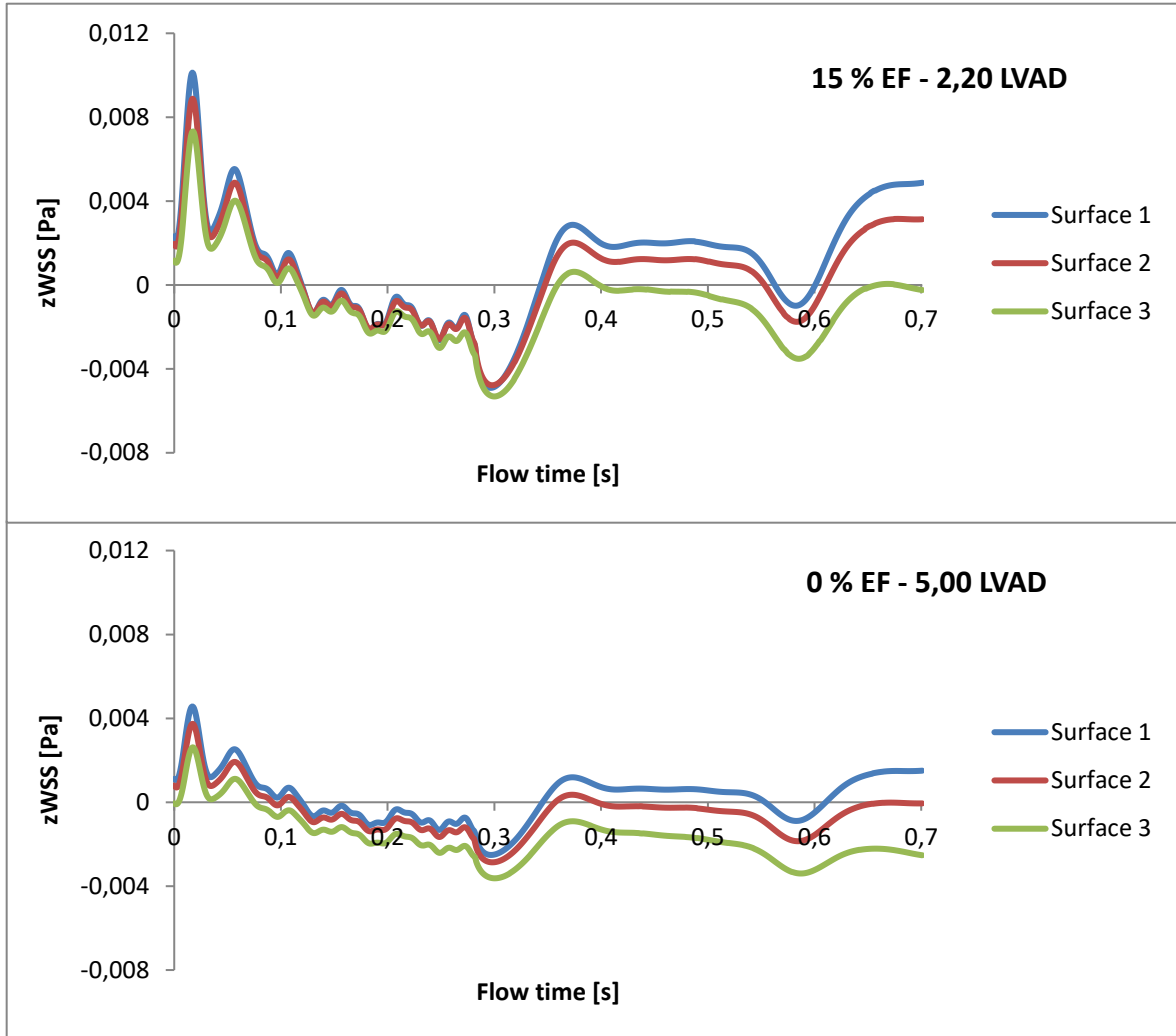
Figure 4.18: zWSS trends for 15% EF + 2.20 L/min LVAD flow rate (top panel); 0% EF + 5.00 L/min LVAD flow rate (bottom panel).

Keeping constant LV residual contractility, equal to 10% for instance, WSS peak values increase with LVAD flow rate. As a matter of fact, Figure 4.19 shows that WSS peak value increases from 0.007 Pa, when LVAD flow rate is around 2.20 L/min, to 0.008 Pa, LVAD flow rate being equal to 3.00 L/min. The same phenomenon was observed for 5% EF test conditions (trends are not shown).
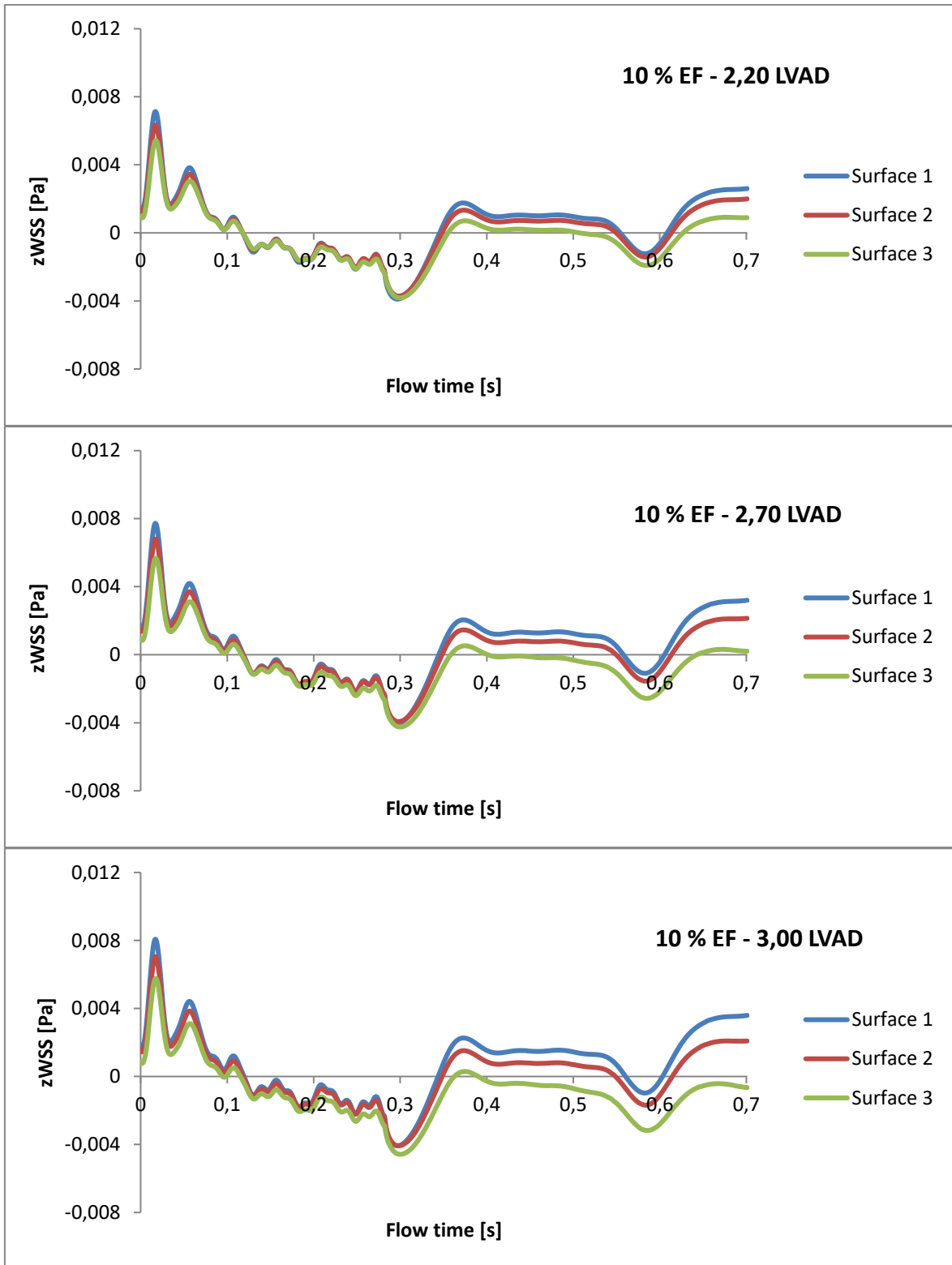
Figure 4.19: zWSS trends for 10% EF with increasing levels of LVAD flow rates: (from top to bottom) 2.20 L/min, 2.70 L/min, and 3.00 L/min.
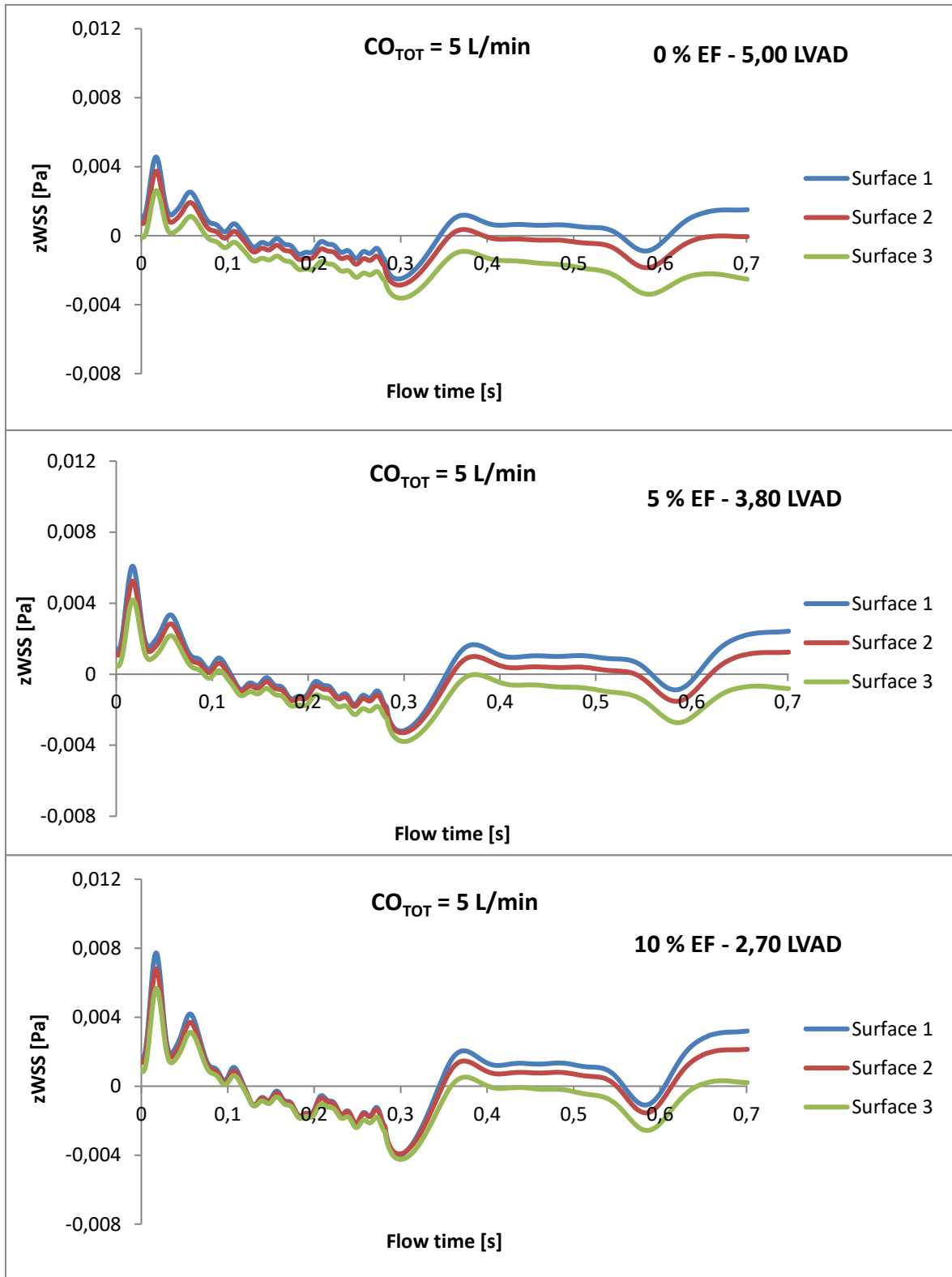
Figure 4.20: zWSS trends for three different combination of EF and LVAD flow rate. The total cardiac output considered is 5 L/min (EF+LVAD flow rate): (from top to bottom) 0% EF + 5 L/min LVAD flow rate, 5% EF + 3.80 L/min LVAD flow rate, and 10% EF 2.70 L/min LVAD flow rate.

WSS trends were further compared looking at the total cardiac output, defined as the sum of native cardiac output (which depends on the degree of LV residual contractility) and LVAD flow rate. WSS trends considered for the comparison were extracted from test conditions that ensured a total CO of 5.00 L/min (Figure 4.20).

WSS peak values decrease when the LV residual contractility is reduced, in other words with increasing levels of cardiac impairment.

Therefore, WSS are strongly influenced by LV residual contractility and, to a lesser extent, by LVAD flow rate.

As previously done for Set 1, blood peak values were investigated, both in systole and diastole, in different areas of the LV, in particular in the apical region, to quantify blood stasis, for test conditions sharing the same total CO, equal to 5 L/min.

The same three planes were defined crossing apical surfaces 1, 2 and 3, respectively; then blood maximum velocity, at systolic peak and during the diastolic E wave, was evaluated on the aortic and mitral valvular planes and in the apical region, exploiting the above defined planes. Values are reported in Tables 4.3 and 4.4.

At the systolic peak (Table 4.3), results showed that blood velocity increased with the residual EF%, in two specific areas of the LV, that is the aortic valve and surface 1 (the closest to the LV apex), while remaining almost constant on the other two surfaces.
In diastole (Table 4.4), a similar behaviour was observed.

However, looking over the whole cardiac cycle, velocity peak values were close to zero, thus proving blood stasis, as for the *pre-implant* test conditions.

v_{MAX} (m/s) - Systolic Peak – CO_tot 5 L/min		
	10% EF + 2.7 L/min	**5% EF + 3.8 L/min**	**0% EF + 5 L/min**
Aortic Valve	0.44	0.28	0.1
Surface 1	0.0052	0.0043	0.0035
Surface 2	0.007	0.0073	0.0078
Surface 3	0.009	0.01	0.01

Table 4.3: Blood maximum velocity values at the systolic peak, computed at the aortic valve and in the apical region of the LV. Values are expressed in [m/s].

v_{MAX} (m/s) - E Wave - CO_tot 5 L/min		
	10% EF + 2.7 L/min	**5% EF + 3.8 L/min**	**0% EF + 5 L/min**
Mitral Valve	0.15	0.14	0.13
Surface 1	0.0045	0.0038	0.0035
Surface 2	0.0068	0.0068	0.0073
Surface 3	0.0085	0.0086	0.01

Table 4.4: Blood maximum velocity values at the diastolic E wave, computed at the mitral valve and in the apical region of the LV. Values are expressed in [m/s].

4.3. Set 3 *Post-Implant* B

This last simulation set consists of 2 test conditions, selected from Set 2 simulation matrix, namely 10% EF + 2.70 L/min LVAD flow rate and 5% EF + 3.80 L/min LVAD flow rate. These two configurations were chosen to study the impact of cannula position on LV hemodynamics, since they provide to the patient a total CO equal to 5 L/min, a condition mimicking the average CO at rest.

The LVAD inflow cannula was modelled in order to have its longitudinal axis intersecting the LV apex and the centre of the mitral valve orifice (apical positioning).

To identify the most hemodynamically favourable LVAD implantation configuration, results from *post-implant* B simulation set were compared with corresponding simulations from *post-implant* A simulation set, where the cannula orientation accurately replicated the patient-specific configuration.

4.3.1. Patterns of Vortex Formation and Evolution

As previously done, vortex dynamics was analyzed applying the Q-criterion.

The 3D intraventricular vortex field is reported in Figure 4.21b and d, at selected systolic and diastolic time points (i.e. systolic and diastolic acceleration), for test condition 10% EF + LVAD 2.70 L/min.

As it can be noticed, the obtained vortex dynamics is apparently not dissimilar from that characterizing corresponding *post-implant* A simulations (Figure 4.21a and c). Similar observations can be made for test condition 5% EF + 3.80 L/min LVAD flow rate.

More interesting is the analysis of the intraventricular flow through velocity vectors, on a longitudinal plane across the mitral/aortic orifices and the LV apex; this way blood velocity magnitude values and vortexes directions of rotation can be identified.

121
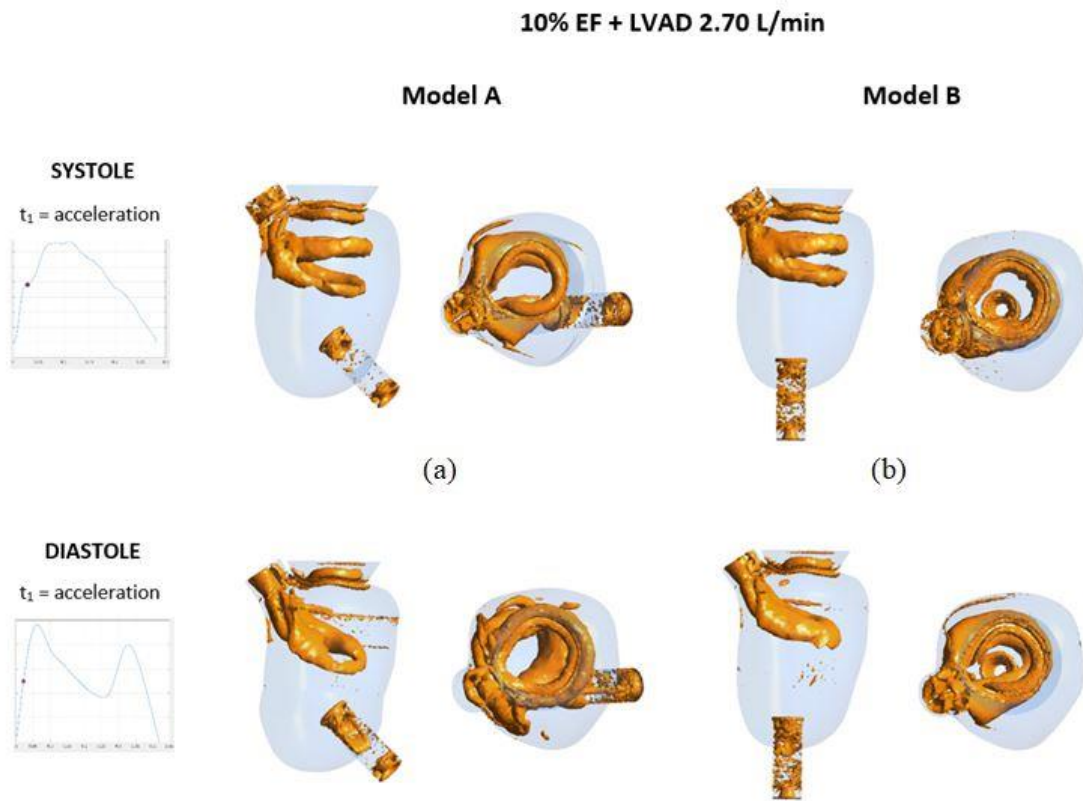
Figure 4.21: 3D Vortex fields at systolic (top) and diastolic (bottom) acceleration phases for test condition 10% EF + LVAD 2.70 L/min; (a) and (c) refer to *post*-implant Model A; (b) and (d) refer to *post*-implant Model B.

Differently from matching *post-implant A* simulations, a predominant counter-clockwise rotation was observed throughout the systolic phase (Figure 4.22), that directed blood in the LVOT and the cannula inlet.

In diastole, when the inflow cannula was inserted in the apex, blood took a more direct route through the LV, from the MV to the inflow cannula (Figure 4.23).

These findings are coherent with results obtained by Chivukula *et al.* [37], when investigating the impact of surgical angulation of the inflow cannula on LV thrombogenic potential.

In the study, it was proven that inflow cannula angles closer to the apical axis resulted in more linear blood flow from the MV to the LVAD cannula. Deviations of LVAD inflow cannula alignment away from the apical LV axis induced unfavourable hemodynamics. Indeed, the risk for both high shear, which promotes platelet activation, and stagnation and recirculation regions, which influence platelet agglomeration, was likely to increase, thus rising, in turn, the thrombogenic potential.

Therefore, the comparative analysis suggests that the LVAD inflow cannula in the apical configuration exerts a more effective suction action on blood in the apical region of the LV, with respect to the patient-specific positioning.

Figure 4.22: Systolic intraventricular flow, considering test condition 10% EF + LVAD 2.70 L/min. Vectors and velocity magnitude contours were obtained for systolic acceleration (a), systolic peak (b), and systolic deceleration (c).

15% EF + LVAD 2.20 L/min

DIASTOLE

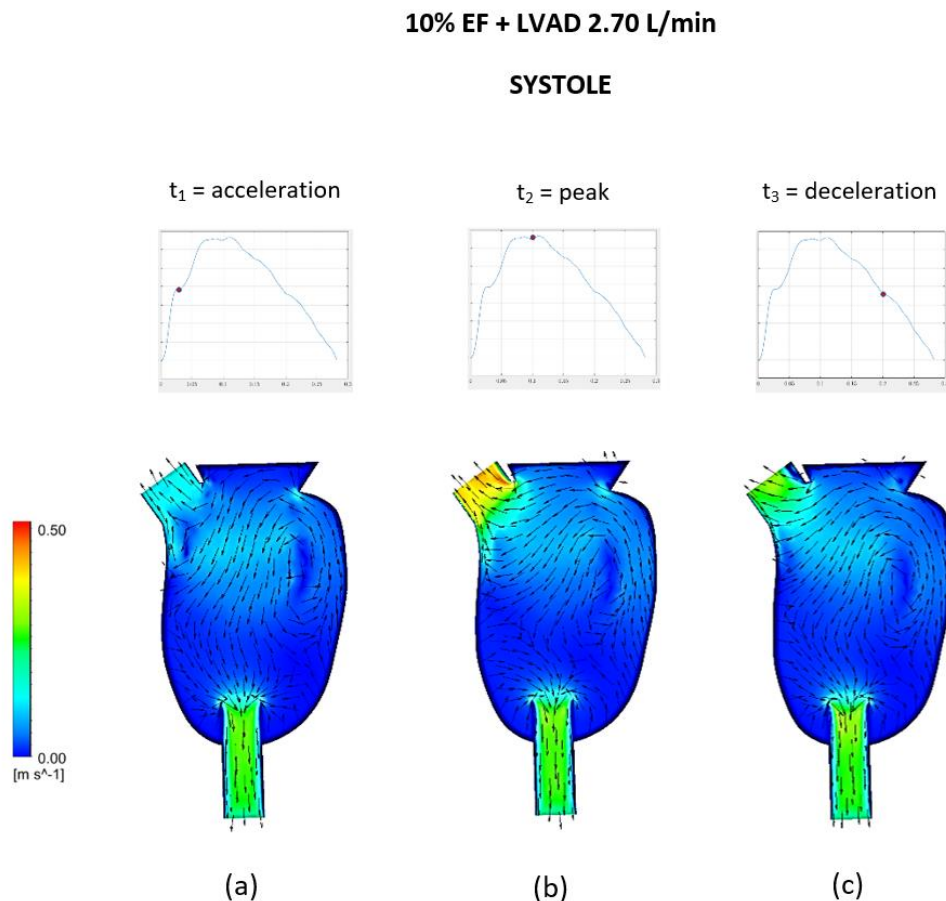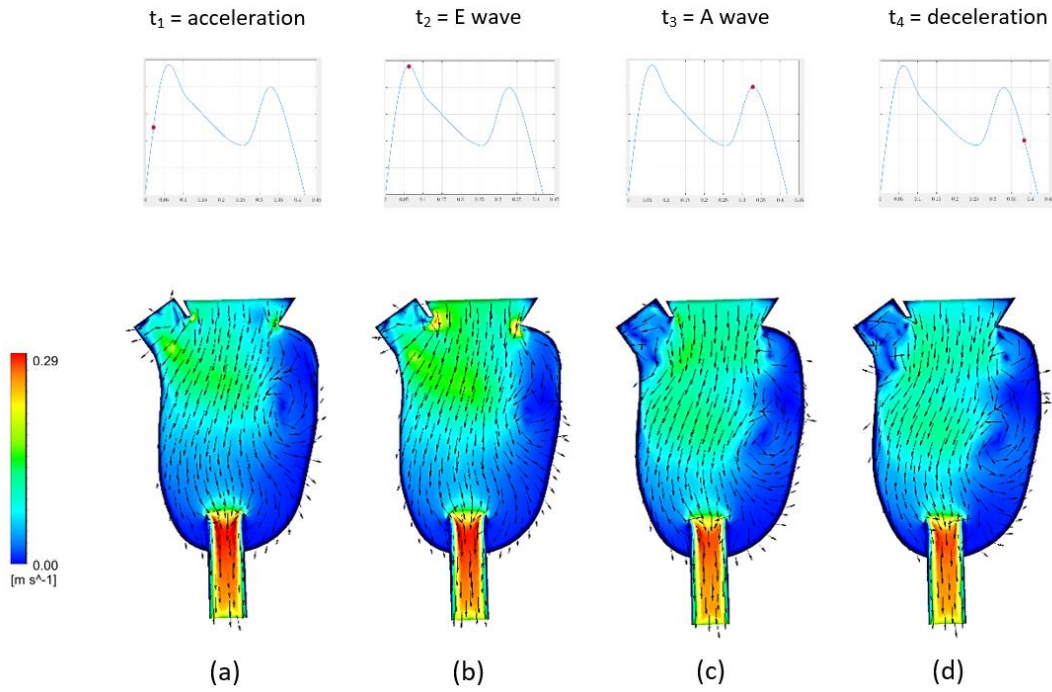| t₁ = acceleration | t₂ = E wave | t₃ = A wave | t₄ = deceleration |

(a) (b) (c) (d)

Figure 4.23: Diastolic intraventricular flow, considering test condition 10% EF + LVAD 2.70 L/min. Vectors and velocity magnitude contours were obtained for diastolic acceleration (a), E wave (b), A wave (c), and diastolic deceleration (d).

4.3.2. Thrombogenic Potential: the Effect of Cannula Positioning

WSS were analyzed in terms of three-dimensional components and modulus, but x and y components were approximately zero over the whole cardiac cycle, so that only zWSS, that is WSS along the axial direction of the LV, were reported.

In this set of simulations, cannula position was varied: moving from the patient-specific configuration to the reference apical positioning (as defined in § 4.3).

The aim was to quantify the impact of cannula position on LV thrombogenicity, so to identify the most hemodynamically favourable LVAD implantation configuration between the examined ones.

Figure 4.24 and 4.25 show that WSS for the apical positioning are one order magnitude greater than those obtained for the patient-specific positioning. For instance, examining test condition 5% EF + 3.80 L/min LVAD flow rate (Figure 4.24), WSS peak value varies from 0.006 Pa, to 0.016 Pa. Similarly, for test condition 10% EF + 2.70 L/min LVAD flow rate (Figure 4.25), WSS maximum increases from 0.008 Pa to 0.02 Pa.

In addition, as previously done (§ 4.2.2), blood peak values were investigated, both in systole and diastole, in different areas of the LV, for the apical positioning of the LVAD inflow cannula (see Tables 4.5 and 4.6). Blood v_{MAX} values in the apical configuration were found to be one order of magnitude higher than those from the patient-specific positioning (Tables 4.3 and 4.4).

Hence, less extent of blood stagnation was observed at the apex of the LV in the apical configuration. The obtained results suggest that there might be a higher risk for thromboembolic events when the cannula was in the patient-specific positioning, given the *i)* greater blood stagnation and *ii)* the slower blood flow in areas not directly along the path between the inlet (the mitral valve) and the outlets (LVAD and aortic valve) (Tables 4.3 and 4.4).

v_{MAX} (m/s) - Systolic Peak		
	10% EF + 2.7 L/min	**5% EF + 3.8 L/min**
Aortic Valve	0.43	0.27
Plane 1	0.013	0.01
Plane 2	0.015	0.012
Plane 3	0.015	0.012

Table 4.5: Blood maximum velocity values at the systolic peak, computed at the aortic valve and in the apical region of the LV. Values are expressed in [m/s].

v_{MAX} (m/s) - E Wave		
	10% EF + 2.7 L/min	**5% EF + 3.8 L/min**
Mitral Valve	0.15	0.14
Plane 1	0.012	0.01
Plane 2	0.013	0.09
Plane 3	0.012	0.01

Table 4.6: Blood maximum velocity values at the diastolic E wave, computed at the mitral valve and in the apical region of the LV. Values are expressed in [m/s].

Misalignment between the LV apical axis and the LVAD inflow cannula resulted in more convoluted blood trajectories, increasing the potential for platelets to be trapped in the LV, in particular in the space between the LV wall and the inflow cannula, in the apical region. Platelets trapped in this recirculation/stagnation zones could linger significantly longer in the LV and, thus accumulate higher shear stress given their increased residence time in the MV-to-cannula pathway [37].

Figure 4.24: zWSS trends on the apical surfaces for 5% EF + 3.80 L/min LVAD flow rate. Patient-specific positioning (top); Apical positioning (bottom).

Hence, since even small areas of stagnation may induce formation of thrombi with clinical consequences, our results suggest that an apical configuration for cannula placement might promote "less" thrombogenic hemodynamics. These results were consistent with a previous work reported in literature [30] (see § 2.2.2 for details).
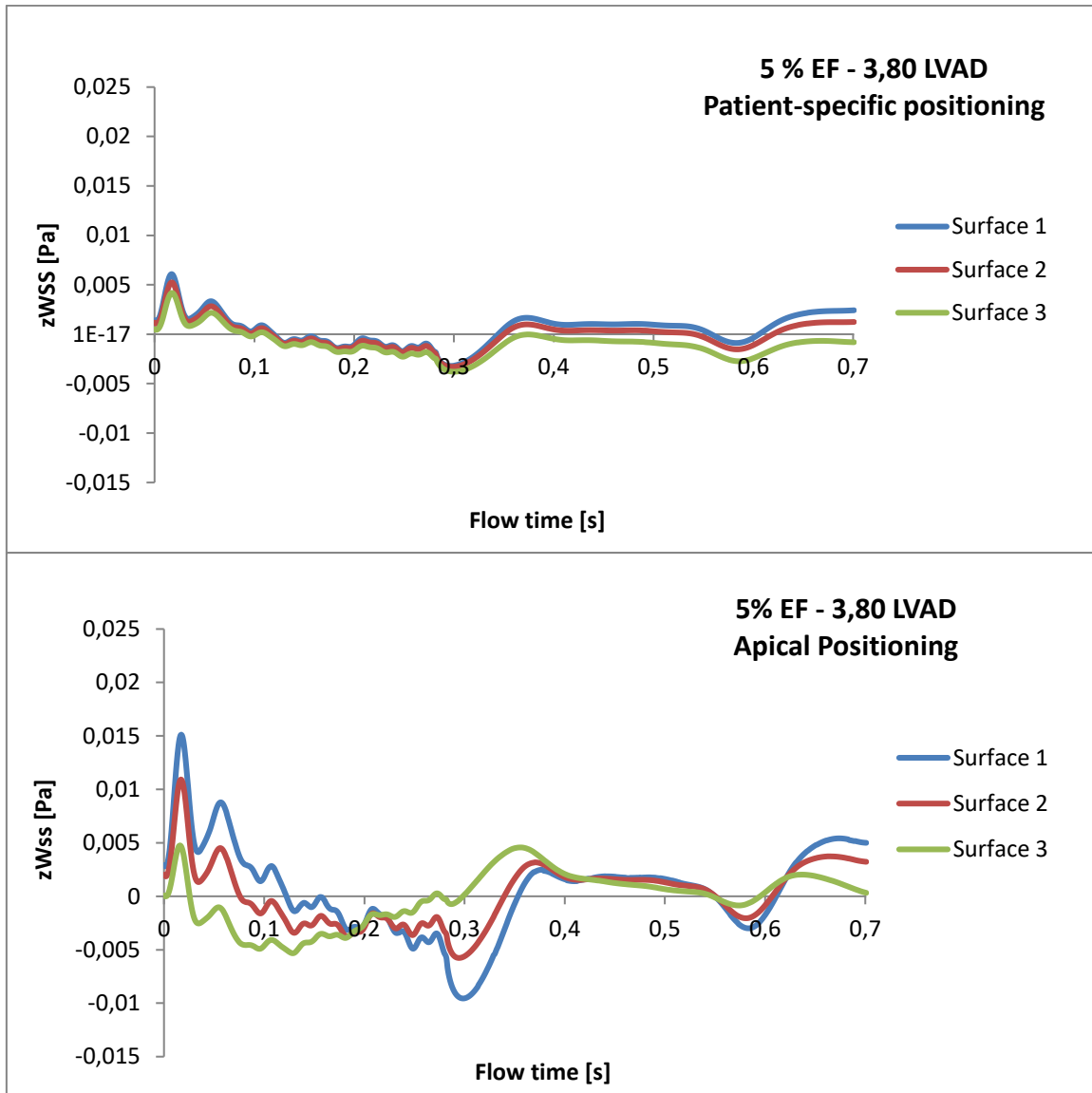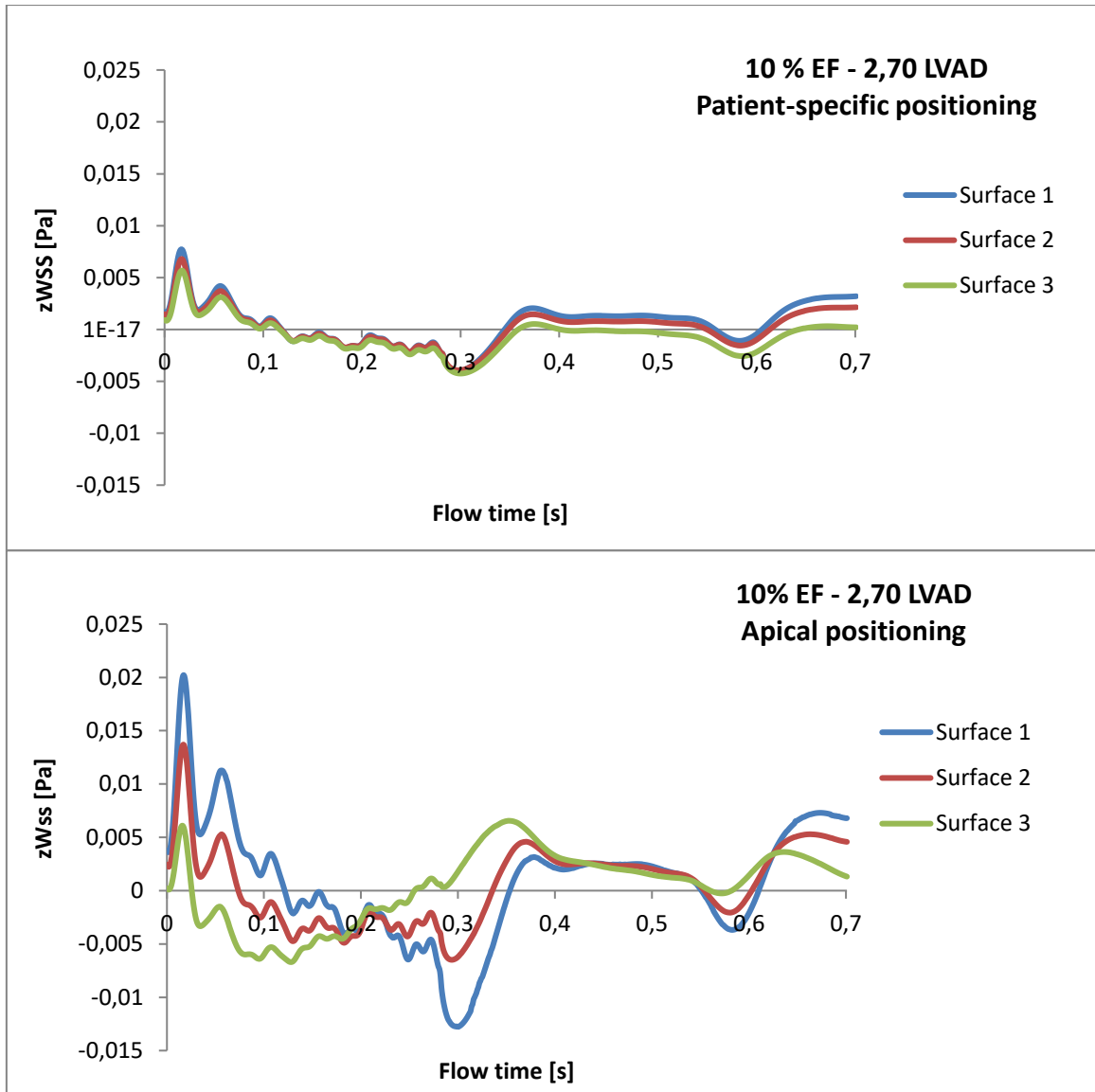
Figure 4.25: zWSS trends on the apical surfaces for 10% EF + 2.70 L/min LVAD flow rate. Patient-specific positioning (top); Apical positioning (bottom).

5.   Conclusions

LVAD support is an established treatment for patients suffering HF, both as bridge-to-transplantation and destination therapy.

Despite the widespread clinical use of VADs, there are a number of complications associated with VAD therapy, the most relevant being those associated with the device-related thrombogenicity. A wide range of mechanisms was suggested to enhance and promote thrombogenesis, such as *i)* shear stress mediated platelet prothrombotic activity, *ii)* LVAD inflow cannula/outflow graft surgical implantation configurations, *iii)* haemolysis, *iv)* intraventricular aberrant flow patterns and *v)* surface contact activation.

In this study, the role of LV residual contractility as an additional thrombogenic factor was investigated, since the thrombus-favourable LV flow dynamics, in the pathological LV, was hypothesized to synergize to the mechanism of platelet activation and thrombus formation.

Moreover, given that both the LV residual contractility and the LVAD-induced hemodynamics might have a role in altering the LV hemodynamics promoting thrombogenesis, we herein analysed the mutual interactions between these two factors.

Investigation of this hypothesis was carried out by setting up a CFD model of the LV, that systematically analysed the contribution of LV residual contractility and LVAD inflow cannula implantation configurations on the LV thrombogenic potential through three sets of simulations.

For each of them, blood velocity patterns, blood stasis, and associated WSS trends in the apical region were analysed, to describe the intraventricular hemodynamics.

In simulation Set 1 *pre-implant*, the role of LV residual contractility as a possible thrombogenic factor was explored. It was found that decreasing values of LV residual EF% determined an increase in blood stasis in the apical region of the LV and, consequently, a reduction of the WSS in the same area.

Simulation Set 2 *post-implant A* was used to evaluate the impact of the inflow cannula on blood stagnation and the mutual interactions between LV residual contractility and LVAD flow rate.

When the LVAD inflow cannula was placed in the LV, WSS values decreased of one order magnitude with respect to those extracted, in the same apical region, from the *pre-implant* configurations. To note, it resulted that WSS were strongly influenced by LV residual contractility and, to a lesser extent, by LVAD flow rate.

Simulation Set 3 *post-implant* B was exploited to quantify the impact of cannula position on blood stagnation, so to identify the most hemodynamically favourable LVAD implantation configuration between the patient-specific positioning and the apical one.

The obtained results suggested a lower risk for thromboembolic events when the cannula was positioned in the apical configuration, because of lower blood stagnation and a more linear blood flow from the MV to the LVAD inflow cannula.

As pointed out in §2 (p.22), to achieve a detailed and reliable hemodynamic analysis whose results are not overly approximated, a LV CFD model should have the following properties:

- reproduce the patient-specific geometry of the LV;
- the imposed LV wall motion should replicate the cardiac one, thus accounting for myocardial torsion, as well as for LV wall contraction/dilation over the different phases of the cardiac cycle.

In addition, ventricular wall motion should be conceived so as to be applicable not only to *pre*-implant LV models but also to LVAD-assisted LV models.

These specifications were required since vortex dynamics, stagnation areas and recirculation patterns were strongly dependent on the LV morphology and cardiac wall motion.

The developed model fulfils all the listed requirements, since the geometry is patient-specific, LV wall motion is reconstructed taking into account both torsion and contraction/dilation and it is implemented for *pre* as well as for *post* implant models.

Furthermore, the implemented method for wall motion can be applied to any kind of geometry, just tuning properly the model parameters.

Concluding, the herein numerical approach proved efficient in achieving the main goals of the study; nonetheless, some limitations have to be declared as ideas for further improvements. LV blood flow was assumed to be laminar, as in previous studies [30, 49, 58-60]. In our model, the maximum Reynolds number at the mitral valve was $Re \cong 2000$, which supports the assumption of laminar flow. A recent CFD study [58], based on a turbulence model exploitation, actually reported turbulent fluctuations in the velocity field in the LV, but the authors concluded that laminar models can still capture the large-scale flow features.

The current method assumed an almost instantaneous opening or closing of the valves orefices. Valve motion undoubtedly affects the intraventricular flow, but, as pointed out by Baccani *et al.* [61], valve dynamics has no fundamental relevance on the LV global hemodynamic field, because of its rapidity. Another intrinsic limitation was ignoring the influence of mitral leaflets, trabeculae and papillary muscles, that can affect flow orientation and pattern of vortex formation and evolution [62].

Moreover, the isovolumetric phases of the cardiac cycle were not included in the simulations even though isovolumetric contraction and relaxation have an effect on blood stasis. Furthermore, a constant velocity BC was applied at the inlet of the cannula. By contrast, it is known that cannula suction flow rate depends on the impedance of the systemic circulation.

That being said, future developments of this work include the analysis of the impact of different cannula insertion lengths and tip geometries on LV hemodynamics; isovolumic contraction and relaxation phases will be considered in order to achieve a complete simulation of the cardiac cycle. In addition, a particle tracking analysis will be implemented, to directly determine recirculation and stagnation areas and zones of stress accumulation, through particle residence times and stress history.

With this study we provide further mechanistic insights into the mechanisms related to intraventricular thrombus formation and thromboembolic complications in LVAD patients. In detail, the results of our study suggest that the LV residual contractility and LVAD inflow cannula insertion configuration are hemodynamic-associated variables that must be considered when facing with the LVAD-induced thrombogenicity.

References

(1)   Lloyd-Jones DM, Larson MG, Leip EP, *et al*. Lifetime risk for developing congestive heart failure: the Framingham Heart Study. *Circulation 2002*;106:3068-72.

(2)   Townsend N, Wickramasinghe K, Bhatnagar P, *et al.* Coronary heart disease statistics. London: *British Heart Foundation*, 2012.

(3)   Cowie M, *et al*. Improving care for patients with acute heart failure. Before, during and after hospitalisation. *Heart Failure Association of the ESC*, 2014.

(4)   Molisso C, Molisso V. La cardiomiopatia dilatativa in ambito valutativo medico-legale. *G Ital Cardiol* 2007;8 (5):299-305.

(5)   Roberts WC, Siegel RJ, McManus BM. Idiopathic dilated cardiomyopathy: analysis of 152 necropsy patients. *Am J Cardiol* 1987;60:1340-55.

(6)   Feild BJ, Baxley WA, Russell RO Jr, *et al*. Left ventricular function and hypertrophy in cardiomyopathy with depressed ejection fraction. *Circulation* 1973;47:1022-31.

(7)   Wallis DE, O'Connell JB, Henkin RE, Costanzo-Nordin MR, Scanlon PJ. Segmental wall motion abnormalities in dilated cardiomyopathy: a common finding and good prognostic sign. *J Am Coll Cardiol* 1984;4:674-9.

(8)   Douglas PS, Morrow R, Ioli A, Reichek N. Left ventricular shape, afterload and survival in idiopathic dilated cardiomyopathy. *J Am Coll Cardiol* 1989;13:311-5.

(9)   Bergerone S, Morello M. Insufficienza cardiaca: fisiopatologia. Selezione di argomenti di cardiologia per i candidati all'idoneità apicale. *Centro Scientifico Editore Torino*, 1997:95-112.

(10)   Magnani B, Galiè N. Insufficienza cardiaca cronica. *La cardiologia nella pratica clinica* 1994;1:3-8.

(11)   Mariotti R, Mariani M. Meccanismi patogenetici dell'insufficienza cardiaca. *Cardiologia* 1996;41 (Suppl. 4):11-16.

(12)   Little WC. Valutazione della funzione cardiaca normale e patologica. In: Braunwald E, Zipes DP, Libby P, eds. *Malattie del cuore. VI edizione. San Donato Milanese (MI): Excerpta Medica*, 2002:500-24.

(13) Chioin R, Razzolini R. Scompenso cardiaco nel portatore di protesi valvolare. In: Rovelli F, DeVita C, Moreo A, eds. *Cardiologia 1995. Firenze: Scientific Press*, 1996:149-55.

(14) Gaash WH. Insufficienza aortica cronica: indici ecocardiografici di funzione e prognosi. *Primary Cardiology* Ed ital 1987;4:353-60.

(15) Borow KM, Green LH, Mann T, *et al*. End-systolic volume as a predictor of postoperative left ventricular performance in volume overload from valvular regurgitation. *Am J Med* 1980;68:655-63.

(16) McMurray JJ, Adamopoulos S, Anker SD, *et al*. ESC Guidelines for the diagnosis and treatment of acute and chronic heart failure 2012: The Task Force for the Diagnosis and Treatment of Acute and Chronic Heart Failure 2012 of the European Society of Cardiology. Developed in collaboration with the Heart Failure Association (HFA) of the ESC. *Eur Heart J* 2012;33:1787-847.

(17) Lam CS, Donal E, Kraigher-Krainer E, Vasan RS. Epidemiology and clinical course of heart failure with preserved ejection fraction. *Eur Heart J* 2011;13:18-28.

(18) Borlaug BA, Paulus WJ. Heart failure with preserved ejection fraction: pathophysiology, diagnosis, and treatment. *Eur Heart J* 2011;32:670-9.

(19) Dec G W, Fuster V. Idiopathic dilated cardiomyopathy. *N Engl J Med*, 1994 Dec 8;331(23):1564-75.

(20) Capoccia M. Mechanical Circulatory Support for Advanced Heart Failure: Are We about to Witness a New "Gold Standard"?. *J.Cardiovasc. Dev.* Dis. 2016, 3, 35.

(21) Fraser KH, Taskin ME, Griffith BP, Wu ZJ. The Use of Computational Fluid Dynamics in the Development of Ventricular Assist Devices. *Med Eng Phys.* 2011 April; 33(3):263-280.

(22) Kirklin JK, Naftel DC, Pagani FD, Kormos RL, Stevenson LW, Blume ED, Myers SL, Miller MA, Baldwin JT, Young JB. Seventh INTERMACS annual report: 15,000 patients and counting. *J Heart Lung Transplant.* 2015;34(12):1495-504.

(23) Marsden AL, Bazilevs Y, Long CC, Behr M. Recent advances in computational methodology for simulation of mechanical circulatory assist devices. *Wiley Interdiship Rev Sys Biol Med*, 2014 March; 6(2):169-188.

(24) Starling RC, Moazami N, Silvestry SC, Ewald G, Rogers JG, Milano CA, Rame JE, Acker MA, Blackstone EH, Ehrlinger J, Thuita L, Mountis MM, Soltesz EG, Lytle

BW, Smedira NG. Unexpected abrupt increase in left ventricular assist device thrombosis. *N Engl J Med*. 2014;370(1):33-40.

(25) Rogers JG, Pagani FD, Tatooles AJ, Bhat G, Slaughter MS, Birks EJ, Boyce SW, Najjar SS, Jeevanandam V, Anderson AS, Gregoric ID, Mallidi H, Leadley K, Aaronson KD, Frazier OH, Milano CA. Intrapericardial Left Ventricular Assist Device for Advanced Heart Failure. *N Engl J Med* 2017;376(5):451-460.

(26) Mehra MR, Naka Y, Uriel N, Goldstein DJ, Cleveland JC Jr, Colombo PC, Walsh MN, Milano CA1, Patel CB1, Jorde UP, Pagani FD, Aaronson KD, Dean DA, McCants K, Itoh A, Ewald GA, Horstmanshof D, Long JW, Salerno C; MOMENTUM 3 Investigators. A Fully Magnetically Levitated Circulatory Pump for Advanced Heart Failure. *N Engl J Med* 2017;376(5):440-450.

(27) Najjar SS, Slaughter MS, Pagani FD, Starling RC, McGee EC, Eckman P, Tatooles AJ, Moazami N, Kormos RL, Hathaway DR, Najarian KB, Bhat G, Aaronson KD3, Boyce SW; HVAD Bridge to Transplant ADVANCE Trial Investigators. An analysis of pump thrombus events in patients in the HeartWare ADVANCE bridge to transplant and continued access protocol trial. *J Heart Lung Transplant* 2014;33(1):23-34.

(28) Chiu WC, Alemu Y, *et al*. Ventricular Assist Device Implantation Configurations Impact Overall Mechanical Circulatory Support System Thrombogenic Potential. *ASAIO J.* 2017;63:285-292.

(29) Sheriff J, Bluestein D, Girdhar G, Jesty J. High-Shear Stress Sensitizes Platelets to Subsequent Low-Shear Conditions. *Ann Biomed Eng.* 2010 April;38(4):1442-1450.

(30) Prisco AR, Aliseda A, *et al*. Impact of LVAD Implantation Site on Ventricular Blood Stagnation. *ASAIO J.* 2017;63:392-400.

(31) Yin W, Shanmugavelayudam SK, Rubenstein DA. The effect of physiologically relevant dynamic shear stress on platelet and endothelial cell activation. *Thrombosis Res* (2011)127:235-241.

(32) Rossini L, Martinez-Legazpi P, Vu V, *et al*. A clinical method for mapping and quantifying blood stasis in the left ventricle. *J Biomech*. 2016 July 26;49(11): 2152–2161.

(33) Tang C, Zhu Y, Zhang J, *et al*. Analysis of left ventricular fluid dynamics in dilated cardiomyopathy by echocardiographic particle image velocimetry. *Echocardiography*. 2018;35:56–63.

(34) Mangual JO, Kraigher-Krainer E, Luca AD, Toncelli L, Shah A, Solomon S, Galanti G, Domenichini F, Pedrizzetti G. Comparative numerical study on left ventricular fluid dynamics after dilated cardiomyopathy. *J Biomech.* 2013 Jun 21;46(10):1611-7.

(35) Chiu WC, Alemu Y, McLarty AJ, Einav S, Slepian MJ, Bluestein D. Ventricular Assist Device Implantation Configurations Impact Overall Mechanical Circulatory Support System Thrombogenic Potential. *ASAIO J*. 2017;63(3):285-292.

(36) Taghavi S, Ward C, Jayarajan SN, Gaughan J, Wilson LM, Mangi AA. Surgical technique influences HeartMate II left ventricular assist device thrombosis. *Ann Thorac Surg.* 2013;96:1259-1265.

(37) Chivukula VK, Beckman JA, Prisco AR, Dardas T, Lin S, Smith JW, Mokadam NA, Aliseda A, Mahr C. Left Ventricular Assist Device Inflow Cannula Angle and Thrombosis Risk. *Circ Heart Fail*. 2018 Apr;11(4):e004325.

(38) Bavo AM, Pouch AM, Degroote J, Vierendeels J, Gorman JH, Gorman RC. Patient-specific CFD models for intraventricular flow analysis from 3D ultrasound imaging: Comparison of three clinical cases. J Biomech 2017 Jan 4; 50:144-150.

(39) Chan BT, Lim E, Chee KH, Abu Osman NA. Review on CFD simulation in heart with dilated cardiomyopathy and myocardial infarction. Computers in Biology and Medicine 2013; 43:377-385.

(40) Doost NS, Ghista D, Su B, Zhong L, Morsi YS. Heart blood flow simulation: a perspective review. BioMed Eng OnLine (2016); 15:101.

(41) Loerakker S, Cox LGE, van Heijst GJF, de Mol BAJM, van de Vosse FN. Influence of dilated cardiomyopathy and a left ventricular assist device on vortex dynamics in the left ventricle. Computer Methods in Biomechanics and Biomedical Engineering 2008; 11(6): 649-660.

(42) Bermejo J, et al. Intraventricular vortex properties in nonischemic dilated cardiomyopathy. Am. J. Physiol. Heart Circ Physiol. 2014; 306: H714-H729.

(43) Chan BT, Ong CW, Lim E, Abu Osman NA, Al Abed A, Lovell NH, Dokos S. Simulation of Left Ventricle Flow Dynamics with Dilated Cardiomyopathy during

the Filling Phase. Annual International Conference of the IEEE Engineering in Medicine and Biology Society. IEEE Engineering in Medicine and Biology Society. Conference. 2012; 6289-92.

(44)   Bavo AM, Pouch AM, Degroote J, Vierendeels J, Gorman JH, Gorman RC, Segers P. Patient-specific CFD simulation of intraventricular haemo-dynamics based on 3D ultrasound imaging. Biomed Eng OnLine. 2016; 15(107): 144-150.

(45)   Liu GM, Chen HB, Luo FL, Zhang Y, Sun HS, Zhou JY, Hu SS. Numerical Simulation of LVAD Inflow Cannulas with Different Tip. International Journal of Chemical Engineering, vol. 2012, Article ID 596960, 2012.

(46)   Ong CW, Dokos S, Chan BT, Lim E, Abed AA, Osman NABA, Kadiman S, Lovell NH. Numerical investigation of the effect of cannula placement on thrombosis. Theor Biol Med Model 2013; 10:35.

(47)   Ong CW, Chan T, Lim E, Abu Osman NA, Abed AA, Dokos S, Lovell NH. Fluid Structure Interaction Simulation of Left Ventricular Flow Dynamics under Left Ventricular Assist Device Support. Conf Proc IEEE Eng Med Biol Soc. 2012; 2012: 6293-6.

(48)   Liao S, Simpson B, Neidlin M, Kaufmann TAS, Li Z, Woodruff MA, Gregory SD. Numerical prediction of thrombus risk in an anatomically dilated left ventricle: the effect of inflow cannula designs. Biomed Eng Online. 2016 Dec 28; 15(Suppl 2): 136.

(49)   Liao S, Neidlin M, Li Z, Simpson B, Gregory SD. Ventricular flow dynamics with varying LVAD inflow cannula lengths: In-silico evaluation in a multiscale model. J Biomech 2018 Apr 27; 72: 106-115.

(50)   Medvitz RB, Reddy V, Deutsch S, Manning KB, Paterson EG. Validation of a CFD Methodology for Positive Displacement LVAD Analysis Using PIV Data. J Biomech Eng. 2009; 131(11):111009.

(51)   Laumen M, Kaufmann T, Timms D, Schlanstein P, Jansen S, Gregory S, Wong KC, Schmitz-Rode T, Steinseifer U. Flow Analysis of Ventricular Assist Device Inflow and Outflow Cannula Positioning Using a Naturally Shaped Ventricle and Aortic Branch. Artificial Organs 2010 Oct; 34(10): 798-806.

(52)   Wong K, Samaroo G, Ling I, Dembitsky W, Adamson R, del Alamo JC, May-Newman K. Intraventricular flow patterns and stasis in the LVAD-assisted heart. J Biomech. 2014 Apr 11; 47(6): 1485-94.

(53)   Apostoli A, Bianchi V. Development of an in vitro platform to characterize Endothelial Cell-Platelet pro-thrombotic interaction mechanisms associated with Left Ventricular Assist Device therapy. http://hdl.hsndle.net/10589/135360.

(54)   Omar AM, Vallabhajosyula S, Sengupta PP. Left Ventricular Twist and Torsion: research observations and clinical applications. Circ Cardiovasc Imaging. 2015 Jun;8(6).

(55)   Doost SN, Zhong L, Su B, Morsi YS. The numerical analysis of non-Newtonian blood flow in human patient-specific left ventricle. Comput Methods Programs Biomed. 2016 Apr;127:232-47.

(56)   Hunt JCR, Wray AA, Moin P. Eddies, stream, and convergence zones in turbulent flows. Center for Turbulence Research Report CTR-S88 1988, pp. 193-208.

(57)   Fukuda N, Itatani K, Kimura K, Ebihara A, Negishi K, Uno K, Miyaji K, Kurabayashi M, Takenaka K. Prolonged vortex formation during the ejection period in the left ventricle with low ejection fraction: a study by vector flow mapping. *J Med Ultrason* (2001) 2014 Jul; 41(3): 301–310.

(58)   Khalafvand SS, Ng EYK, Zhong L, Hung TK. Fluid-dynamics modelling of the human left ventricle with dynamic mesh for normal and myocardial infarction: preliminary study. *Comput Biol Med.* 2012 Aug; 42(8): 863–870.

(59)   Chnafa C,Mendez S, Nicoud F. Image-Based Simulations Show Important Flow Fluctuations in a Normal Left Ventricle: What Could be the Implications? *Ann Biomed Eng.* 2016 Apr 12.

(60)   Domenichini F, Pedrizzetti G, Baccani B. Three-dimensional filling flow into a model left ventricle. *Journal of Fluid Mechanics* 2005, 539, 179-198.

(61)   Baccani B, Domenichini F, Pedrizzetti G. Model and influence of mitral valve opening during the left ventricular filling. *J Biomech* 2003, 36, 355-361.

(62)   Vedula V, Seo JH, Lardo AC, Mittal R. Effect of trabeculae and papillary muscles on the hemodynamics of the left ventricle. *Theor. Comput. Fluid Dyn.* 2015, 30, 3-21.